



HAL
open science

Innovative simulation tool for composite material heating using microwave

Hermine Tertrais

► **To cite this version:**

Hermine Tertrais. Innovative simulation tool for composite material heating using microwave. Solid mechanics [physics.class-ph]. École centrale de Nantes, 2018. English. NNT : 2018ECDN0061 . tel-02117899

HAL Id: tel-02117899

<https://theses.hal.science/tel-02117899>

Submitted on 2 May 2019

HAL is a multi-disciplinary open access archive for the deposit and dissemination of scientific research documents, whether they are published or not. The documents may come from teaching and research institutions in France or abroad, or from public or private research centers.

L'archive ouverte pluridisciplinaire **HAL**, est destinée au dépôt et à la diffusion de documents scientifiques de niveau recherche, publiés ou non, émanant des établissements d'enseignement et de recherche français ou étrangers, des laboratoires publics ou privés.

THESE DE DOCTORAT DE

L'ÉCOLE CENTRALE DE NANTES
COMUE UNIVERSITE BRETAGNE LOIRE

ECOLE DOCTORALE N° 602
Sciences pour l'Ingénieur
Spécialité : « *Mécanique des solides, des matériaux, des structures et des surfaces* »

Par

Hermine TERTRAIS

« Développement d'un outil de simulation pour le chauffage de matériaux composites par micro-ondes »

Thèse présentée et soutenue à Nantes le 20 décembre 2018
Unité de recherche : Gem - Institut de Recherche en Génie Civil et Mécanique

Rapporteurs avant soutenance :

Amine AMMAR Professeur des Universités – ENSAM Angers
Vadim YAKOVLEV Associate Research Professor – Worcester Polytechnic Institute

Composition du Jury :

Président : Amine AMMAR Professeur des Universités – ENSAM Angers
Examineurs : Iciar ALFARO Associate Professor – Universidad de Zaragoza
 Jean-Yves HASCOET Professeur des Universités – Ecole Centrale de Nantes
 Vadim YAKOVLEV Associate Research Professor – Worcester Polytechnic Institute

Dir. de thèse : Francisco CHINESTA Professeur des Universités – ENSAM ParisTech
Co-enc. de thèse : Anaïs BARASINSKI Docteur – Ecole Centrale de Nantes

Invité

Jean-Claude KEDZIA Docteur – CEM Product Manager – ESI Group

Titre : Développement d'un outil de simulation pour le chauffage de matériaux composites par micro-ondes

Mots clés : Matériaux composites, micro-ondes, PGD, simulation

Résumé : Le travail présenté dans cette thèse s'inscrit dans le contexte du développement de nouveaux procédés pour la mise en forme de matériaux composites pour répondre aux contraintes industrielles de gain de temps et d'énergie. Le procédé de chauffage par micro-onde reposant sur un principe de chauffage volumique permet de garantir ces avantages.

L'inconvénient majeur est que le comportement du champ électrique lors de l'interaction entre matériaux composites et micro-ondes est peu connu. L'objectif de cette thèse est donc de proposer des solutions numériques pour approfondir la connaissance du procédé et la physique associée afin de mettre en avant ses capacités quant à un développement industriel. Pour ce faire, le travail réalisé est axé autour de trois verrous. En premier lieu, une nouvelle méthode numérique est proposée afin de résoudre

les équations de Maxwell en 3D dans un stratifié composite. Prendre en compte le comportement 3D est essentiel afin de décrire avec précision l'impact des différentes couches du matériau et de leur épaisseur sur la propagation du champ électrique.

Dans un second temps, la simulation électromagnétique est couplée à une résolution thermique afin de simuler le procédé de chauffage d'une pièce composite. Différents paramètres du procédé sont étudiés afin de mettre en avant les plus sensibles pour l'utilisation du chauffage micro-onde pour les matériaux composites.

Enfin, l'attention du lecteur est portée sur le développement d'une méthode de simulation pour un contrôle en temps réel du procédé en comparaison avec des essais expérimentaux.

Title : Innovative simulation tool for composite material heating using microwave

Keywords : Composite materials, microwaves, PGD, simulation

Abstract : The context of the present work is the development of new processes for the heating and forming of composite materials in order to provide an answer to the industrial needs for less energy and less time-consuming processes. In that sense, microwave heating is a perfect match as it relies on volumetric heating.

The major drawback is that the behaviour of the electric field while interacting with composite material is poorly known. Therefore, the main objective of this thesis is to provide numerical solutions to go more deeply in the understanding of such process and put forward its capabilities for an industrial development.

To fulfil this objective, the work is oriented over three main axes. First, an innovative simulation

tool is presented in order to solve the Maxwell's equations in a thin multilayered domain. Taking into account the 3D behaviour of the electric field is a major issue in order to describe precisely the impact of the different plies of the laminate on the propagation of the electric field. Then, the electromagnetic simulation is coupled with a thermal simulation in order to simulate the full heating process of a composite part. Parameters of the process are investigated to bring forward the most crucial ones.

Finally, real-time control of the process is tackled using a model order reduction simulation technique. These results are compared to experimental work on two sets of samples.

“N’ayez jamais peur de la vie, n’ayez jamais peur de l’aventure, faites confiance au hasard, à la chance, à la destinée. Partez, allez conquérir d’autres espaces, d’autres espérances. Le reste vous sera donné de surcroît.”

Henry de Monfreid

Acknowledgements

My first thanks go to my advisors Pr. Francisco (Paco) Chinesta and Dr. Anaïs Barasinski for guiding me during the three years of research I dedicated to this work. Their advice, steady scientific and moral support have been essential to the completion of my thesis. The unmatched enthusiasm of Paco has revived me more than once when motivation was not at a peak. The continuous presence and accompaniment of Anaïs has been an indispensable component of my work.

I would like to acknowledge all the members of my defense committee who took the time to come from close and far locations to assess my work and help me improve it.

A huge thanks to all of the research team that have provided me with scientific support, especially Chady Ghnatios, Ruben Ibanez and Enrique Nadal Soriano. Their help have been crucial and essential.

This work has been realised within the framework of the H2020 european project SIMUTOOL. Acknowledgements go to the simulation team I worked with and to all of the partners of the project.

Beside the technical support, I would like to thank all the colleagues and friends from Ecole Centrale de Nantes, for all the coffee breaks, the 'coinche' games over lunch, the releasing badminton sessions and the unique work yet relaxed atmosphere of the 'open-space du milieu'. A million special thanks to the best support group I could count on during the three years as a PhD student: Julie, Alexia, Marie-Emeline and Denise - a strong friendship build over cheese, wine and the occasional motivation breakdowns.

At last, I would like to thank my whole family for their long-lasting support. And more specially, to my Dad who tried to catch the technicality of my research and to my Mum who might not understand but always encouraged.

À Bonne-Maman d'Arradon

Contents

Acknowledgements	vii
List of Figures	xv
List of Tables	xxi
List of Symbols	xxiii
General Introduction	1
1 Electromagnetic Field Propagation in a Thin Multilayered Composite Part	3
1.1 Introduction	3
1.1.1 2D, 2.5D and 3D: from which to choose ?	5
1.1.2 PGD at a glance	7
1.2 Electromagnetic formulation	9
1.3 In-plane-out-of-plane separated representation	12
1.3.1 Separated representation	12
1.3.2 Functional approximation	13
1.4 PGD-based discretization	14
1.5 Numerical results	15
1.5.1 3-layer laminate	15
1.5.2 29-layer laminate	23
1.6 Discussion and conclusions	24
2 Simulation of the Microwave Heating of a Composite Preform	27
2.1 Introduction	27
2.1.1 Processing composite materials	28
2.1.2 Composite heating simulation with microwaves	30
2.2 Coupling electromagnetics and heating	31
2.2.1 Heat mechanisms	31
2.2.2 Numerical implementation	32
2.3 Electric field distribution in an oven cavity	33

2.3.1	Comsol Multiphysics modeling	33
2.3.2	Extracting the electromagnetic boundary conditions	36
2.4	Numerical results	37
2.4.1	Fibers choice: which material for MW processing ?	38
2.4.2	Influence of the plies orientation	44
2.4.3	Mold design to ensure uniform heating	46
2.4.4	Uncertainty on the dielectric properties	51
2.4.5	Placement of the tool in the oven cavity	53
2.5	Discussions and conclusions	55
3	Real-time Simulation for Direct Control during Microwave Heating	59
3.1	Introduction	59
3.1.1	A need for real-time control of process	60
3.1.2	Taking into account kinetic sources	61
3.2	Reduction of the heat equation with thermo-kinetic and electromagnetic sources	61
3.3	Experimental measurements for reduction model validation	64
3.3.1	Microwave oven device	65
3.3.2	Samples used	66
3.3.3	Temperature measurements	68
3.4	Experimental and simulation comparison	69
3.4.1	Sample 1: no kinetic heat sources	69
3.4.2	Sample 2: exothermic epoxy curing	74
3.5	Discussions and conclusions	78
	Conclusion	81
A	Basis of electromagnetism	83
A.1	Maxwell's equations	83
A.2	Curl-curl formulation	84
A.3	Interface conditions for electric field	85
B	PGD technique - detailed example on the heat equation	89
B.1	PGD assumption and heat equation	89
B.2	Construction of the separated representation	90
B.2.1	Step 1. Calculating $X_n^p(x)$ from $Y_n^{p-1}(y)$ and $\Theta_n^{p-1}(t)$	91
B.2.2	Step 2. Calculating $Y_n^p(y)$ from $X_n^p(x, y)$ and $\Theta_n^{p-1}(t)$	92
B.2.3	Step 3. Calculating $\Theta_n^p(t)$ from $X_n^p(x)$ and $Y_n^p(y)$	94
B.3	Numerical application	95

Bibliography

List of Figures

1	Laminated composite composed of a specific stacking sequence of plies made of fibers and polymer matrix [15]	1
2	Production of composite VS other materials in weight	2
1.1	Three-(thin)-plies laminate	17
1.2	V_x on $\partial\Omega$	17
1.3	V_y on $\partial\Omega$	17
1.4	V_z on $\partial\Omega$	18
1.5	Electric field along the plate thickness, $E_x(0.25, 0.25, z)$	18
1.6	Electric field along the plate thickness, $E_y(0.25, 0.25, z)$	18
1.7	Electric field along the plate thickness, $E_z(0.25, 0.25, z)$	19
1.8	Electric field along the plate thickness, $E_x(0.25, 0.25, z)$ when considering a coarser mesh in the thickness	19
1.9	Electric field along the plate thickness, $E_y(0.25, 0.25, z)$ when considering a coarser mesh in the thickness	20
1.10	Electric field along the plate thickness, $E_z(0.25, 0.25, z)$ when considering a coarser mesh in the thickness	20
1.11	Electric field along the central layer thickness when considering a mesh in the thickness consisting of 30 elements	21
1.12	Electric field along the central layer thickness when considering a mesh in the thickness consisting of 300 elements	22
1.13	Electric field along the central layer thickness when considering a mesh in the thickness consisting of 3000 elements	22
1.14	Electromagnetic losses: (left) dielectric and (right) eddy current	23
1.15	29-ply laminate	24
1.16	Electric field along the plate thickness, $E_x(0.25, 0.25, z)$	24
1.17	Electric field along the plate thickness, $E_y(0.25, 0.25, z)$	25
1.18	Electric field along the plate thickness, $E_z(0.25, 0.25, z)$	25
2.1	Composite material processes involving electromagnetics and their frequency range	29
2.2	Oven cavity geometry	34

2.3	Mesh generated by Comsol for the oven	34
2.4	Mesh generated by Comsol for the composite plate	35
2.5	Example of E_x component of electric field on the mold surface	35
2.6	Example of E_y component of electric field on the mold surface	35
2.7	Example of E_z component of electric field on the mold surface	36
2.8	Test case geometry with composite and mold - all dimensions are given in mm	38
2.9	Carbon case - electric field along $(x_{middle}, y, z_{middle})$	40
2.10	Glass case - electric field along $(x_{middle}, y, z_{middle})$	41
2.11	Carbon case - electric field along the thickness $(x_{middle}, y_{middle}, z)$	41
2.12	Glass case - electric field along the thickness $(x_{middle}, y_{middle}, z)$	42
2.13	Carbon case - temperature distribution in the middle section (x, y, z_{middle}) after heating for 20 min	42
2.14	Glass case - temperature distribution in the middle section (x, y, z_{middle}) after heating for 20 min	43
2.15	Carbon case - temperature field along the thickness $(x_{middle}, y_{middle}, z)$ (left) after heating for 20 min and temperature evolution along time at central location $(x_{middle}, y_{middle}, z_{middle})$ (right)	43
2.16	Glass case - temperature field along the thickness $(x_{middle}, y_{middle}, z)$ after heating for 20 min (left) and temperature evolution along time at central location $(x_{middle}, y_{middle}, z_{middle})$ (right)	44
2.17	0° case - electric field along $(x_{middle}, y, z_{middle})$	44
2.18	90° case - electric field along $(x_{middle}, y, z_{middle})$	45
2.19	Comparison of 0° and 90° cases - electric field along the thick- ness zoomed at composite interfaces $(x_{middle}, y_{middle}, z_{composite})$	45
2.20	Comparison of 0° and 90° cases - temperature field along the thickness $(x_{middle}, y_{middle}, z)$ after heating for 20 min	46
2.21	No-conductive case - electric field along the thickness $(x_{middle}, y_{middle}, z)$ (left) and along $(x_{middle}, y, z_{middle})$ (right)	47
2.22	$500\mu m$ case - electric field along the thickness $(x_{middle}, y_{middle}, z)$ (left) and along $(x_{middle}, y, z_{middle})$ (right)	47
2.23	$1mm$ case - electric field along the thickness $(x_{middle}, y_{middle}, z)$ (left) and along $(x_{middle}, y, z_{middle})$ (right)	47
2.24	$500\mu m$ case - electric field along the thicknees zoomed at the composite interface	48
2.25	$1mm$ case - electric field along the thicknees zoomed at the composite domain interface	48

2.26	No-conductive case - losses (left) and temperature field (right) along the thickness after heating for 20 min	49
2.27	500 μm case - losses (left) and temperature field (right) along the thickness after heating for 20 min	49
2.28	1mm case - losses (left) and temperature field (right) along the thickness after heating for 20 min	50
2.29	No-conductive case - temperature distribution in the middle section after heating for 20 min	50
2.30	500 μm case - temperature distribution in the middle section after heating for 20 min	50
2.31	1mm case - temperature distribution in the middle section after heating for 20 min	51
2.32	$\sigma - 10\%$ case - temperature distribution in the middle section after heating for 10 min	52
2.33	$\sigma_{original}$ case - temperature distribution in the middle section after heating for 10 min	52
2.34	$\sigma + 10\%$ case - temperature distribution in the middle section after heating for 10 min	52
2.35	Temperature evolution of the hot spots in the part according to the value of the electrical conductivity σ	53
2.37	Offset-x case - distribution of the electric field norm on the top surface of the mold	54
2.36	Centered case - distribution of the electric field norm on the top surface of the mold	54
2.38	Offset-xy case - distribution of the electric field norm on the top surface of the mold	55
2.39	Centered case - temperature distribution in the middle section of the domain after heating for 45 min	55
2.40	Offset-x case - temperature distribution in the middle section of the domain after heating for 45 min	56
2.41	Offset-xy case - temperature distribution in the middle section of the domain after heating for 45 min	56
3.1	Hexagonal-shaped Hephaistos microwave oven	65
3.2	Electric field amplitude for the empty oven with all waveguides feeding	66
3.3	Surface currents (right) for the empty oven with all waveguides feeding	67
3.4	Mold design for experimental tests in the microwave oven	67

3.5	Projected fiber sample prior to heating	68
3.6	Carbon / epoxy sample prior to heating	68
3.7	Heating cycles for projected fiber sample (left) and carbon / epoxy sample (right) where t_s refers to the shortest possible heating time from ambient temperature to 230°C	69
3.8	Thermocouples location in the projected-fiber sample, bottom view of the tool and sample - striped thermocouples represent the thermocouples inserted in the middle of the part	70
3.9	Thermocouples location in the projected-fiber sample, top view of the tool and sample	70
3.10	Thermocouples location in the projected-fiber sample, front view of the tool and sample	71
3.11	Thermocouples location in the carbon / epoxy sample, bottom view of the tool and sample	71
3.12	Thermocouples location in the carbon / epoxy sample, top view of the tool and sample	71
3.13	Thermocouples location in the carbon / epoxy sample, front view of the tool and sample	72
3.14	Heat sources distribution in the composite part for unitary power delivered by the twelve magnetrons for the projected-fiber sample in W/m^3	72
3.15	Power evolution during the projected-fiber sample trial (100% of the power represents a total 10.2 kW delivered by the twelve magnetrons)	72
3.16	Measured temperature evolution at the six sensors locations in the projected-fiber sample	73
3.17	Temperature evolution at sensors location simulated with the MOR technique for the projected fiber sample	73
3.18	Temperature distribution at the end of the heating process in the middle cross-section of the composite part for the projected fiber sample	74
3.19	Power evolutions for the optimised (rleft) and initial (right) heating processes for the projected-fiber sample	74
3.20	Temperature evolution at the six sensors locations in the projected-fiber sample for the optimised heating	75
3.21	Heat sources distribution in the composite part for unitary power delivered by the twelve magnetrons for the carbon / epoxy sample in W/m^3	75

3.22	Power evolution during the carbon / epoxy sample trial (100% of the power represents a total 10.2 kW delivered by the twelve magnetrons)	76
3.23	Measured temperature evolution in time at the six sensors locations in the carbon / epoxy sample	77
3.24	Temperature evolution at sensors location for the carbon / epoxy sample and simplified kinetic model	78
A.1	Box at the interface between two media	86
A.2	Loop at the interface between two media	86
B.1	Initial condition f defined on $\Omega_{xy} = (0, L) \times (0, L)$	90
B.2	Temperature distribution as calculated using the PGD at different time	96
B.3	$T_{PGD} - T_{ex}$ for $M = 90$ and different enrichment steps N for $t = t_{max}$	96
B.4	Error between PGD solution and analytical solution as a function of enrichment steps N and discretization refinement M for $t = t_{max}$	97

List of Tables

2.1 Dielectric and thermal material properties - GFRP and CFRP respectively stand for Glass and Carbon Fiber Reinforced Polymer, \parallel and \perp respectively characterise the material property in the longitudinal and transversal directions of the fibers of the ply	39
3.1 Parameters for the Kamal-Sourour model of the kinetic reaction of the epoxy resin [44, 45]	77

List of Symbols

E	Electric field intensity	V/m
H	Magnetic field intensity	A/m
D	Electric flux density	C/m ²
B	Magnetic flux density	T
J	Electric current density	A/m ²
E_x	x-component of electric field	V/m
E_y	y-component of electric field	V/m
E_z	z-component of electric field	V/m
ρ_c	Volume charge density	C/m ³
μ	Magnetic permeability	H/m
μ_r	Relative permeability	
ϵ	Electrical complex permittivity	F/m
ϵ_r	Relative permittivity	
σ	Electric conductivity	S/m
ω	Angular frequency	rad/s
\mathbf{n}	Unit outward vector normal to a surface	
ϕ	Heat flux	W/m ²
ϕ_s	Normal heat flux to the surface	W/m ²
T	Temperature field	K
T_∞	Outside temperature	K
λ	Thermal conductivity	W/mK
ρ	Volumetric mass density	kg/m ³
ρ_r	Volumetric mass density of the resin	kg/m ³
C_p	Specific heat	J/kgK
h	Heat transfer coefficient	W/m ² K
Q_{MW}	Heat sources from microwave heating	W/m ³
Q_{kin}	Heat sources from kinetic reaction	W/m ³
α	Degree of cure	
ΔH	Enthalpy of reaction	J/g
V_f	Fiber content	

a_{\parallel}	Material property along the fiber direction	
a_{\perp}	Material property along the transversal fiber direction	
\bar{a}	Conjugate of complex number	
$\nabla \cdot$	Divergence operator	
$\nabla \times$	Curl operator	
∇	Gradient operator	
μ_0	Vacuum permeability	$12.57 \cdot 10^{-7} \text{ H/m}$
ϵ_0	Vacuum permittivity	$8.854 \cdot 10^{-12} \text{ F/m}$
R	Gas constant	8.314 J/molK

General Introduction

The research work presented in this thesis is part of the wider context of the processing and forming of composite material. Composite materials are commonly used as structural parts in the main sectors of use: the transportation industries and civil engineering. A composite part, as we will consider in the following, is a part made of a combination of reinforcement - fibers - and matrix. Several types of fibers can be encountered in today's applications of composite materials, the main ones being glass fibers and carbon fibers. The matrix is composed of polymers, either thermoset such as epoxy and phenolic resins or thermoplastic such as PEEK or PET. The resin acts as a binder between the fibers to ensure continuity and transfer the loads endured by the part. Fibers and matrix are preformed in plies which are then stacked (Fig. 1) such as they fulfill the mechanical properties needed for the part. The combination of light weight and high mechanical properties have made the composite material an option that cannot be overlooked by manufacturers.

Beside the advantages and trending use of composite materials, the goal of composite producers is to compete and overcome the other materials (Fig. 2) which are still innovating and improving their own characteristics.

In this framework, new challenging and industrial-friendly processes have to

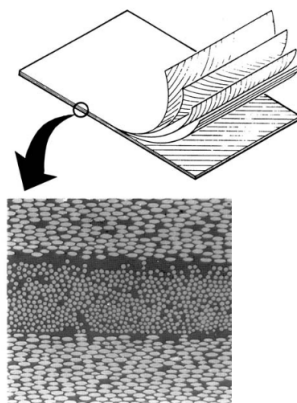


FIGURE 1: Laminated composite composed of a specific stacking sequence of plies made of fibers and polymer matrix [15]

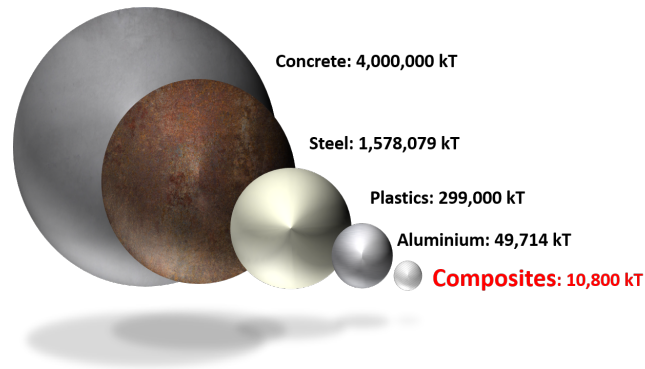


FIGURE 2: Production of composite VS other materials in weight

be developed and perfected. That is why the microwave heating of composite materials will be studied in the following work. Despite the wide use of microwave heating for domestic applications, this fast process known to all has not yet reach the industry of composite processing. A lot of unknown still remains on the phenomena occurring when there is interaction between electromagnetic fields at the microwave frequency and a laminated composite material because of its multiscale and multi-material aspects. In order to increase our knowledge, simulation solutions are proposed in the following chapters.

Several issues will be raised and studied in the following order:

- Dealing with electromagnetic fields means solving the Maxwell's equations in order to apprehend the behaviour of such fields in a multi-scale material such as a laminated composite part. However, an adapted 3D simulation technique needs to be developed in order to take into account the specificity of the geometry and the material we are working with: a thin multilayered part.
- Studying the heating of a part using electromagnetics implies a coupling between two interdependent physics. What is then left is to understand the impact of the electric field properties and distribution on the heating of the part.
- Finally, in order to have a competitive process, real-time monitoring has to be possible to have a precise control over the temperature field in the composite part and the curing of the resin. Such real-time monitoring is made accessible by using the appropriate simulation technique and modeling.

Chapter 1

Electromagnetic Field Propagation in a Thin Multilayered Composite Part

Contents

1.1 Introduction	3
1.1.1 2D, 2.5D and 3D: from which to choose ?	5
1.1.2 PGD at a glance	7
1.2 Electromagnetic formulation	9
1.3 In-plane-out-of-plane separated representation	12
1.3.1 Separated representation	12
1.3.2 Functional approximation	13
1.4 PGD-based discretization	14
1.5 Numerical results	15
1.5.1 3-layer laminate	15
1.5.2 29-layer laminate	23
1.6 Discussion and conclusions	24

1.1 Introduction

Many electrical and structural components are constituted of a stacking of multiple thin layers with different electromagnetic, mechanical and thermal properties (e.g. laminated magnetic cores and circuits when looking for reducing the eddy currents or usual composite materials). In the case of composite materials for structural parts some recent studies reveal that thin-ply laminates exhibit higher strength than their counterparts making use

of thicker plies [75, 76, 92, 74]. The main characteristic of such structural systems is that the plies composing them, and even the component itself, have a characteristic dimension (the one related to the thickness) much lower than the other in-plane characteristic lengths. The analysis of such geometrically degenerated systems does not concern solely the mechanical performances as discussed below.

In thin-ply composite laminates we can define three scales: (i) the macroscopic one that concerns the plates or shells, that is, the component scale; (ii) the mesoscopic one evidencing its intimate multi-layered structure and consequently its heterogeneity along the component thickness, with many thin-ply plies exhibiting different electromagnetic, mechanical and thermal properties; and finally (iii) the microscopic scale that reveals the intimate structure of each ply, in which the reinforcement, usually consisting of continuous unidirectional carbon or glass fibres impregnated by a thermoplastic or thermoset resin, with many possible microstructures.

Both the macroscopic and the mesoscopic models (the former using in general through-the-thickness homogenized properties and the last addressing explicitly the properties of each layer composing the laminate, that results at its turn from an adequate microscopic upscaling taking into account each particular fiber arrangement into the matrix) are defined in plate or shell domains characterized by having one dimension (the thickness) several orders of magnitude lower than the other representative in-plane dimensions. This fact, even if it is not a major conceptual issue, is a real handicap for simulation purposes. This situation is not new, plate and shell theories were successfully developed many years ago and they were intensively used in structural mechanics. These theories make use of some kinematic and mechanic hypotheses to reduce the 3D nature of mechanical models to 2D reduced models defined in the plate (or shell) middle surface. In the case of elastic behaviors the derivation of such reduced models is quite simple and it constitutes the foundations of classical plate and shell theories. Today, most commercial codes for structural mechanics applications propose different type of plate and shell finite elements, even in the case of multilayered composite plates or shells.

1.1.1 2D, 2.5D and 3D: from which to choose ?

In the context of electromagnetism the situation was similar to the one encountered in structural mechanics as discussed in [71, 80], where 2D cross-section, 2.5D planar solvers and 3D arbitrary-solvers were discussed. Waveguides simulators widely employed 2.5D formulations where one of the dimensions was eliminated by assuming a particular evolution of the electromagnetic field in that direction [17, 66, 30]. 2.5D formulations have been also extensively considered for analyzing printed circuits [86, 53].

Microscopic, mesoscopic and macroscopic models have been proposed and widely considered in engineering applications, in particular in those involving laminates. Many works concerned the microscopic homogenization of electromagnetic systems, in particular composite materials [85]. At the mesoscopic scale, laminates were addressed in view of defining macroscopic approaches. Three main routes were considered: (i) laminate homogenization [63, 32]; (ii) monolayer and multilayer shell elements were proposed in [7, 8], where the shell impedance was derived analytically by assuming a number of simplifying hypotheses and then coupled with the electromagnetic problem solution in the external domain in order to obtain the electromagnetic fields on the shell surfaces, and from them calculating all the physics inside (it is important to note that the assumed hypotheses could, in some complex circumstances, prove defective); (iii) special elements were proposed in [13] for meshing laminates when addressing explicitly the solution inside, however, for finely representing boundary layers inside the plies the computing complexity due the required mesh resolution could become excessive.

When 3D models become compulsory, the approximation of the different fields could imply thousands of nodes distributed along the thickness direction, and consequently millions of nodes to represent the fields in the case of a composite part. Such solution is now, in principle, possible thanks to the impressive progresses reached in modeling, numerical techniques (e.g., in FEM and FDTD) and computer science (e.g., GPU) in the last decades. However, the solution of such rich 3D models remains very difficult to achieve as it requires access to wide computational resources. Simulation attempts using the well experienced mesh-based discretization techniques fail because of the excessive number of degrees of freedom involved in the full 3D discretization as very fine meshes are required in the thickness direction (despite its reduced dimension - few mm in the case of composite materials). Consequence is that the in the in-plane directions would also require fine

discretization to avoid too distorted meshes and also because some processes (e.g. microwaves) require fine in-plane representations. The only getaway in such impasse is to explore new discretization strategies able to circumvent or at least alleviate the drawbacks related to mesh-based discretization of fully 3D models defined in plate or shell domains. To circumvent the just discussed issues, an efficient in-plane-out-of-plane separated representation has been proposed some years ago with the aim of computing fully 3D solutions as a sequence of problems defined in the plane and others (1D) in the thickness. Thus, high-resolution 3D solutions could be computed at the cost of 2D dimensional calculations.

The use of separated representations was originally proposed for defining non-incremental solvers based on the separation of space and time [49], then they were extended for addressing the solution of multidimensional models suffering the so-called curse of dimensionality [3]. The technique based on the use of separated representations was called Proper Generalized Decomposition – PGD –. The interested reader can refer to the recent reviews [19] [18, 21] and the references therein.

A direct consequence was separating the physical space. Thus in plate domains an in-plane-out-of-plane decomposition was proposed for solving 3D flows occurring in RTM – Resin Transfer Moulding – processes [18], then for solving elasticity problems in plates [11] and shells [10]. In those cases the 3D solution was obtained from the solution of a sequence of 2D problems (the ones involving the in-plane coordinates) and 1D problems (the ones involving the coordinate related to the plate thickness). It is important to emphasize the fact that these approaches are radically different from standard ones. Such 3D solver is able to compute the different unknown 3D fields without the necessity of introducing any hypothesis. The most outstanding advantage is that 3D solutions can be obtained with a computational cost characteristic of standard 2D solutions.

PGD has been used in the framework of electrical engineering [70, 37, 38, 56], however these works considered mainly space-time separation for performing transient simulation in a non-incremental way.

The main contribution of the present work is the proposal of an efficient in-plane-out-of-plane separated representation of the double-curl formulation of Maxwell equations able to address thin-layer laminates while ensuring the continuity and discontinuity of the tangential and normal electric field

components respectively at the plies interface. Before addressing electromagnetic models within the PGD framework, a summary of its main ingredients is given.

1.1.2 PGD at a glance

Most of the existing model reduction techniques proceed by projecting the problem solution onto a reduced basis (this constitutes the wide class of *projection-based model order reduction* methods). Therefore, the construction of the reduced basis usually constitutes the first step in the solution procedure, giving rise to a second important distinction when classifying Model Order Reduction – MOR – techniques: *a posteriori* versus *a priori* model order reduction. One must be careful on the suitability of a particular reduced basis when employed for representing the solution of a particular problem, particularly if it was obtained through *snapshots* of slightly different problems. This difficulty (at least partially) disappears if the reduced basis is constructed at the same time that the problem is solved (in other words: *a priori* with no need for snapshots of different problems). Thus, each problem has its associated basis in which its solution is expressed. One could consider few vectors in the basis, leading to a reduced representation, or all the terms needed for approximating the solution up to a certain accuracy level. The Proper Generalized Decomposition (PGD), which is described in general terms in what follows proceeds in this manner. For deep details on the separated representation constructor itself, the interested reader can refer to [20] and the numerous references therein. A simple example of the construction of the PGD and how the separation is managed is given in Appendix B. This section aims to guide the reader to the separated representation principle.

When calculating the transient solution of a generic problem, say $u(x, t)$, we usually consider a given basis of space functions $N_i(x)$, $i = 1, \dots, N_n$, the so-called shape functions within the finite element framework, being N_n the number of nodes. They approximate the problem solution as

$$u(x, t) \approx \sum_{i=1}^{N_n} a_i(t) N_i(x). \quad (1.1)$$

This implies a space-time separated representation where the time-dependent coefficients $a_i(t)$ are unknown at each time instant (when proceeding incrementally) and the space functions $N_i(x)$ are given *a priori*, e.g., piece-wise

polynomials. POD – Proper Orthogonal Decomposition – and Reduced Basis methodologies consider a set of global, reduced basis $\phi_i(x)$ for approximating the solution instead of the generic, but local, finite element functions $N_i(x)$. The former are expected to be more adequate to approximate the problem at hand. Thus, it results

$$u(x, t) \approx \sum_{i=1}^R b_i(t) \phi_i(x), \quad (1.2)$$

where it is expected that $R \ll N_n$. Again, Eq. (1.2) represents a space-time separated representation where the time-dependent coefficient must be calculated at each time instant during the incremental solution procedure.

Inspired from these results, one could consider the general space-time separated representation

$$u(x, t) \approx \sum_{i=1}^N X_i(x) \cdot T_i(t), \quad (1.3)$$

where now neither the time-dependent functions $T_i(t)$ nor the space functions $X_i(x)$ are *a priori* known. Both will be computed on the fly when solving the problem.

As soon as one postulates that the solution of a transient problem can be expressed in the separated form (1.3), whose approximation functions $X_i(x)$ and $T_i(t)$ will be determined during the problem solution, one could make a step forward and assume that the solution of a multidimensional problem $u(x_1, \dots, x_d)$ could be found in the separated form

$$u(x_1, x_2, \dots, x_d) \approx \sum_{i=1}^N X_i^1(x_1) \cdot X_i^2(x_2) \cdot \dots \cdot X_i^d(x_d), \quad (1.4)$$

and even more, expressing the 3D solution $u(x, y, z)$ as a finite sum decomposition involving low-dimensional functions

$$u(x, y, z) \approx \sum_{i=1}^N X_i(x) \cdot Y_i(y) \cdot Z_i(z), \quad (1.5)$$

or

$$u(x, y, z) \approx \sum_{i=1}^N X_i(x, y) \cdot Z_i(z). \quad (1.6)$$

Equivalently, the solution of a parametric problem $u(\mathbf{x}, t, p_1, \dots, p_\varphi)$ could be approximated as

$$u(\mathbf{x}, t, p_1, \dots, p_\varphi) \approx \sum_{i=1}^N X_i(\mathbf{x}) \cdot T_i(t) \cdot \prod_{k=1}^{\varphi} P_i^k(p_k). \quad (1.7)$$

1.2 Electromagnetic formulation

The usual approach when solving a general electromagnetic problem with the finite element method is considering edge elements [60] with the double-curl formulation of Maxwell equations. The use of edge elements allow efficiently circumventing the main problems of FEM applied to electromagnetic models [42], in particular they produce spurious-free solutions and ensure the normal discontinuity and tangential continuity between different media, however some disadvantages have been also pointed out [57, 58], concerning the ill-conditioning of discrete systems when the number of degrees of freedom – *dof* – increases. Some solutions were proposed for circumventing such issue, as for example the introduction of Lagrange multipliers [23], with the associate *dof* increase.

Many authors preferred the use of nodal-regularized formulations to avoid spurious solutions [36, 25], while proposing ad-hoc solutions for accounting the transfer conditions at the material interfaces, as implemented in the ER-MES software [64], consisting of duplicating the nodes located at the interfaces, for approximating the discontinuous field while enforcing the jump condition. Moreover, in these formulations a second regularization is required for addressing field singularities.

In the case of multilayered laminates, the interfaces coincide with constant values of the out-of-plane coordinate (the thickness). Therefore, implementing a discontinuous approximation within the in-plane-out-of-plane separated representation involved in the PGD seems quite simple. Thus, the modeling framework that considered consists of standard approximations combined with a regularized formulation, with an ad-hoc treatment of interface transfer conditions.

Electromagnetic physics are described by the Maxwell's equations. These four equations link electric and magnetic fields in space and time:

$$\left\{ \begin{array}{l} \nabla \times \mathbf{H} = \mathbf{J} + \frac{\partial \mathbf{D}}{\partial t} \\ \nabla \times \mathbf{E} = -\frac{\partial \mathbf{B}}{\partial t} \\ \nabla \cdot \mathbf{D} = \rho_c \\ \nabla \cdot \mathbf{B} = 0 \end{array} \right. , \quad (1.8)$$

with:

\mathbf{H} the magnetic field intensity (A/m)

\mathbf{E} the electric field intensity (V/m)

\mathbf{B} the magnetic flux density (T)

\mathbf{D} the electric flux density (C/m^2)

\mathbf{J} the electric current density (A/m^2)

ρ_c the volume charge density (C/m^3)

The double-curl formulation that is going to be solved is derived from the above Maxwell's equations in the frequency space (detailed in Appendix A), that in absence of volume charge density in the laminate, reads

$$\nabla \times \left(\frac{1}{\mu} \nabla \times \mathbf{E} \right) - \omega^2 \epsilon \mathbf{E} = 0, \quad \text{in } \Omega \subset \mathbb{R}^3 \quad (1.9)$$

with the complex permittivity ϵ given by

$$\epsilon = \epsilon_0 \epsilon_r - i \frac{\sigma}{\omega}, \quad (1.10)$$

and where μ , ϵ_r and σ represent the usual magnetic permeability, the electric permittivity and the conductivity respectively and ϵ_0 is the constant vacuum permittivity.

The previous equation is complemented with adequate boundary conditions. Without loss of generality we are assuming in what follows Dirichlet boundary conditions in the whole domain boundary $\partial\Omega$

$$\mathbf{n} \times \mathbf{E} = \mathbf{E}_g^t, \quad \text{in } \partial\Omega \quad (1.11)$$

where \mathbf{n} refers to the unit outwards vector defined on the domain boundary. In the previous expressions \mathbf{E}_g^t is the prescribed electric field (assumed known) on the domain boundary, tangent to the boundary as Eq. (1.11) expresses.

The weighted residual weak form is obtained by multiplying (1.9) by the test function \mathbf{E}^* (in fact by its conjugate, $\bar{\mathbf{E}}^*$, to define properly scalar products being the electric field a complex field, i.e. $\mathbf{E} = \mathbf{E}_r + i\mathbf{E}_i$), and then integrating by parts, to obtain

$$\begin{aligned} \int_{\Omega} \frac{1}{\mu} (\nabla \times \mathbf{E}) \cdot (\nabla \times \bar{\mathbf{E}}^*) \, d\mathbf{x} - \omega^2 \int_{\Omega} \epsilon \mathbf{E} \cdot \bar{\mathbf{E}}^* \, d\mathbf{x} - \\ \int_{\partial\Omega} \frac{1}{\mu} (\nabla \times \mathbf{E}) \cdot (\mathbf{n} \times \bar{\mathbf{E}}^*) \, d\mathbf{x} = 0, \end{aligned} \quad (1.12)$$

for all test function $\bar{\mathbf{E}}^*$ regular enough.

In the previous expression the boundary integral can be removed if the test function is assumed verifying $\mathbf{n} \times \bar{\mathbf{E}}^* = 0$ on $\partial\Omega$ where Dirichet boundary conditions are enforced, i.e. $\mathbf{n} \times \mathbf{E}$ on $\partial\Omega$. As such boundary conditions are assumed on the whole domain boundary, the weak form reduces to

$$\int_{\Omega} \frac{1}{\mu} (\nabla \times \mathbf{E}) \cdot (\nabla \times \bar{\mathbf{E}}^*) \, d\mathbf{x} - \omega^2 \int_{\Omega} \epsilon \mathbf{E} \cdot \bar{\mathbf{E}}^* \, d\mathbf{x} = 0 \quad (1.13)$$

However, it is known [36, 25] that the weak form (1.13) produces spurious solutions because even if Eq. (1.9) ensures the verification of the Gauss equation $\nabla \cdot (\epsilon \mathbf{E}) = 0$, its discrete counterpart after approximating the different fields implied in the weak form (1.13) does not ensure the fulfillment of the Gauss equation. Thus, a regularization is compulsory for avoiding these spurious solutions. In what follows we consider the regularized form [64]

$$\nabla \times \left(\frac{1}{\mu} \nabla \times \mathbf{E} \right) - \bar{\epsilon} \nabla \left(\frac{1}{\bar{\epsilon} \epsilon \mu} \nabla \cdot (\epsilon \mathbf{E}) \right) - \omega^2 \epsilon \mathbf{E} = 0, \quad (1.14)$$

whose (regularized) weak form when Dirichlet boundary conditions apply on the wall domain boundary, reads

$$\begin{aligned} \int_{\Omega} \frac{1}{\mu} (\nabla \times \mathbf{E}) \cdot (\nabla \times \bar{\mathbf{E}}^*) \, d\mathbf{x} - \omega^2 \int_{\Omega} \epsilon \mathbf{E} \cdot \bar{\mathbf{E}}^* \, d\mathbf{x} + \\ \int_{\Omega} \frac{\tau}{\bar{\epsilon} \epsilon \mu} (\nabla \cdot (\epsilon \mathbf{E})) (\nabla \cdot (\bar{\epsilon} \bar{\mathbf{E}}^*)) \, d\mathbf{x} - \int_{\partial\Omega} \frac{\tau}{\bar{\epsilon} \epsilon \mu} (\nabla \cdot (\epsilon \mathbf{E})) (\mathbf{n} \cdot (\bar{\epsilon} \bar{\mathbf{E}}^*)) \, d\mathbf{x} = 0, \end{aligned} \quad (1.15)$$

where τ is the regularization coefficient proposed in [65] and that according to that reference is taken with a unit value everywhere except at the interfaces where it vanishes. Eq. (1.15) is the weak formulation used for the further developments of the PGD-based simulation for the rest of this chapter.

1.3 In-plane-out-of-plane separated representation

This section presents the new approach developed during the thesis work in order to solve Eq. (1.15) using the PGD technique. To ensure a high enough resolution of the electric field along the component thickness to represent the multilayered structure of a composite part, we consider an in-plane-out-of-plane separated representation in $\Omega = \Omega_p \times \Omega_t$, with $\Omega_p \subset \mathbb{R}^2$ and $\Omega_t \in \mathbb{R}$. Each point $\mathbf{x} \in \Omega$ is decomposed in its plane component $(x, y) \in \Omega_p$ and its out-of-plane $z \in \Omega_t$.

1.3.1 Separated representation

The electric field is expressed as

$$\mathbf{E}(x, y, z) \approx \sum_{i=1}^N \mathbf{P}_i(x, y) \circ \mathbf{T}_i(z) = \begin{pmatrix} \sum_{i=1}^N P_i^x(x, y) \cdot T_i^x(z) \\ \sum_{i=1}^N P_i^y(x, y) \cdot T_i^y(z) \\ \sum_{i=1}^N P_i^z(x, y) \cdot T_i^z(z) \end{pmatrix}, \quad (1.16)$$

where "o" refers to the Hadamard product. The different in-plane and out-of-plane functions, P_i and T_i respectively, are complex and then they involve a real and imaginary parts.

The previous separated representation leads to a separated representation of its derivatives according to

$$\begin{pmatrix} \frac{\partial E_x}{\partial x} & \frac{\partial E_x}{\partial y} & \frac{\partial E_x}{\partial z} \\ \frac{\partial E_y}{\partial x} & \frac{\partial E_y}{\partial y} & \frac{\partial E_y}{\partial z} \\ \frac{\partial E_z}{\partial x} & \frac{\partial E_z}{\partial y} & \frac{\partial E_z}{\partial z} \end{pmatrix} \approx \sum_{i=1}^N \begin{pmatrix} \frac{\partial P_i^x}{\partial x} & \frac{\partial P_i^x}{\partial y} & P_i^x \\ \frac{\partial P_i^y}{\partial x} & \frac{\partial P_i^y}{\partial y} & P_i^y \\ \frac{\partial P_i^z}{\partial x} & \frac{\partial P_i^z}{\partial y} & P_i^z \end{pmatrix} \circ \begin{pmatrix} T_i^x & T_i^x & \frac{\partial T_i^x}{\partial z} \\ T_i^y & T_i^y & \frac{\partial T_i^y}{\partial z} \\ T_i^z & T_i^z & \frac{\partial T_i^z}{\partial z} \end{pmatrix} = \sum_{i=1}^N \mathbb{P}_i(x, y) \circ \mathbb{T}_i(z), \quad (1.17)$$

allowing the separated representation of all the differential operators appearing within the regularized weak form (1.15).

However, the separated representation just proposed requires that all the model parameters accept a similar separated representation.

Consider the laminate composed of \mathcal{P} layers, each one having uniform properties inside. If H is the total laminate thickness, and assuming for the sake of simplicity and without loss of generality that all the plies have the same thickness h , it results $h = \frac{H}{\mathcal{P}}$. Now, we introduce the characteristic function of each ply $\chi_i(z)$, $i = 1, \dots, \mathcal{P}$:

$$\chi_i(z) = \begin{cases} 1 & \text{if } (i-1)h \leq z < ih \\ 0 & \text{elsewhere} \end{cases}, \quad (1.18)$$

that allows expressing the different properties in the separated form

$$\begin{cases} \mu(x, y, z) = \sum_{i=1}^{\mathcal{P}} \mu_i \cdot \chi_i(z) \\ \epsilon(x, y, z) = \sum_{i=1}^{\mathcal{P}} \epsilon_i \cdot \chi_i(z) \end{cases}, \quad (1.19)$$

being μ_i and ϵ_i the permeability and complex permittivity (the one that involves the permittivity and conductivity) in the i -layer.

1.3.2 Functional approximation

Now, before calculating the different functions involved in the approximation of the electric field, we must approximate them. Because it is assumed that the only heterogeneity applies along the thickness direction when moving from one ply to its neighbor, we can assume a standard continuous nodal approximation of fields E_x and E_y that moreover are continuous at the ply interfaces. For E_z the situation is a bit different (detailed in Appendix A), because it is continuous in the plane but discontinuous across the ply interfaces, where the field jump reads

$$\epsilon_{r,j} E_z(z_j^-) = \epsilon_{r,j+1} E_z(z_j^+), \quad (1.20)$$

where $j \geq 1$ denotes the common interface between plies j and $j+1$, z_j its out-of-plane coordinate, $z_j = jh$, and $E_z(z_j^-)$ and $E_z(z_j^+)$ denote the electric field at both sides of the interface, i.e. $z_j^- = z_j - \nu$ and $z_j^+ = z_j + \nu$, with ν a small enough coefficient ensuring $\nu \ll h$. Discontinuities within the PGD framework were addressed in [31, 22, 14] in mechanical and thermal problems enforcing temperature through interface integrals and using finite elements based separated representations enrichment. However, in the case of electromagnetism, the jump has to be enforced according to material properties and only for one component of the electric field.

Here, continuous bilinear quadrilaterals are considered, Q1 for approximating functions depending on the in-plane coordinates, i.e. $P_i^x(x, y)$, $P_i^y(x, y)$ and $P_i^z(x, y)$. Considering the functions depending on the out-of-plane coordinates, linear continuous 1D finite elements are considered for approximating functions $T_i^x(z)$ and $T_i^y(z)$, ensuring the continuity of $E_x(x, y, z)$ and $E_y(x, y, z)$. However, in order to enforce the discontinuity of $E_z(x, y, z)$ across the ply interfaces, the nodes of the one-dimensional mesh attached to Ω_z located at the ply interfaces and used for approximating T_i^z , are duplicated as proposed in [68, 69, 12, 64]. This simple choice ensures the continuity of E_z in the plane and its discontinuity across the ply interfaces.

1.4 PGD-based discretization

The separated representation construction proceeds by computing a term of the sum at each iteration. Assuming that the first $n - 1$ modes (terms of the finite sum) of the solution were already computed, $\mathbf{E}^{n-1}(x, y, z)$ with $n \geq 1$, the solution enrichment reads:

$$\mathbf{E}^n(x, y, z) = \mathbf{E}^{n-1}(x, y, z) + \mathbf{P}^n(x, y) \circ \mathbf{T}^n(z), \quad (1.21)$$

where both vectors \mathbf{P}^n and \mathbf{T}^n containing functions P_i^n and T_i^n ($i = 1, 2, 3$) depending on (x, y) and z respectively, are unknown at the present iteration. The test function $\bar{\mathbf{E}}^*$ reads $\bar{\mathbf{E}}^* = \mathbf{P}^* \circ \bar{\mathbf{T}}^n + \bar{\mathbf{P}}^n \circ \mathbf{T}^*$.

The introduction of Eq. (1.21) into (1.15) results in a non-linear problem. We proceed by considering the simplest linearization strategy, an alternated directions fixed point algorithm, that proceeds by calculating $\mathbf{P}^{n,k}$ from $\mathbf{T}^{n,k-1}$ and then by updating $\mathbf{T}^{n,k}$ from the just calculated $\mathbf{P}^{n,k}$ where k refers to the step of the non-linear solver. The iteration procedure continues until convergence, that is, until reaching the fixed point $\|\mathbf{P}^{n,k} \circ \mathbf{T}^{n,k} - \mathbf{P}^{n,k-1} \circ \mathbf{T}^{n,k-1}\| < \nu$ (ν being a small enough coefficient), that results in the searched functions $\mathbf{P}^{n,k} \rightarrow \mathbf{P}^n$ and $\mathbf{T}^{n,k} \rightarrow \mathbf{T}^n$. Then, the enrichment step continues by looking for the next mode $\mathbf{P}^{n+1} \circ \mathbf{T}^{n+1}$. The enrichment stops when the model residual becomes small enough.

When \mathbf{T}^n is assumed known, we consider the test function $\bar{\mathbf{E}}^*$ given by $\mathbf{P}^* \circ \bar{\mathbf{T}}^n$. By introducing the trial and test functions into the weak form and then

integrating in Ω_t because all the functions depending on the thickness coordinate are known, we obtain a 2D weak formulation defined in Ω_p whose discretization (by using a standard discretization strategy, e.g. finite elements) allows computing \mathbf{P}^n .

Analogously, when \mathbf{P}^n is assumed known, the test function $\bar{\mathbf{E}}^*$ is given by $\bar{\mathbf{P}}^n \circ \mathbf{T}^*$. By introducing the trial and test functions into the weak form and then integrating in Ω_p because all the functions depending on the in-plane coordinates (x, y) are at present known, we obtain a 1D weak formulation defined in Ω_t whose discretization (using any technique for solving standard ODE equations) allows computing \mathbf{T}^n .

As discussed in [11] this separated representation allows computing 3D solutions while keeping a computational complexity characteristic of 2D solution procedures. If we consider a hexahedral domain discretized using a regular structured grid with N_x , N_y and N_z nodes in the x , y and z directions respectively, usual mesh-based discretization strategies imply a challenging issue because the number of nodes involved in the model scales with $N_x \cdot N_y \cdot N_z$, however, by using the separated representation and assuming that the solution involves N modes, one must solve about N 2D problems related to the functions involving the in-plane coordinates (x, y) and the same number of 1D problems related to the functions involving the thickness coordinate z . The computing time related to the solution of the one-dimensional problems can be neglected with respect to the one required for solving the two-dimensional ones. Thus, the resulting complexity scales as $N \cdot N_x \cdot N_y$. By comparing both complexities we can notice that as soon as $N_z \gg N$ the use of separated representations leads to impressive computing time savings, making possible the solution of models never until now solved, and even using light computing platforms.

1.5 Numerical results

In this section, two laminates are considered with different number of plies, 3 and 29 layers respectively.

1.5.1 3-layer laminate

The first laminate of $0.5\text{m} \times 0.5\text{m} \times 3\text{mm}$ is composed of three plies of similar thicknesses (1mm each), depicted in Fig. 1.1. The in-plane-out-of-plane

representation of the electric field components is expressed from a uniform mesh of the plane domain composed of $50 \times 50 = 2500$ Q1 bilinear finite elements while the thickness is equipped with 1D uniform mesh consisting of 3000 linear elements (1000 elements per layer).

The layers located at the top and bottom are characterized by the electromagnetic properties $\epsilon = 10\epsilon_0$, $\mu = \mu_0$ and $\sigma = 10^{-2}\text{S/m}$, with ϵ_0 and μ_0 the vacuum electrical permittivity and the magnetic permeability respectively. The ply located at the center exhibits a larger electrical conductivity in order to attenuate the electric field, being its associated electromagnetic properties given by $\epsilon = \epsilon_0$, $\mu = \mu_0$ and $\sigma = 10^4\text{S/m}$.

We considered such a laminate in order to enforce both kind of electromagnetic losses, the one related to dielectric losses here mostly occurring in the top and bottom layers, whereas in the central layer the losses are motivated by the larger electrical conductivity. The fact of placing the lowest electrical conductivity layers at top and bottom is to ensure the penetration of electromagnetic waves into the laminate to reach the central layer where they will be attenuated due to the larger electrical conductivity. By locating high conductivity layers at the top and bottom the electromagnetic waves cannot reach the central layer because they will be mostly suppressed in the neighborhood of the laminate boundaries.

Dirichlet boundary conditions are enforced on the whole domain boundary, i.e. $\mathbf{E} \times \mathbf{n}$. The tangential components of the electric field on each face of the layers located on the domain boundary are selected from vector \mathbf{V}

$$\mathbf{V} = \begin{pmatrix} \cos kx + \cos ky \\ \cos ky \\ \tau \cos kx \end{pmatrix}, \quad (1.22)$$

with $k = 20\pi$, $\tau = 1$ in the top and bottom layers and with the appropriate value in the central one for ensuring the field jump according to the Gauss law.

The components of the electric field prescribed as boundary conditions on the laminate are depicted in Figs. 1.2-1.4 for E_x , E_y and E_z respectively. It is important to remember that only tangential components of the electric field are enforced on each domain face (Eq. 1.20).

Figs. 1.5-1.7 depict the evolution along the thickness of the real and imaginary parts of the three components of the electric field. In these figures the

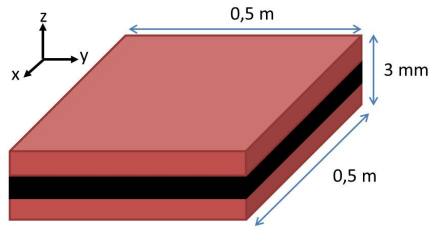
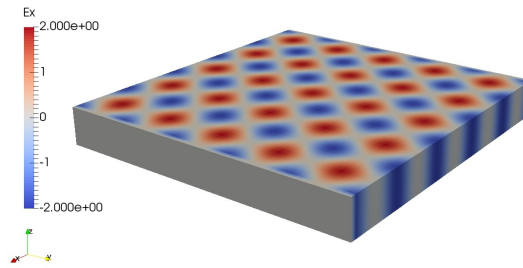


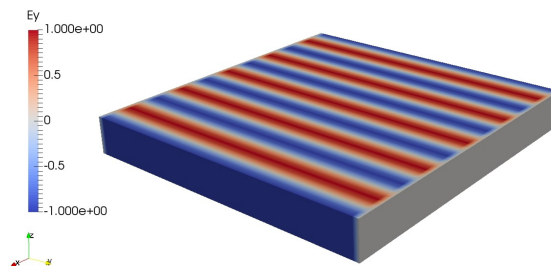
FIGURE 1.1: Three-(thin)-plies laminate

FIGURE 1.2: V_x on $\partial\Omega$

continuity of E_x and E_y , and the discontinuity of E_z across the ply interfaces can be noticed, with a jump magnitude in agreement with the expected value corresponding to the permittivity ratio of adjacent layers according to .

In order to check the effects of unresolved scales related to the penetration depth, we consider a coarser mesh along the thickness composed of 30 elements (10 per layer). It can be noticed that the solution is significantly degraded with respect to solution obtained with the finer mesh as the comparison of Figs. 1.5-1.7 and Figs. 1.8-1.10 reveals, in particular the out-of-plane component of the electric field E_z .

To better appreciate the unresolved boundary layer (the penetration depth being $\delta = \sqrt{2/\omega\mu_0\sigma} \approx 0.1\text{mm}$), Figs. 1.11-1.13 depict the real part of

FIGURE 1.3: V_y on $\partial\Omega$

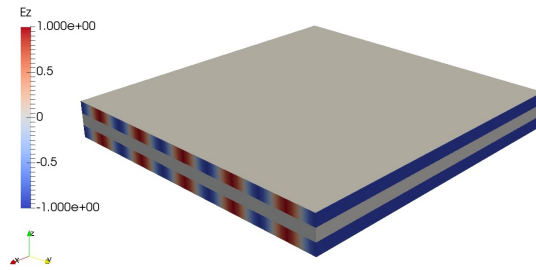


FIGURE 1.4: V_z on $\partial\Omega$

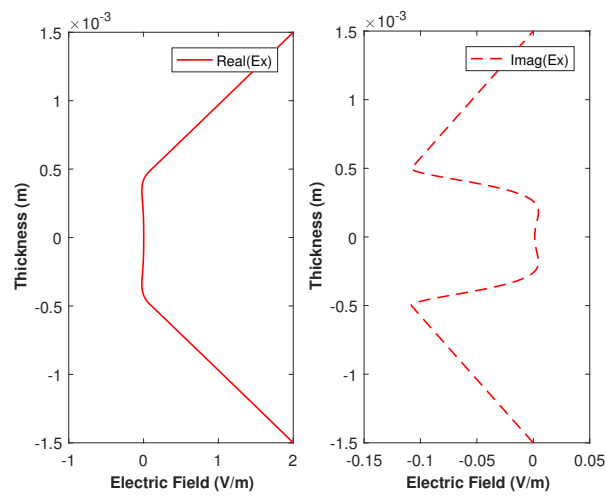


FIGURE 1.5: Electric field along the plate thickness, $E_x(0.25, 0.25, z)$

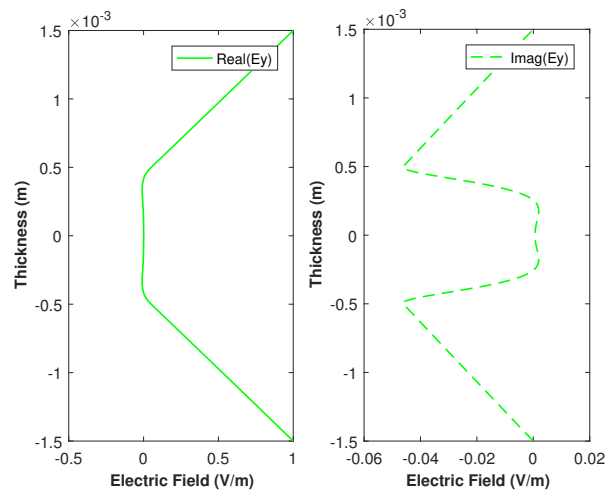


FIGURE 1.6: Electric field along the plate thickness, $E_y(0.25, 0.25, z)$

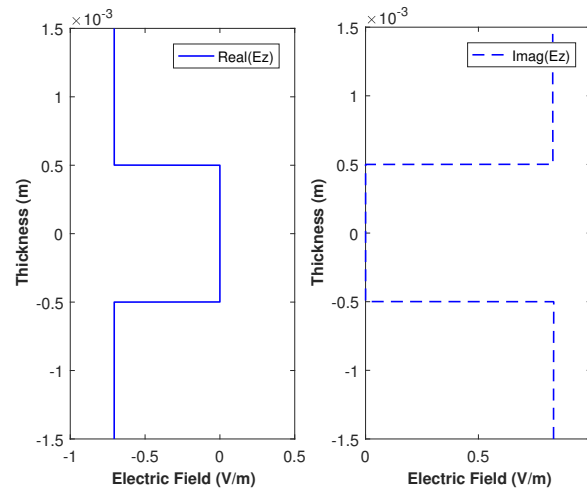


FIGURE 1.7: Electric field along the plate thickness, $E_z(0.25, 0.25, z)$

.

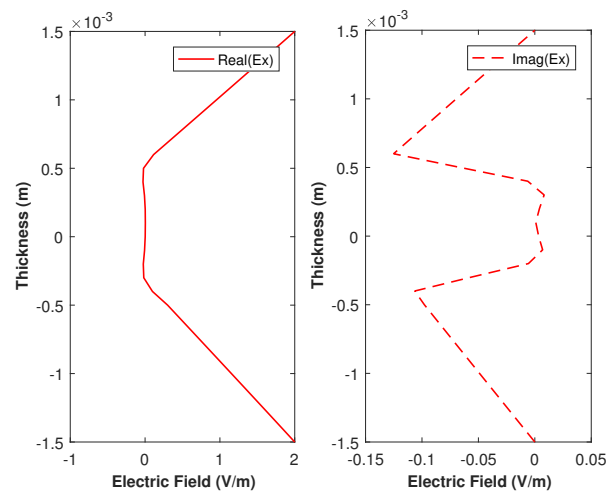


FIGURE 1.8: Electric field along the plate thickness, $E_x(0.25, 0.25, z)$ when considering a coarser mesh in the thickness

.

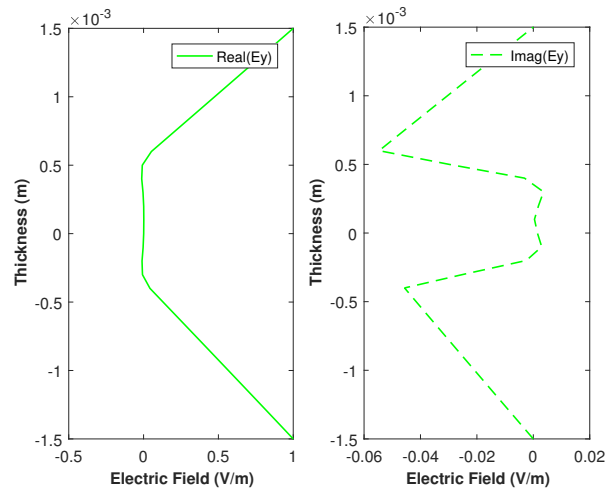


FIGURE 1.9: Electric field along the plate thickness, $E_y(0.25, 0.25, z)$ when considering a coarser mesh in the thickness

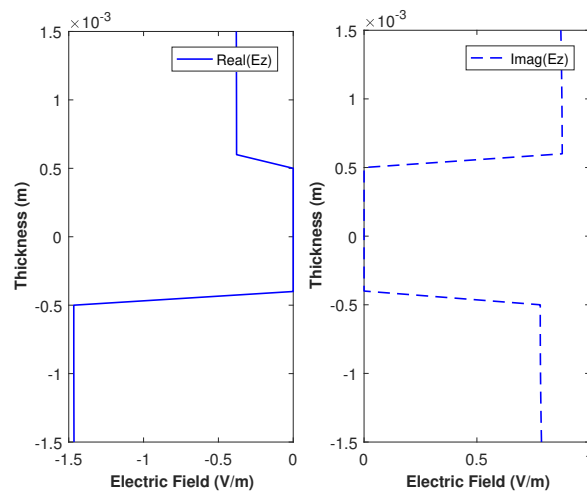


FIGURE 1.10: Electric field along the plate thickness, $E_z(0.25, 0.25, z)$ when considering a coarser mesh in the thickness

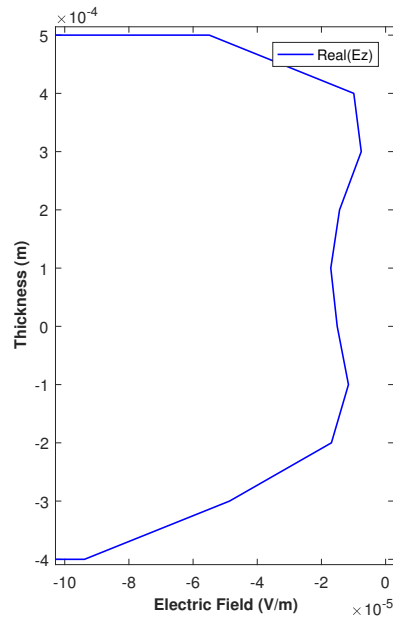


FIGURE 1.11: Electric field along the central layer thickness when considering a mesh in the thickness consisting of 30 elements

$E_z(0.25, 0.25, z)$ in the central layer.

It can be noticed that for resolving all the scales extremely fine meshes are required along the thickness direction, involving about thousand elements that with the thousands involved in the in-plane resolution imply meshes involving millions of elements (extremely distorted) when proceeding with standard finite elements. When using the in-plane-out-of-plane separated representation, in-plane and out-of-plane meshes become independent avoiding issues related to mesh distortion. On the other hand the problems defined in the thickness are one-dimensional and consequently their computational cost is almost negligible with respect to the solution of in-plane problems. Thus, finally the high-resolution 3D solution is obtained while keeping the computational complexity similar to the one characteristic of the solution of 2D problems (the one defined in the plane).

In order to emphasize the location of both kind of losses, the dielectric one and the one related to eddy currents, Fig. 1.14 represents the density of both losses, where as expected, the dielectric ones locate at the external layers, whereas the one related to eddy current effects locates in the central layer and close to the interfaces where the electric field is attenuated (the penetration depth).

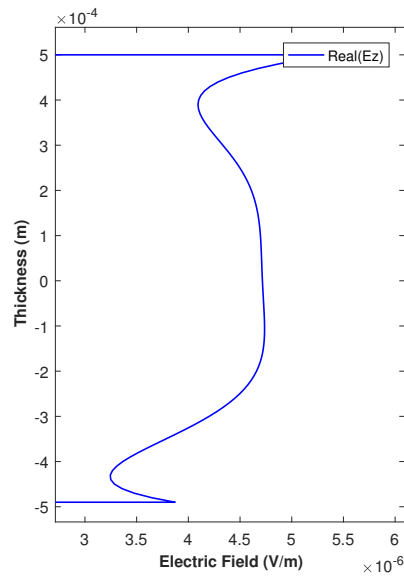


FIGURE 1.12: Electric field along the central layer thickness when considering a mesh in the thickness consisting of 300 elements

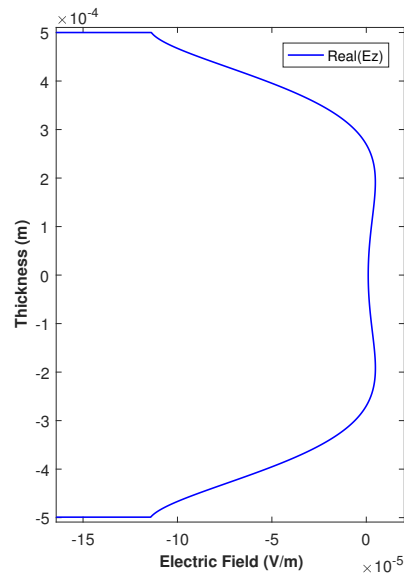


FIGURE 1.13: Electric field along the central layer thickness when considering a mesh in the thickness consisting of 3000 elements

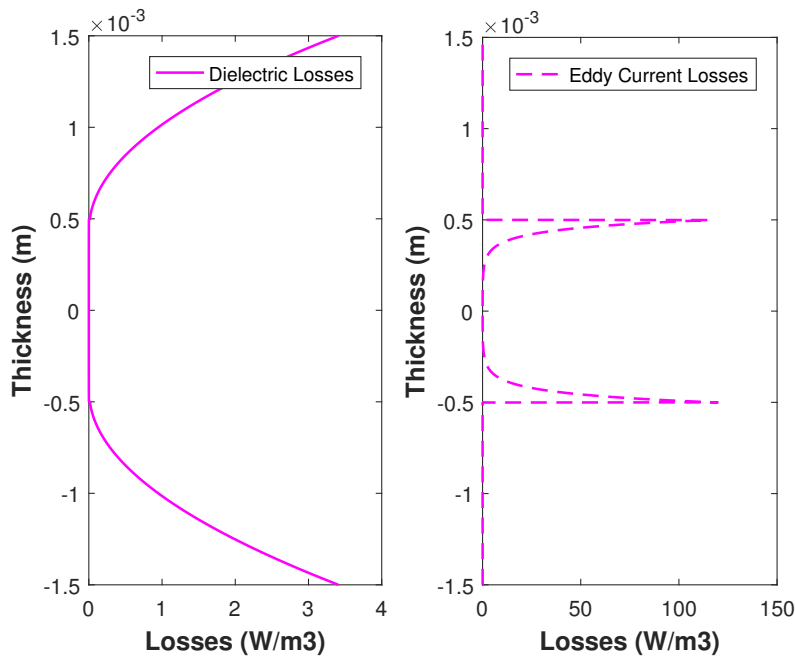


FIGURE 1.14: Electromagnetic losses: (left) dielectric and (right) eddy current

1.5.2 29-layer laminate

The second laminate of $0.5\text{m} \times 0.5\text{m} \times 2.9\text{mm}$ is composed of 29 plies of similar thicknesses (0.1mm each) where two different materials are alternatively placed as illustrated in Fig. 1.15. The in-plane-out-of-plane representation of the electric field components is expressed from a uniform mesh of the plane domain composed of $50 \times 50 = 2500$ Q1 bilinear finite elements while the thickness is equipped with 1D uniform mesh consisting of 1450 linear elements (50 elements per layer).

The layers in red in Fig. 1.15 are characterized by the electromagnetic properties $\epsilon = 5\epsilon_0$, $\mu = \mu_0$ and $\sigma = 0\text{S/m}$, with ϵ_0 and μ_0 the vacuum electrical permittivity and the magnetic permeability respectively. The remaining plies exhibit a larger electrical conductivity in order to attenuate the electric field, being its associated electromagnetic properties given by $\epsilon = \epsilon_0$, $\mu = \mu_0$ and $\sigma = 1\text{S/m}$. The boundary conditions are the same that were enforced when addressing the solution of the three-layer laminate.

Figs. 1.16-1.18 depict the evolution along the thickness of the real and imaginary parts of the three components of the electric field. In these figures the continuity of E_x and E_y , and the discontinuity of E_z across the ply interfaces can be noticed, with a jump magnitude in agreement with the expected value.

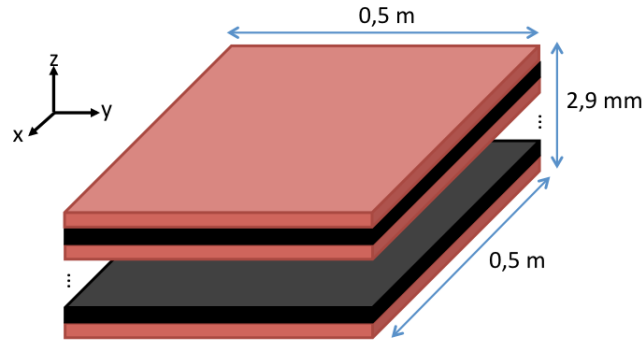
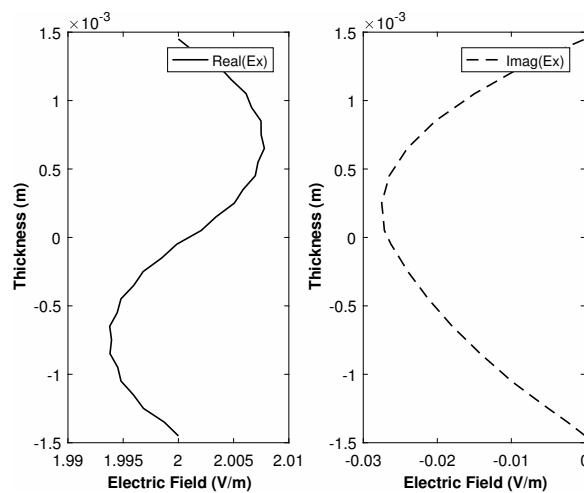


FIGURE 1.15: 29-ply laminate

FIGURE 1.16: Electric field along the plate thickness, $E_x(0.25, 0.25, z)$

It is important to note that such a high-resolution remains out-of-reach when using standard 3D mesh-based discretization techniques, whereas the separated representation allows a very accurate solution, cheap and fast from the computational view point (the solution was obtained in 20 seconds using a standard laptop).

1.6 Discussion and conclusions

This first part of the work proposes the modeling and simulation of the electric field addressing the propagation of electromagnetic waves in composite laminates. The PGD method and its in-plane-out-of-plane decomposition have been applied and adapted to ensure convergence to the proper solution

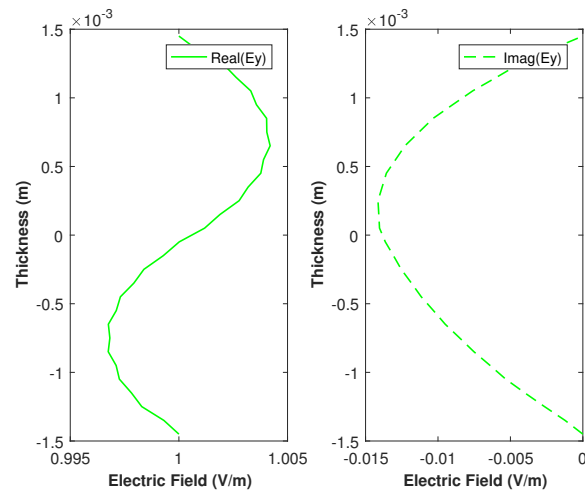


FIGURE 1.17: Electric field along the plate thickness, $E_y(0.25, 0.25, z)$

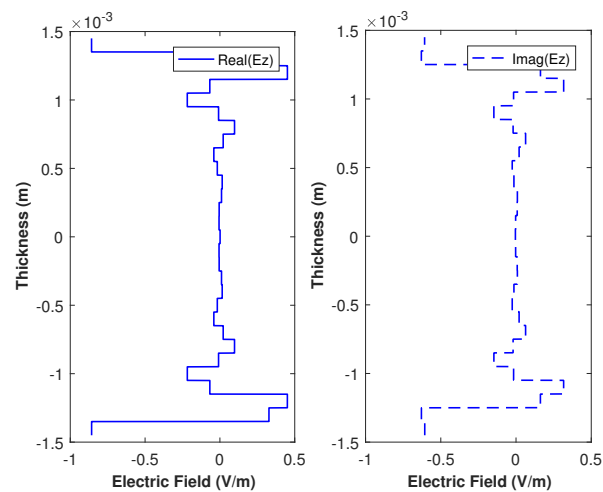


FIGURE 1.18: Electric field along the plate thickness, $E_z(0.25, 0.25, z)$

of the given problem. Because its inherent throughout-its-thickness high-resolution, direct consequence of the in-plane-out-of-plane separated representation, the reached resolution falls beyond the capabilities of standard and well experienced mesh-based discretization techniques. By using it, micrometric re-resolutions can be easily reached when addressing usual composite structural parts. It allows zooming at regions exhibiting high variations of the solution, as for example the wave attenuation when reaching a conductive layer, that localizes the solution in an extremely narrow layer, whose accurate representation remains out of reach for standard discretization techniques.

The second advantage in using the proposed technique is related to the facility to enforce the jump of the normal component of the electric field across two layers exhibiting different electromagnetic properties. For that purpose the field approximation is able to produce jumps at the laminate interfaces.

When using a high-resolution discretization based on the in-plane-out-of-plane separated representation, the double-curl electromagnetic formulation worked quite well as soon as boundary conditions were regular enough. However as soon as complex Dirichlet boundary conditions were enforced a lack of convergence was noticed and the computed solutions were almost wrong. In fact the Gauss law was not fulfilled at the discrete level and for that reason a regularized formulation was considered, that allowed ensuring the solution convergence.

These three issues are subtly entangled. It is important to note that when solving the electromagnetic problem in the laminate, the z -component of the electric field E_z is not enforced on the top and bottom surfaces. Moreover, at the ply interfaces E_z jumps according to the Gauss law, and then, if the field attenuation when the wave reaches the central (conductive) layer is not accurately described (approximated), the solution E_z becomes wrong almost everywhere. Thanks to the proposed method, these linked issues are resolved.

Chapter 2

Simulation of the Microwave Heating of a Composite Preform

Contents

2.1 Introduction	27
2.1.1 Processing composite materials	28
2.1.2 Composite heating simulation with microwaves	30
2.2 Coupling electromagnetics and heating	31
2.2.1 Heat mechanisms	31
2.2.2 Numerical implementation	32
2.3 Electric field distribution in an oven cavity	33
2.3.1 Comsol Multiphysics modeling	33
2.3.2 Extracting the electromagnetic boundary conditions	36
2.4 Numerical results	37
2.4.1 Fibers choice: which material for MW processing ?	38
2.4.2 Influence of the plies orientation	44
2.4.3 Mold design to ensure uniform heating	46
2.4.4 Uncertainty on the dielectric properties	51
2.4.5 Placement of the tool in the oven cavity	53
2.5 Discussions and conclusions	55

2.1 Introduction

Structural parts made of composite materials tend to represent an increasing volume of production in the industry. This is due to their combination of

high mechanical properties and low mass. The production in 2015 represents approximately 10 millions tons of composite materials processed throughout the globe leading to a market of 78 billion dollars [33]. Every year, the composite market is expected to grow between 5 and 6 percents. This everlasting growth is due to the increasing development of composite materials processes, structures and a strong will from the transportation industry to incorporate such parts in their products. Therefore, the main industries where composite parts are employed are the transportation industry (automotive, aeronautic, railway, nautical) but also civil construction, the energy sector with the development of sustainable energy, leisure industry and medical equipment.

2.1.1 Processing composite materials

Mastering the service life of the product is the key element for a growing industry. The life cycle of a composite material part is divided in four main steps which are the elaboration of semi-manufactured products, the processing of the material to form the final product, the use of the part and, finally, the recycling of the product. During all of the four phases, heat is applied to the part. Looking at the second step of the life cycle of a composite material, conventional processing methods used to produce a finished part usually involve the application of heat to the material by convection heating of the tool and composite in an oven (pressurized or non-pressurized), or conductive heating of mold and platens through heating elements. Looking at the autoclave process, the air in the chamber and the mold are heated first and then, by conduction, heat energy is transferred through the thickness of the part. The duration of the process relies on the rate of the heat flow in the material depending on the thermal properties of the composite material. Therefore, the edges and corners are heated to the desired temperature before the core of the part. This uneven rate of heating leads to induced mechanical stresses which will damage the final part. In order to minimize these stresses, specific care has to be given to the heating rate such that the time scale of the process is larger than the time needed for the heat to diffuse in the part. In an industrial context, such surface heat transfer is therefore a real challenge regarding temperature control and process duration optimization.

As a consequence, innovative processes have been introduced as for example heat gain using magnetic hysteresis [79], dielectric heating [50] and induction

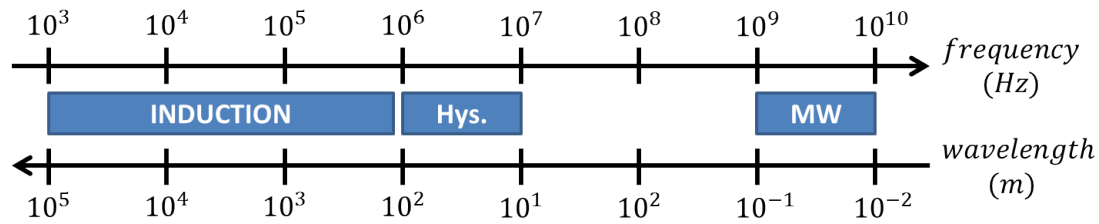


FIGURE 2.1: Composite material processes involving electromagnetics and their frequency range

heating [6] – each of them operating at a specific frequency range as displayed on Fig. 2.1. Conversely to the traditional heating methods which depends on surface heating (conduction and/or convection), these innovative processes rely on volumetric heating of the part. Thermal energy is transferred thanks to the interaction between the electromagnetic field and the material which can absorb it more or less according to the frequency used and its dielectric properties.

Thanks to the food industry, the microwave technology has been intensively developed and numerous experimental works has been carried in order to expand this heating process of composite material [87, 89, 52, 48]. The microwave heating technique has been investigated not only by academics but also by companies patenting their developments on the manufacturing process [54] or on new tools specifically designed for microwaves [9]. On the industrial point of view, interesting possibilities on the reduction of the manufacturing cost have been highlighted [27] as a result of a shorter cycle time [40], a better control of the temperature [93] and reduced induced stresses in the manufactured parts [51]. Volumetric heating also enables the possibility of localized heating directly towards the part to be processed avoiding heating of the surrounding air or tool, thus maximizing the energy efficiency of the process. The localized heating also leads to time benefits when it comes to handling the part after heating: the surrounding air and the mold – transparent to microwaves – have not been heated and less time is needed in waiting for the displacement of the manufactured part as for a domestic microwave oven. Regarding the quality of the part, comparable mechanical properties are shown between parts manufactured using the MW technology and parts made with a traditional curing system [62, 47].

2.1.2 Composite heating simulation with microwaves

The full simulation of the heating process of a composite part in a microwave oven cavity requires to take into account the multiple complexities of the process. On the one hand, the problem to be solved includes several physics: electromagnetics, thermic and kinetics. In this chapter, the coupling of the first two is investigated while the third will be discussed in the Chapter 3. On the other hand, composite material and microwave process imply a multiscale problem: from one ply of composite material (approximately $150\mu m$ thick) to the dimensions of the oven cavity (up to $1m$ long). These multi-physics - multiscale aspects have to be taken into account in the simulation in order to represent fully the phenomena occurring during the process.

Previous works proposed such simulations for induction heating application [7, 84] but when considering composite processing at microwave frequency, only very simplified models have been built. In [83, 5], the temperature field is investigated only in a 1D approximation to capture the temperature gradient in the thickness of a composite plate. [50] does not take into account the interaction between the electromagnetics waves and the composite material as all the incident wave is considered to be absorbed by conductive plates before reaching the part to be processed. Commercial softwares are also available to conduct electromagnetics-thermal coupled simulations as for example Comsol Multiphysics [24, 4] or CEM One [16] but such software is constrained regarding the discretisation refinement in order to represent a thin multilayer component.

In this chapter, a coupled electromagnetic and thermal model is presented. The electromagnetic simulation is carried out using the in-plane-out-of-plane separated representation within the PGD framework (as depicted in Chap. 1) and coupled with a thermal solver based on the same separated representation to keep the richness of the out-of-plane discretisation. After the description of the simulation tool, several studies are carried to investigate the heating of composite materials under a microwave field.

2.2 Coupling electromagnetics and heating

2.2.1 Heat mechanisms

Modeling the heat mechanisms under the influence of an electromagnetic field consists in solving the heat equation, associated with the proper boundary conditions and heat sources. Considering the processing of a composite part in an oven cavity, the domain of interest here is the mold and part ensemble. The conduction mechanism is expressed as a heat flux ϕ between two points of the domain (Eq. 2.1)

$$\phi = -\lambda \nabla T \quad (2.1)$$

with λ the thermal conductivity and T the temperature field

Natural convection is applied in the oven cavity on the surface of the mold which translates into boundary condition on the whole simulation domain. The normal heat flux to the surface ϕ_s reads

$$\phi_s = -\lambda \frac{\partial T}{\partial \mathbf{n}} = h(T - T_\infty) \quad (2.2)$$

with h the heat transfer coefficient and T_∞ the ambient temperature.

Using the electromagnetic formulation described in Chap. 1, the losses Q_{MW} induced by microwaves are calculated in any points of the domain and can be introduced in the heat equation. The temperature field evolution $T(x, y, z, t)$ in the domain of interest is characterised by the resulting Eq. 2.3

$$\rho C_p \frac{\partial T}{\partial t} = \nabla \cdot (\lambda \nabla T) + Q_{MW}(x, y, z) \quad (2.3)$$

with ρ the density and C_p the specific heat, under the boundary conditions in the whole external surface (Eq. 2.2).

A strong coupling between the two solvers involved in the process simulation for the electromagnetics and the heat equation involves taking into account the evolution of all of the material properties according to the temperature. The key for such simulation is to take into account the difference time scales between the electromagnetic and the thermal phenomena [90]. The establishment of a steady state for the electromagnetic field is in the order of magnitudes of nanoseconds whereas the time scale of thermal diffusion requires seconds. Therefore, the strategy to be implemented is a three-stage

iterative process where the first stage consists of solving the electromagnetic problem for a certain set of dielectric material properties, the second stage is solving the temperature field using the derived losses from the previous step and the last stage is going back to the electromagnetic simulation with the updated set of dielectric properties according to the new temperature distribution. This process needs to be repeated for each time interval after which an upgrade of the material properties is required.

In order to implement such thermal coupling, one aspect is essential: knowing the evolution of the dielectric properties of the material with the temperature. Unfortunately, as the simulation of composite heating with microwave is recent, we can observe a lack of these data in the literature as few measurement works have been done [1, 2, 55]. Finding the value of dielectric permittivity and electric conductivity is already a real challenge and no models or experimental measurements known to us today have been developed to follow the temperature dependency of the dielectric properties for composite materials. As a consequence, for the following studies, it will be considered that the material properties are constant in the range of temperature of the process - from 293K to approximately 473K.

2.2.2 Numerical implementation

From all the considerations and hypothesis expressed in the modeling of the heat mechanisms, the weak form to be solved in the simulation can be written. Based on the heat equation and boundary conditions (Eqs. 2.3 and 2.2), the weak form reads:

$$\int_{\Omega} T^* \rho C_p \frac{\partial T}{\partial t} d\mathbf{x} + \int_{\Omega} \nabla T^* \lambda \nabla T d\mathbf{x} + \int_{\partial\Omega} T^* h T d\mathbf{x} = \int_{\Omega} T^* Q_{MW} d\mathbf{x} + \int_{\partial\Omega} T^* h T_{\infty} d\mathbf{x}, \quad (2.4)$$

for all test functions T^* regular enough.

As for the electromagnetic formulation, the in-plane-out-of-plane representation within the PGD framework is adopted here for several reasons, in addition to the obvious easy choice of having the same numerical technique between the two solvers. Using such representation is of major interest when it comes to the investigation of the effect of each ply on the temperature distribution. All the richness of the electromagnetic simulation is transferred

through the losses term Q_{MW} producing volumic heat sources in the composite part. In addition, the PGD numerical technique allows not only the separation between in-plane (x, y) and out-of-plane z coordinates but also a separation along the time t coordinate. Thus, the time integration is performed in a non-incremental way meaning the whole temperature history is computed simultaneously. This ability allows impressive CPU time savings.

In the PGD context, the domain is decomposed as $\Omega = \Omega_p \times \Omega_t \times \Omega_\theta$, with $\Omega_p \subset \mathbb{R}^2$, $\Omega_t \in \mathbb{R}$ and $\Omega_\theta \in \mathbb{R}$ and the temperature field writes:

$$T(x, y, z, t) \approx \sum_{i=1}^N P_i(x, y) \cdot T_i(z) \cdot \Theta_i(t) \quad (2.5)$$

where P_i and T_i are respectively the in-plane and out-of-plane functions and Θ_i is the time function.

2.3 Electric field distribution in an oven cavity

The domain of interest in the coupled solver described in previous section is restricted to the mold and part ensemble and it is linked to its environment through the electromagnetic and thermal boundary conditions. In order to understand the heating process of a composite part in an oven cavity, the electromagnetic boundary conditions have to be representative of an actual electric field in a microwave oven. In order to perform the electromagnetic simulation in the oven and get such boundary conditions, an external software is needed. In this chapter, we will be using Comsol Multiphysics [24].

2.3.1 Comsol Multiphysics modeling

Comsol Multiphysics' Electromagnetic Waves module solves the electric field propagation using the Finite Element Method. Simulation results from Comsol software are used in Section 2.4.5. In this case, the geometry of the oven is presented in Fig. 2.2 where the main box represents the oven cavity with inside the mold and composite part which consists of a plate. The short waveguide on the top right hand edge produces a TE₁₀ electromagnetic field (Eq. 2.6) which propagates in the cavity,

$$\mathbf{n} \times \mathbf{E} = \begin{pmatrix} 0 \\ \sin\left(\frac{\pi x}{a}\right)e^{-jk_z z} \\ 0 \end{pmatrix}, \quad (2.6)$$

where a is the width of the waveguide and k_z the propagation constant.

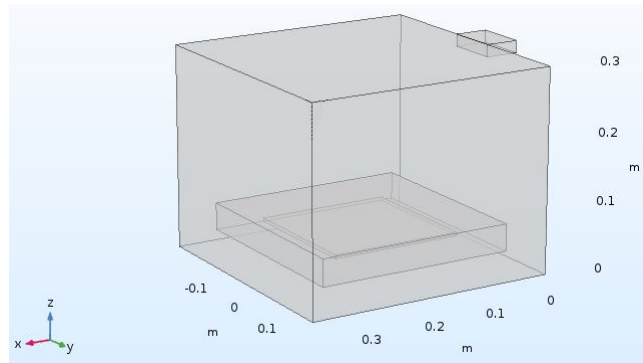


FIGURE 2.2: Oven cavity geometry

The walls of the oven are made of metal and associated to an impedance boundary condition. In order to run a simulation in Comsol, each ply of the composite plate cannot be represented. The geometry is meshed automatically by Comsol based on material properties and distortion ratios. The mesh of the plate contains only one element in the thickness and approximately 1000 tetrahedra elements in total (Figs. 2.3 and 2.4). As far as the dielectric properties of the composite part are concerned, they have to be homogenised using the method described in [39].

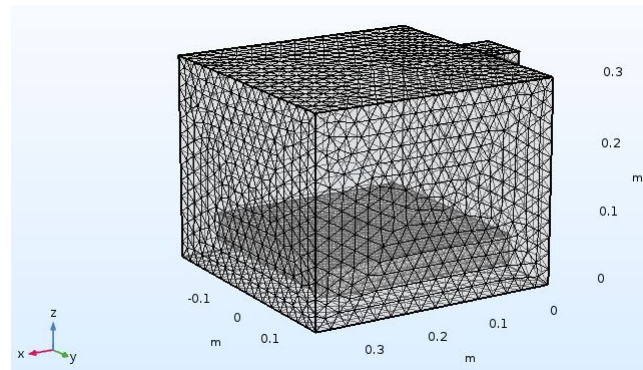


FIGURE 2.3: Mesh generated by Comsol for the oven

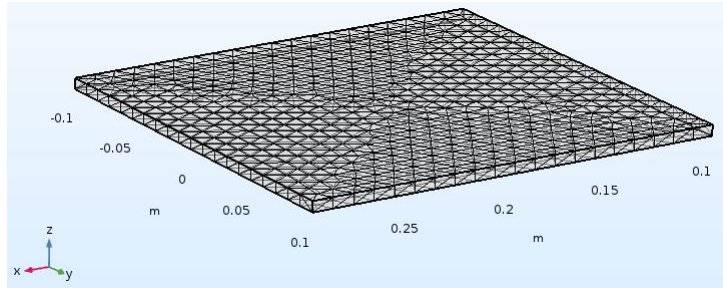
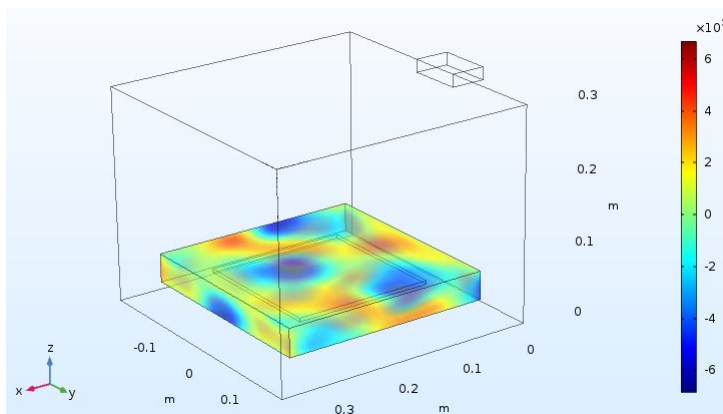
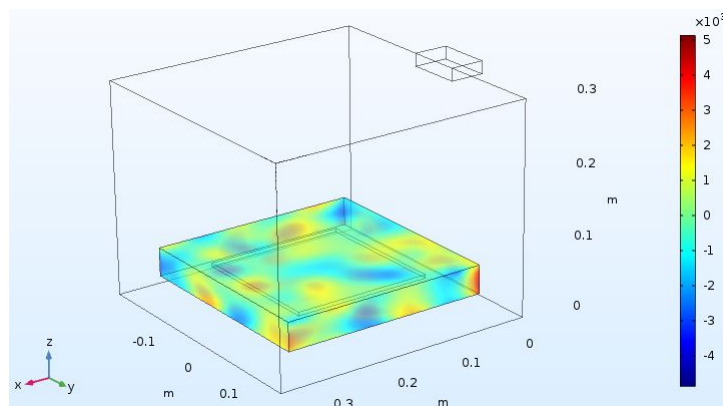


FIGURE 2.4: Mesh generated by Comsol for the composite plate

Solving the electromagnetic problem under Comsol provides the three components of the electric field E_x , E_y and E_z (Figs. 2.5, 2.6 and 2.7) on the surface of the mold which can then be exported and used as boundary conditions in the PGD-based solver.

FIGURE 2.5: Example of E_x component of electric field on the mold surfaceFIGURE 2.6: Example of E_y component of electric field on the mold surface

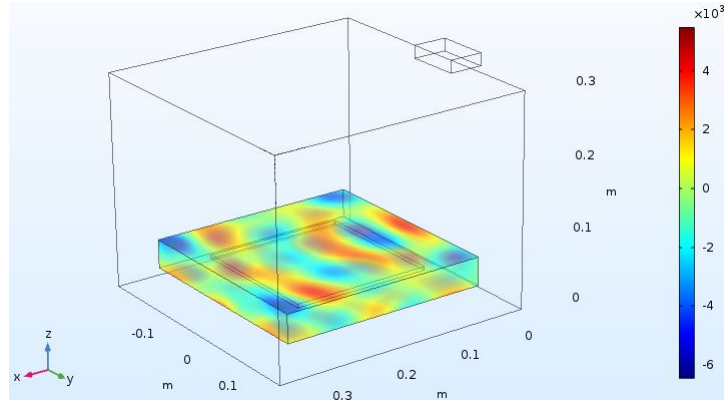


FIGURE 2.7: Example of E_z component of electric field on the mold surface

2.3.2 Extracting the electromagnetic boundary conditions

Comsol Multiphysics allows the exportation of results data. Once the simulation is over, the electric field \mathbf{E} can be exported along with the external mesh (nodes and connectivity table) of the mold on which it is calculated. Projection of the electric field from the external surface mesh (triangular elements) on the PGD mesh (combination of quadrilateral and bar elements) is performed. This step is the most time-consuming depending on the refinement of both meshes. For example, projection from a mesh containing 8400 triangular elements to a 10000 Q1 \times 160 bar elements takes approximately 30 minutes whereas when the external mesh is made of 18000 elements and PGD mesh is 14400 Q1 \times 270 elements, it takes 1 hour. Once the electric field is calculated on the PGD mesh, it has to be decomposed to obey to the separated representation. For the top and bottom surfaces of the mold, the in-plane-out-of-plane separation is straightforward:

$$\mathbf{E}_{top/bottom}^{PGD} = \mathbf{E}_{top}^{Comsol}(x, y) \cdot Z_{top}(z) + \mathbf{E}_{bottom}^{Comsol}(x, y) \cdot Z_{bottom}(z) \quad (2.7)$$

with

$$Z_{top}(z) = \begin{cases} 1 & \text{if } z = z_{max} \\ 0 & \text{elsewhere} \end{cases} , \quad (2.8)$$

and

$$Z_{bottom}(z) = \begin{cases} 1 & \text{if } z = z_{min} \\ 0 & \text{elsewhere} \end{cases} . \quad (2.9)$$

But for the four sides of the mold, the in-plane-out-of-plane separation requires the use of an SVD - Singular Value Decomposition - and the extraction of the dominant modes to represent closely enough the electric field on the surface. For example, the SVD for the $x = x_{min}$ side of the mold reads

$$\mathbf{E}_{side, N_y \times N_z}^{Comsol} = U_{N_y \times N_y} \Sigma_{N_y \times N_z} V_{N_z \times N_z}^* \quad (2.10)$$

is the decomposition given by the SVD where N_y and N_z are the number of nodes in the y and z directions respectively. $\Sigma_{N_y \times N_z}$ is a rectangular diagonal matrix containing the singular values of $\mathbf{E}_{side, N_y \times N_z}^{Comsol}$ listed in descending order.

The separated field on the boundary reads:

$$\mathbf{E}_{side}^{PGD} = \sum_{i=1}^N \Sigma_{i,i} \cdot U_i(y) \circ V_i(z) \quad (2.11)$$

where $\Sigma_{i,i}$ is the i-th singular value, $U_i(y)$ the i-th column of matrix U and $V_i(z)$ the i-th column of matrix V . The number of terms N is chosen such as $\Sigma_{N,N} \ll \Sigma_{1,1}$.

With the decomposition of the boundary conditions, the PGD-based electromagnetic solver can be launched.

2.4 Numerical results

In this section, we consider several cases in order to investigate the impact of some parameters of the microwave heating process applied on composite materials. In all the following cases, the geometry of the domain under study is composed of a mold transparent to microwave and the composite part: a 21-layer plate as shown on Fig. 2.8.

Five test cases are treated in the following sections:

- Fibers choice: glass VS carbon
- Orientation of the fibers: plies stacking sequence
- Mold design for a more homogenized heating
- Influence of the uncertainty on the dielectric properties
- Variation of the electromagnetic boundary conditions

In order to achieve these studies, the dielectric and thermal properties of the materials involved are summarised in Table 2.1.

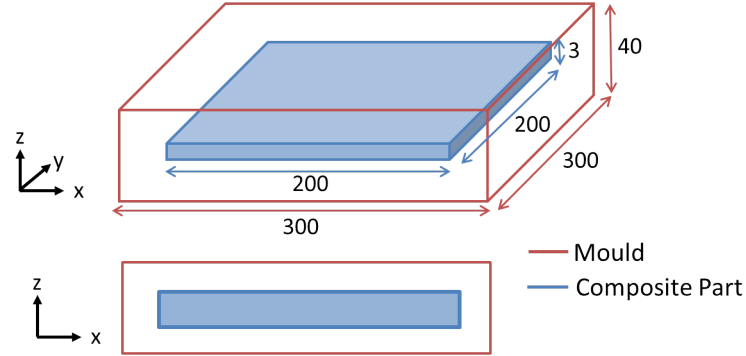


FIGURE 2.8: Test case geometry with composite and mold - all dimensions are given in mm

Dirichlet boundary conditions are enforced on the whole domain boundary, i.e. $\mathbf{E} \times \mathbf{n}$. For the first four cases, the tangential components of the electrical field on each face of the layers located on the domain boundary are selected from vector \mathbf{V} ensuring a representation of the heterogeneity of the field in an oven cavity. The convective boundary condition for the thermal solver is enforced on the whole domain boundary with $h = 10W/m^2K$ and $T_\infty = 293K$,

$$\mathbf{V} = \begin{pmatrix} \cos kx + \cos ky \\ \cos ky \\ \tau \cos kx \end{pmatrix}, \quad (2.12)$$

with $k = 20\pi$ and $\tau = 1$ as there are no discontinuities on the domain boundary (mold material).

2.4.1 Fibers choice: which material for MW processing ?

Microwave heating relies on one phenomena: dielectric heating. Depending on the material properties, losses inducing heating will be more or less important. Therefore, one can ask if all types of composite material are suited to be processed by microwave heating. In this section, the two main fiber types will be investigated by comparing the heating of a glass-based composite and a carbon-based composite. As shown in Table 2.1, these two materials have very different properties: one ply of GFRP is isotropic whereas CFRP is anisotropic, electrical conductivity is much higher for CFRP as well as its

TABLE 2.1: Dielectric and thermal material properties - GFRP and CFRP respectively stand for Glass and Carbon Fiber Reinforced Polymer, \parallel and \perp respectively characterise the material property in the longitudinal and transversal directions of the fibers of the ply

Materials	GFRP [26, 77]	CFRP [29, 94]	Mold [41]	Conductive layer
$\rho(kg/m^3)$	1900	1550	1600	7000
$C_p(J/kgK)$	900	1050	800	400
$\lambda(W/mK)$	0.5	$\lambda_{\parallel} = 9$ $\lambda_{\perp} = 1$	0.4	15
ϵ_r (No Units)	4.5	$\epsilon_{\parallel} = 80$ $\epsilon_{r\perp} = 10$	3	1
$\sigma(S/m)$	0.006	$\sigma_{\parallel} = 4170$ $\sigma_{r\perp} = 6$	0.016	10^6
μ_r (No Units)	1	1	1	1

thermal conductivity. From this observation, we should expect great difference in the heating pattern of these materials.

The composite plate is composed of unidirectional - UD - fabrics. The stacking of the composite plies is the following: $[(0^\circ/90^\circ)_5 0^\circ (90^\circ/0^\circ)_5]$, where 0° stands for a ply where the longitudinal orientation of the fiber is along the x direction whereas 90° is along the y direction. The thermal simulation is carried on for a duration of 20 minutes with a constant power source along time.

The in-plane-out-of-plane representation of the electric and temperature field is simulated from the combination of the plane domain mesh (2D mesh) and the out-of-plane mesh (1D mesh). In the case of GFRP, the 2D mesh is uniform and composed of $90 \times 90 = 8100$ Q1 bilinear finite elements. For CFRP, the very high conductivity in the fiber direction leads to a very small penetration depth. Thus, the 2D mesh has to be refined at the edges of the composite domain. The 2D mesh is non-uniform and composed of $120 \times 120 = 14400$ elements. The 1D mesh contains 600 linear elements.

Figs. 2.9-2.10 present the propagation of the electric components E_x , E_y and E_z along the y direction for the carbon and glass cases. It is noticed that for the carbon composite, the electric field intensity is sharply reduced when passing from mold to composite part whereas in the glass composite, the electric field propagates with comparable intensity.

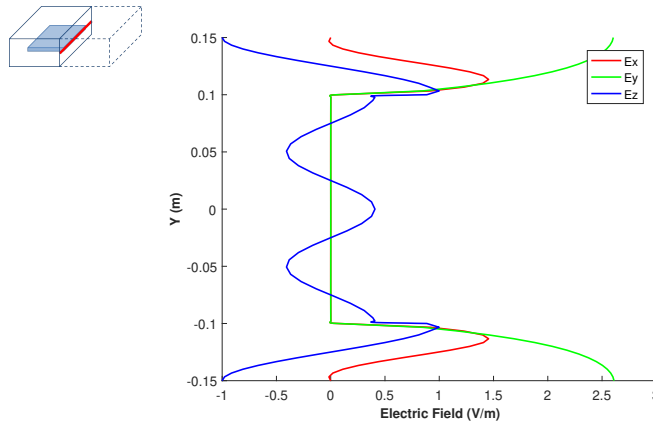


FIGURE 2.9: Carbon case - electric field along $(x_{middle}, y, z_{middle})$

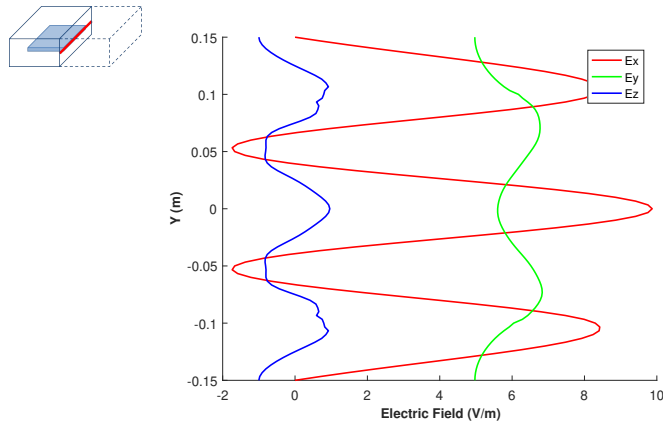


FIGURE 2.10: Glass case - electric field along $(x_{middle}, y, z_{middle})$

The evolution of the electric field along the the thickness of the domain is depicted on Figs. 2.11-2.12. The discontinuity of E_z component is observed with a notable difference between the two cases: $\frac{\epsilon_{r,glass}}{\epsilon_{r,mold}} = 1.5$ and $\frac{\epsilon_{r,carbon\perp}}{\epsilon_{r,mold}} = 3.3$. E_z and E_y components also vanishes in the carbon composite.

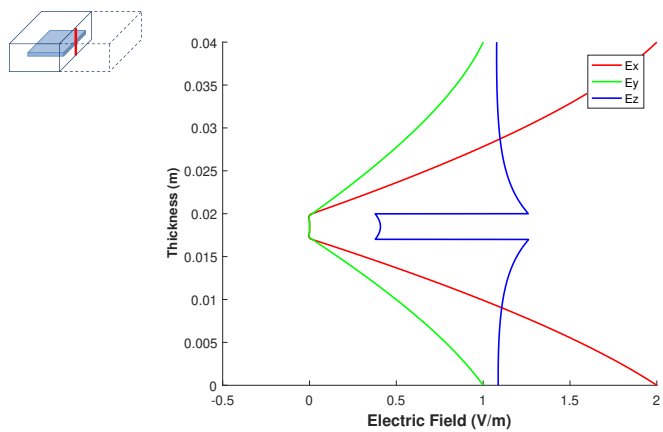


FIGURE 2.11: Carbon case - electric field along the thickness $(x_{middle}, y_{middle}, z)$

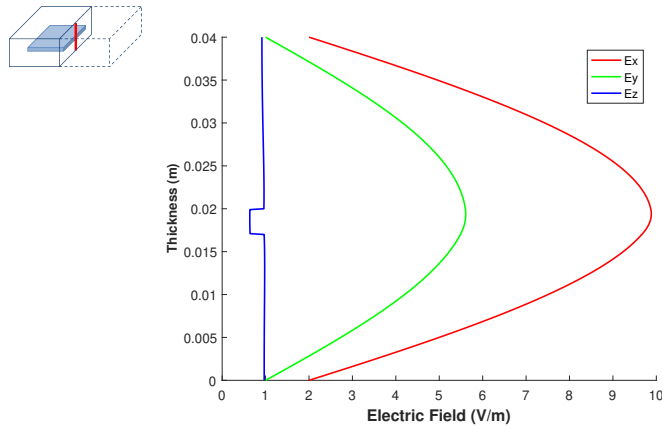


FIGURE 2.12: Glass case - electric field along the thickness
($x_{middle}, y_{middle}, z$)

The temperature field in middle (x, y) section for carbon and glass is represented in Figs. 2.13-2.14. It can be highlighted that higher temperatures are reached in the glass part but it displays a higher heterogeneity of heating with more than 100°C difference between two locations in the part.

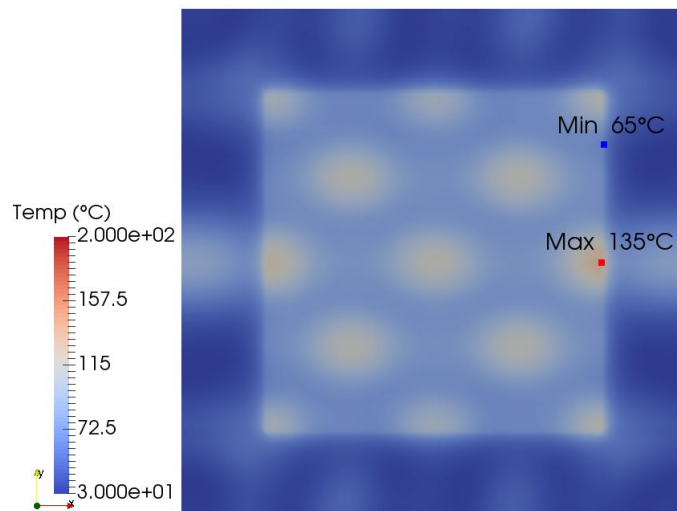


FIGURE 2.13: Carbon case - temperature distribution in the middle section (x, y, z_{middle}) after heating for 20 min

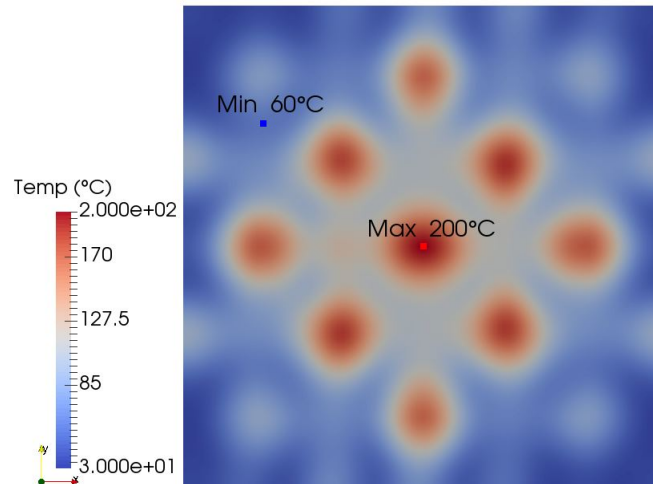


FIGURE 2.14: Glass case - temperature distribution in the middle section (x, y, z_{middle}) after heating for 20 min

Figs. 2.15-2.16 depict the temperature along the thickness of the domain and its evolution in time. It can be observed that at central location, heating has been more effective for the glass part than for the carbon part. In terms of through-thickness heating, the carbon part shows a temperature gradient of 2°C whereas the glass part shows a gradient of less than 1°C .

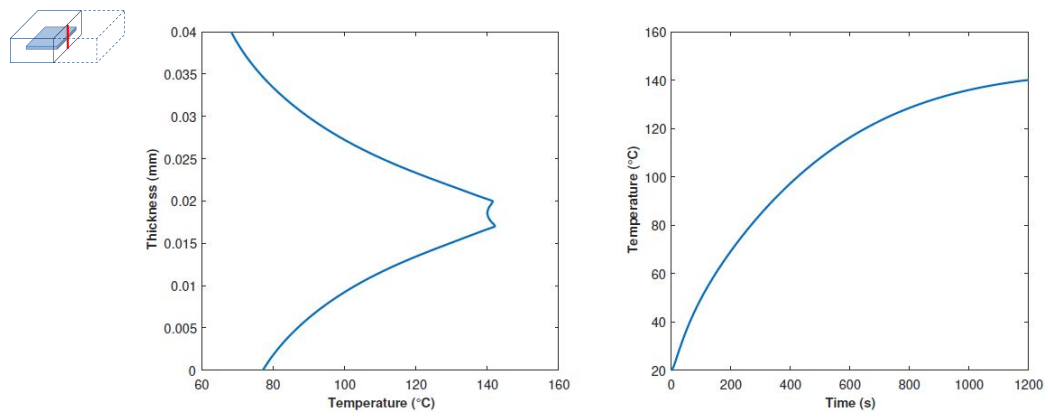


FIGURE 2.15: Carbon case - temperature field along the thickness $(x_{middle}, y_{middle}, z)$ (left) after heating for 20 min and temperature evolution along time at central location $(x_{middle}, y_{middle}, z_{middle})$ (right)

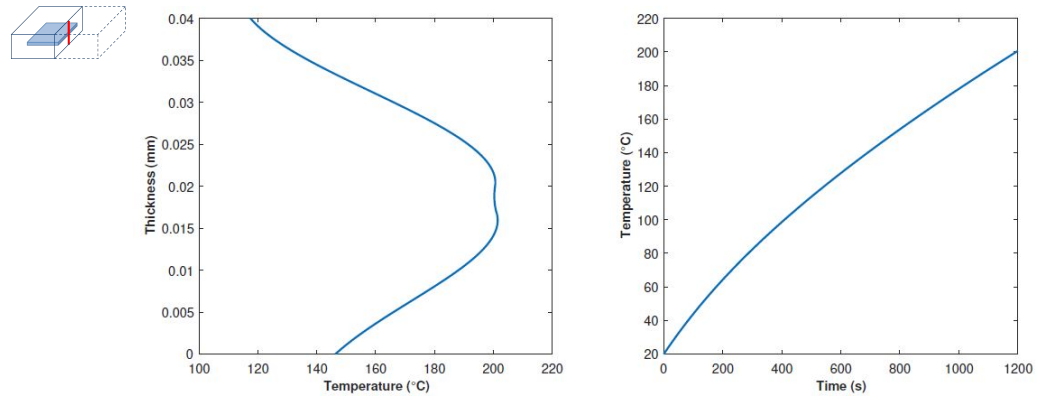


FIGURE 2.16: Glass case - temperature field along the thickness ($x_{middle}, y_{middle}, z$) after heating for 20 min (left) and temperature evolution along time at central location ($x_{middle}, y_{middle}, z_{middle}$) (right)

2.4.2 Influence of the plies orientation

In the case of processing a carbon composite plate, the stacking sequence is one of the important element. Electric field and temperature distribution will be influenced by the anisotropic aspect of the part. In this section, two simple configurations are studied: the stacking in the first case is $[(0^\circ/90^\circ)_5 0^\circ (90^\circ/0^\circ)_5]$ and in the second case, it is $[(90^\circ/0^\circ)_5 90^\circ (0^\circ/90^\circ)_5]$. The important difference between the two configurations lies on the orientation of the external plies, 0° in the first case (later referred as the 0° case) and 90° in the second case (later referred as the 90° case).

Figs. 2.17-2.18 depict the evolution of the electric field along the y direction. No major differences are noticeable in that case: the electric field is almost zero in the composite whereas it propagates in the mold.

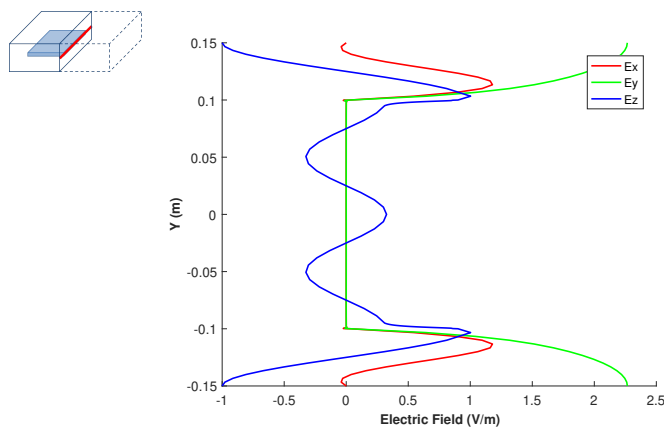


FIGURE 2.17: 0° case - electric field along ($x_{middle}, y, z_{middle}$)

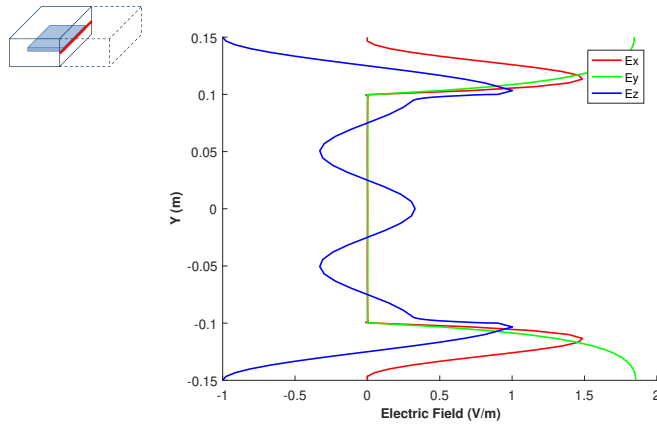


FIGURE 2.18: 90° case - electric field along $(x_{middle}, y, z_{middle})$

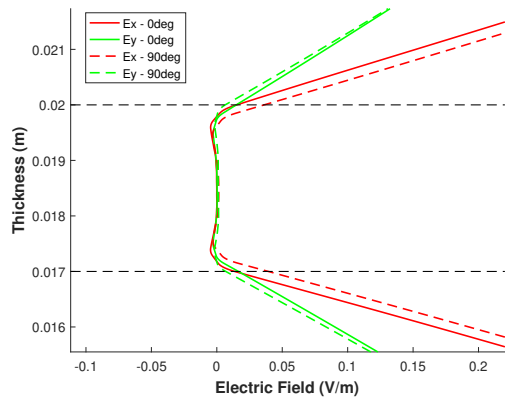


FIGURE 2.19: Comparison of 0° and 90° cases - electric field along the thickness zoomed at composite interfaces $(x_{middle}, y_{middle}, z_{composite})$

Fig. 2.19 highlights the evolution of the E_x and E_y components of the electric field along the thickness zoomed at the composite location. It can be observed that E_x propagates further in the thickness of the composite part in the 90° case whereas E_y propagates further in the thickness of the composite part in the 0° case. In this case, the observation can be explained by the fact that the external layer is 0° oriented, therefore E_x attenuates according to $\sigma_{\parallel} = 4170 \text{ S/m}$ and E_y attenuates according to $\sigma_{\perp} = 6 \text{ S/m}$. Therefore, E_x is more attenuated and E_y propagates further. The same reasoning can be held for the 90° case and leads to the opposite conclusions.

The temperature evolution along the thickness is presented in Fig. 2.20. It appears that heating is more effective in the 90° case than in the 0° case. Indeed, the intensity of E_x component of the electric field is higher than the intensity of E_y . As E_x propagates further in the 90° case, heat sources are

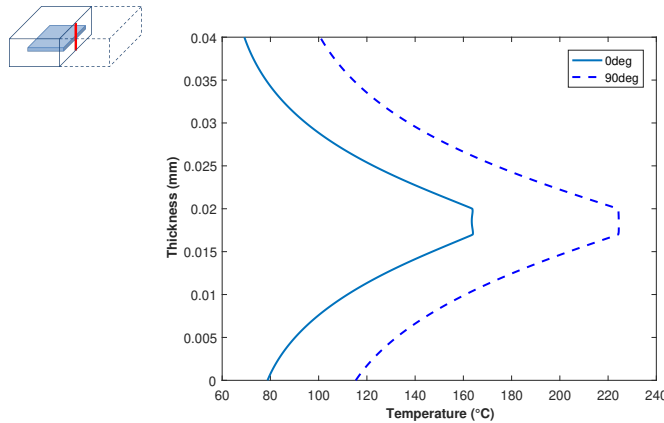


FIGURE 2.20: Comparison of 0° and 90° cases - temperature field along the thickness ($x_{middle}, y_{middle}, z$) after heating for 20 min

more important and leads to higher temperature in the part.

2.4.3 Mold design to ensure uniform heating

In the case of the glass fiber composite plate, it has been observed in Section 2.4.1 that one major issue in processing such material is the strong heterogeneity of the heating, leading to hot spots and bad quality parts. This section investigates the mold design in order to restrain the non-uniform heating. The solution proposed is the insertion of a thin conductive layer at the interface between the mold and the composite part. The aim of such layer is to absorb a part of the incoming electric field. The heat sources produced are then quickly diffused thanks to the high thermal conductivity of the conductive layer. In order to study its effects, three cases are treated: heating of the glass fiber composite without a conductive layer (later referred as non-conductive case), with a conductive layer $500\mu m$ thick (later referred as $500\mu m$ case) and a conductive layer $1mm$ thick (later referred as $1mm$ case).

Figs. 2.21-2.23 depicts the evolution of the three components of the electric field. In the two cases with a conductive layer, a strong attenuation of the electric field is shown in the composite domain.

Figs. 2.24-2.25 present the electric field along the thickness around the composite part. Comparing the two results, the effect of a highly conductive layer is revealed: in the $1mm$ case, the electric field is fully absorbed before propagating in the composite part whereas in the $500\mu m$ case, the electric field is strongly attenuated but not zero.

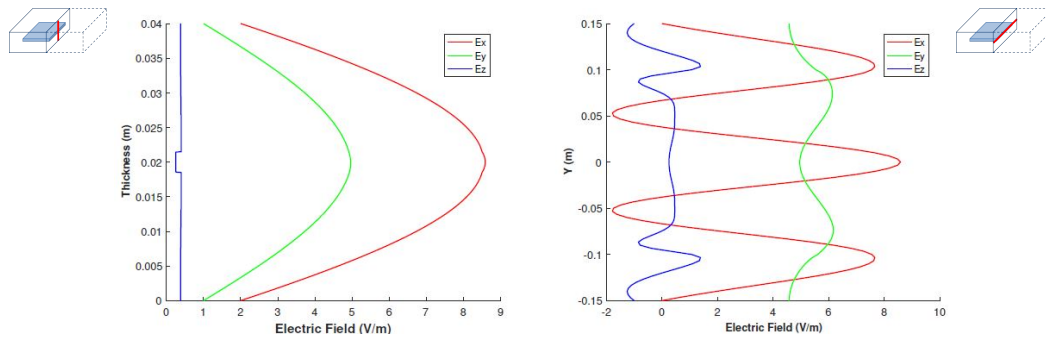


FIGURE 2.21: No-conductive case - electric field along the thickness $(x_{middle}, y_{middle}, z)$ (left) and along $(x_{middle}, y, z_{middle})$ (right)

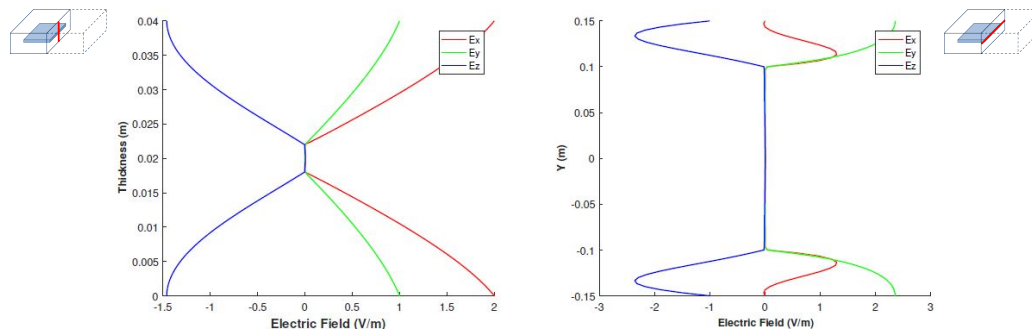


FIGURE 2.22: $500\mu m$ case - electric field along the thickness $(x_{middle}, y_{middle}, z)$ (left) and along $(x_{middle}, y, z_{middle})$ (right)

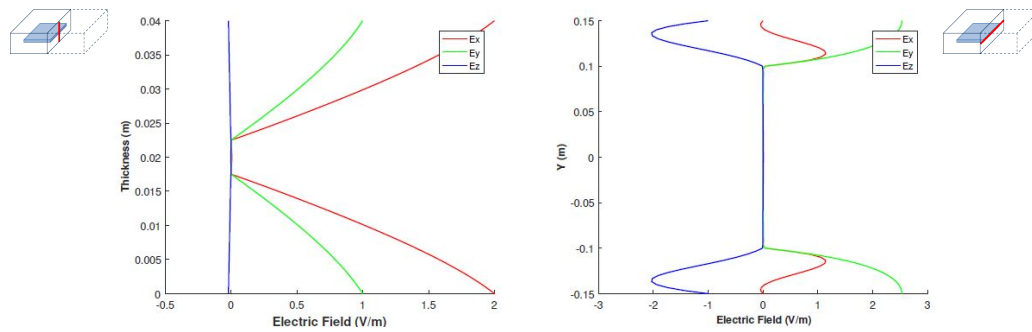


FIGURE 2.23: $1mm$ case - electric field along the thickness $(x_{middle}, y_{middle}, z)$ (left) and along $(x_{middle}, y, z_{middle})$ (right)

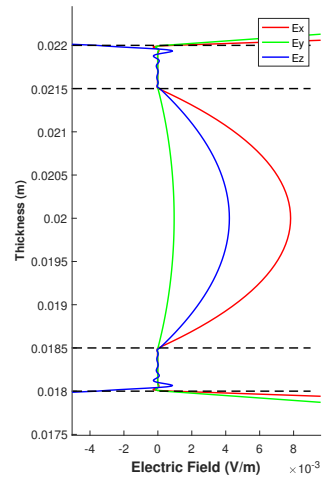


FIGURE 2.24: $500\mu m$ case - electric field along the thicknesses zoomed at the composite interface

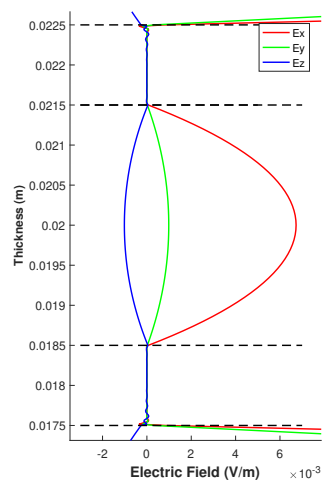


FIGURE 2.25: $1mm$ case - electric field along the thicknesses zoomed at the composite domain interface

The temperature and losses distribution along the thickness at central location in the three different cases are shown in Figs. 2.26-2.28. For an equivalent power delivered, the temperature reached is higher but as recalled from Section 2.4.1, this is due to a very heterogeneous heating. For the cases with a conductive layer, the losses converted in heat sources are located in the conductive layer and are more important in the $500\mu\text{m}$ case - as the electric field is not fully absorbed. This leads to a higher temperature in this case compared to the 1mm case.

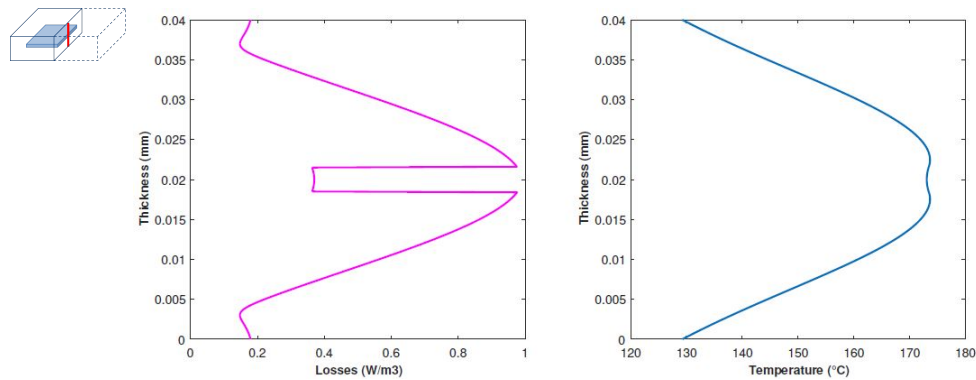


FIGURE 2.26: No-conductive case - losses (left) and temperature field (right) along the thickness after heating for 20 min

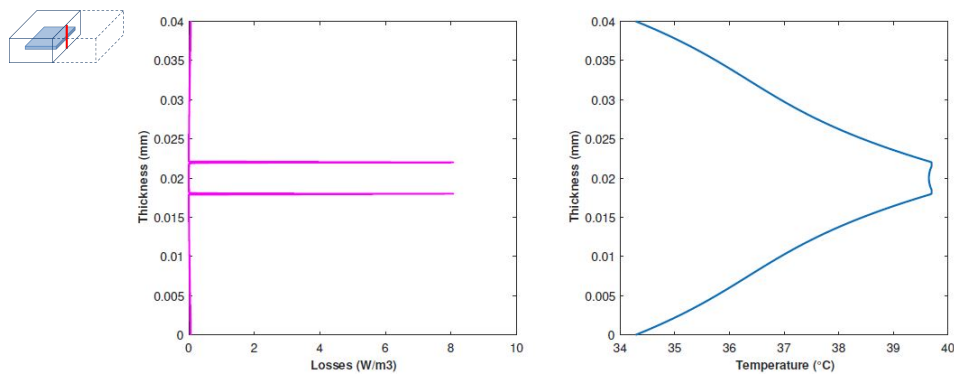


FIGURE 2.27: $500\mu\text{m}$ case - losses (left) and temperature field (right) along the thickness after heating for 20 min

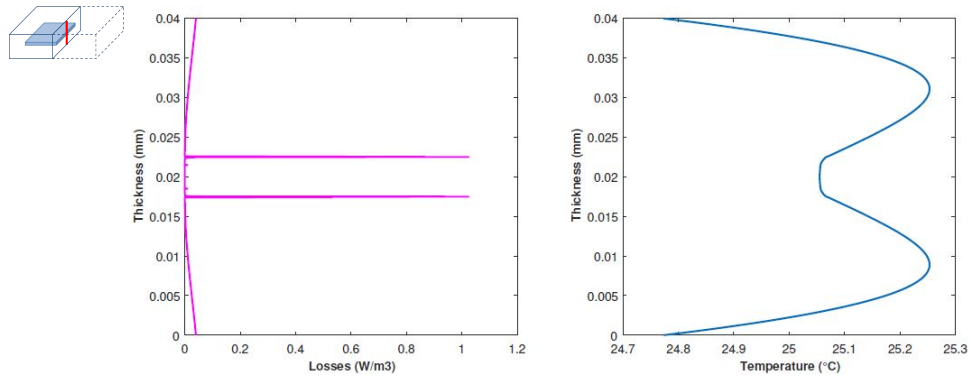


FIGURE 2.28: 1mm case - losses (left) and temperature field (right) along the thickness after heating for 20 min

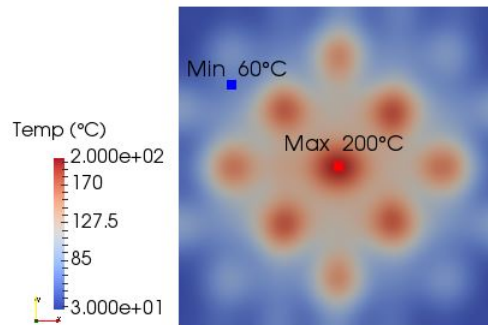


FIGURE 2.29: No-conductive case - temperature distribution in the middle section after heating for 20 min

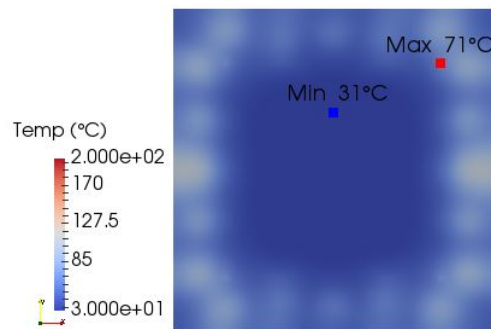


FIGURE 2.30: 500 μ m case - temperature distribution in the middle section after heating for 20 min

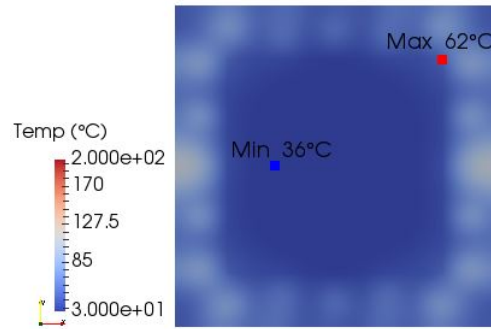


FIGURE 2.31: 1mm case - temperature distribution in the middle section after heating for 20 min

Figs. 2.29-2.31 depict the temperature field in the middle section of the domain. As expected from the previous observations, the temperature reached in the two cases with a conductive layer is less important. Nevertheless, the aim for a more uniform heating is reached.

2.4.4 Uncertainty on the dielectric properties

As mentioned in Section 2.2.1, dielectric properties of composite materials are still one major issue when it comes to the simulation of processing such part at microwave frequency. In order to address the issue of uncertainty of the properties, this section focuses on the impact of variation of the electrical conductivity σ of the composite part considered. The dielectric permittivity of the composite material considered is $\epsilon_r = 4.5$ and $\sigma = 9S/m$. Five test cases are launched with different values of σ : the first one with original value, the next two with a variation of +5% and -5% and the two last with a variation of +10% and -10%.

Figs. 2.32-2.34 depict the temperature field distribution in the middle section of the part for three of the five case: $\sigma_{original}$ and the $\pm 10\%$ cases. Fig. 2.35 presents the evolution of the hot spots temperature – maximum temperature in the composite part – according to the variation of the electrical conductivity. From all the observation, it appears the location of the hot spots in the part does not depend on the conductivity but the temperature value at these hot spots is strongly linked to σ . For a variation of 10% of its value, the hot spot temperature can vary at least of $100^\circ C$ after heating for 20min. Such result is consistent with the evolution expected by common sense.

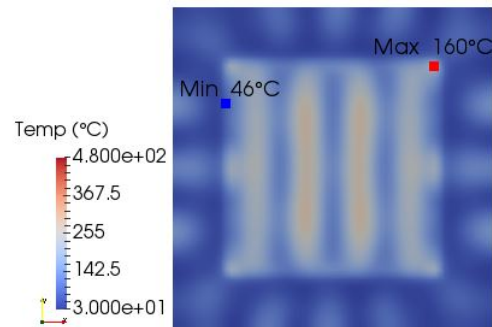


FIGURE 2.32: $\sigma - 10\%$ case - temperature distribution in the middle section after heating for 10 min

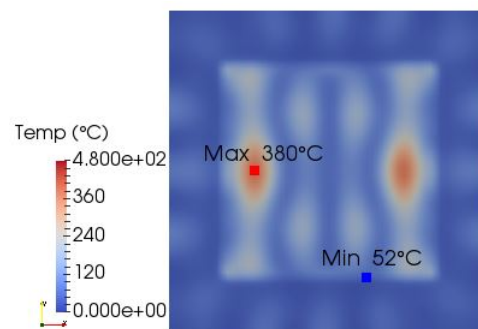


FIGURE 2.33: $\sigma_{original}$ case - temperature distribution in the middle section after heating for 10 min

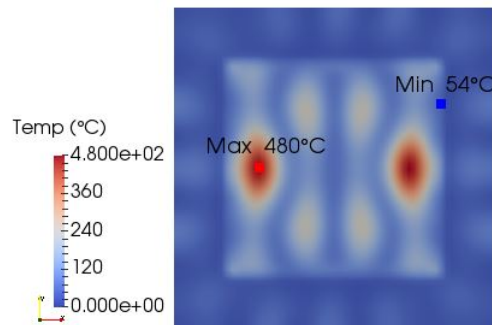


FIGURE 2.34: $\sigma + 10\%$ case - temperature distribution in the middle section after heating for 10 min

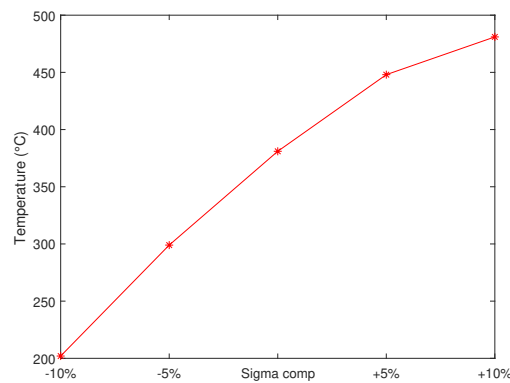


FIGURE 2.35: Temperature evolution of the hot spots in the part according to the value of the electrical conductivity σ

The wide variation range of temperature within a variation of 10% of σ stresses again the need for properties measurements for composite material and their evolution according to temperature in order to have quantitatively reliable results. In the thesis with the assumption of dielectric properties constant with temperature, results can be qualitatively interpreted and compared to each other. Quantitative interpretations are not relevant.

2.4.5 Placement of the tool in the oven cavity

When processing the composite part in a real oven, the electric field distribution in the cavity has a great importance. Furthermore, this electric field strongly depends not only on the cavity but on the disposition of whatever component inside and its location. In order to investigate the influence of the manipulation of the mold by the technician handling the experimental test, three cases are treated. Using Comsol Multiphysics to get the boundary conditions of the electromagnetic problem (see Section 2.3), the mold and part are placed in three different locations in the oven. In the first case, the part is centered, in the second case, the part is positioned with an offset of 3 cm in the x direction (later referred as the offset- x case) and in the third case the offset is set to 3 cm in the x direction and 3 cm in the y direction (later referred as the offset- xy case).

Figs. 2.36-2.38 depict the norm of the electric field on the top surface of the mold. The wide difference observed in the patterns of the electric field on this surface highlights the great dependency of the electric field on the position

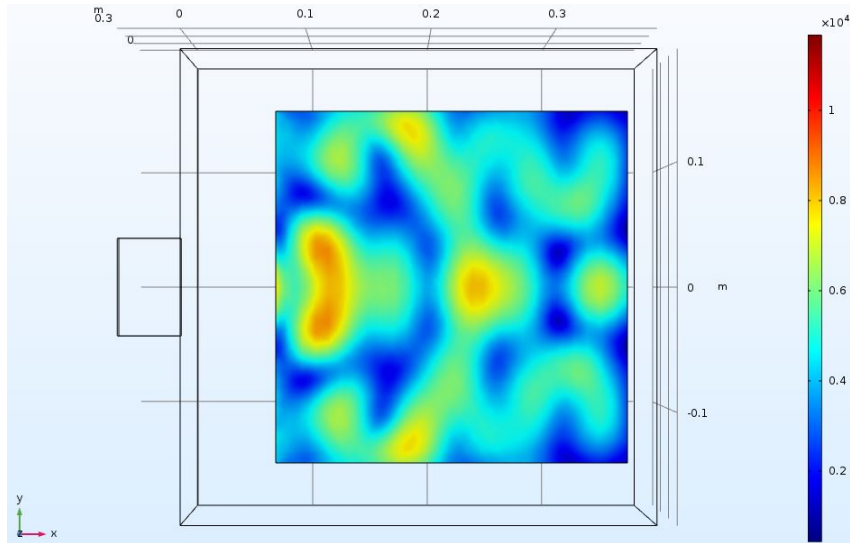


FIGURE 2.37: Offset-x case - distribution of the electric field norm on the top surface of the mold

of the mold and part in the oven cavity – consistent with what is expected from common sense.

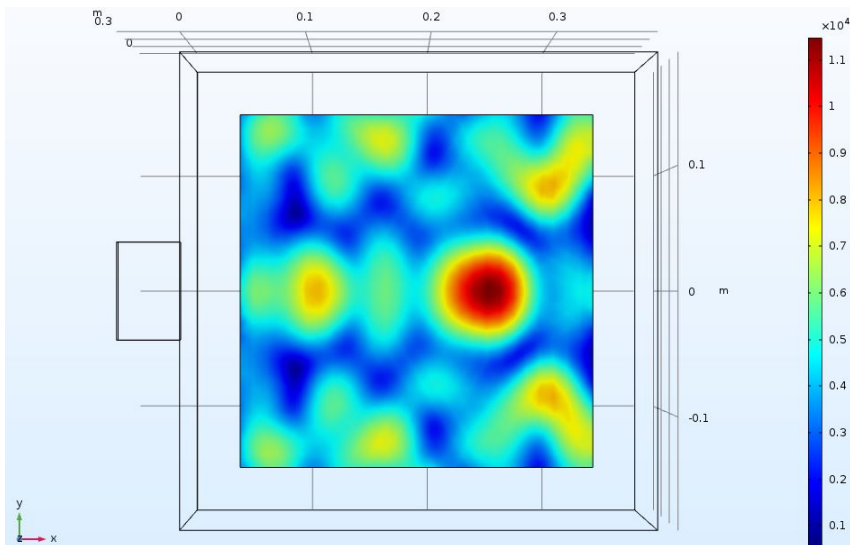


FIGURE 2.36: Centered case - distribution of the electric field norm on the top surface of the mold

The temperature distributions for the three different cases are presented in Figs. 2.39-2.41. From the results, we can observe that the location and the temperature at the hot spots depend on the placement of the part to be processed in the oven. According to where the part is located, it can lead to a

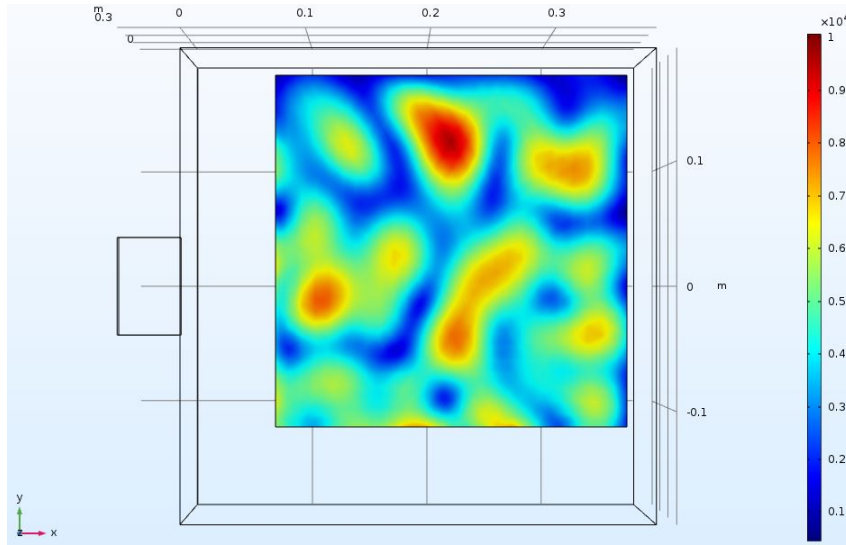


FIGURE 2.38: Offset-xy case - distribution of the electric field norm on the top surface of the mold

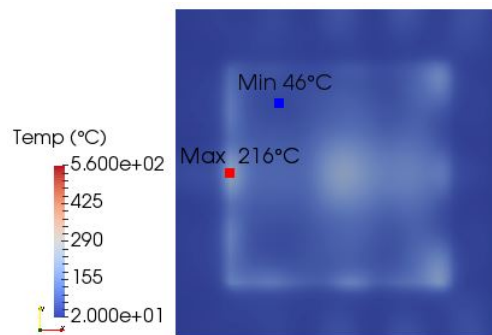


FIGURE 2.39: Centered case - temperature distribution in the middle section of the domain after heating for 45 min

good heating with minimal hot spots as in the centered case or to localized very hot spots as in the offset-x case.

2.5 Discussions and conclusions

In this chapter, the coupling between the electromagnetic solver described in Chapter 1 and the resolution of the heat equation has been presented. The coupling used today is a weak coupling, meaning that the evolution of the dielectric properties with temperature is not taken into account. One full simulation from electromagnetics to calculating the heat sources and solving the heat equation takes approximately 10min in a basic laptop for the typical numerical results presented (a mesh of 10000 Q1 elements \times 200 1D elements).

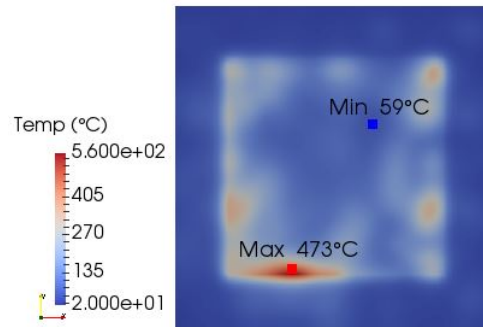


FIGURE 2.40: Offset-x case - temperature distribution in the middle section of the domain after heating for 45 min

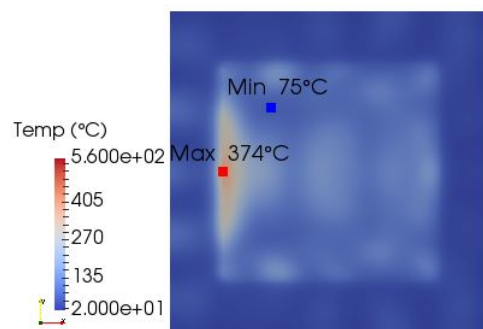


FIGURE 2.41: Offset-xy case - temperature distribution in the middle section of the domain after heating for 45 min

Using the in-plane-out-of-plane representation within the PGD framework allows a very refine discretisation in the thickness direction, which is absolutely necessary in order to capture the heat sources created by the presence of a thin conductive layer for example.

Thanks to the five studies presented, recommandations can be issued in order to use the microwave heating process at its best. The choice of material to be processed is crucial as it can lead to a very heterogeneous heating or a need for more power to be delivered. When using an anisotropic fabric, the user has to be careful to stacking sequence as it will impact the time needed to reach the desired temperature. Homogeneous heating can be enforced using an appropriate design of mold. The handling of the part when placed in the oven cavity has to be precise to ensure a good match between the expected simulated results and the experimental work as small displacement can dramatically change location and temperature of the hot spots. As a consequence, the optimisation of the microwave heating process for composite materials relies on three different aspects:

- Material choice: type of fibers, stacking sequence and optimisation of the resin (for example, addition of fillers to make the resin more thermally conductive to minimize the hot spots) are key parameters.
- Process design: the tools used in the process have to be cleverly designed and optimised - one solution being the addition of a thin conductive layer to ensure heating uniformity.
- Data precision: electromagnetics are easily perturbed by change in geometry or material properties - one has to be as precise as possible when dealing with the process experimentaly or through simulations.

To go forward on this work and understand more precisely and accurately the microwave heating of composite materials, perspectives includes developing the strong coupling between electromagnetic and thermal solvers – which requires to previously measure the dielectric properties of composite materials and their evolution with temperature. A second axis of future developments is the extension of the variability study using a parametric solution.

Chapter 3

Real-time Simulation for Direct Control during Microwave Heating

Contents

3.1 Introduction	59
3.1.1 A need for real-time control of process	60
3.1.2 Taking into account kinetic sources	61
3.2 Reduction of the heat equation with thermo-kinetic and electromagnetic sources	61
3.3 Experimental measurements for reduction model validation	64
3.3.1 Microwave oven device	65
3.3.2 Samples used	66
3.3.3 Temperature measurements	68
3.4 Experimental and simulation comparison	69
3.4.1 Sample 1: no kinetic heat sources	69
3.4.2 Sample 2: exothermic epoxy curing	74
3.5 Discussions and conclusions	78

3.1 Introduction

In this chapter, two new issues are tackled in order to extend the answers we can provide to the ever challenging development of processing a composite material part.

3.1.1 A need for real-time control of process

As mentioned in the general introduction to this work, eventhough the composite material has been a trending topic for the last decades, the strong competition with other materials push forward new innovations. In order to generalize the use of composite materials as part of a manufacturing process, new processing methods have to be developed - that is why this research is focusing on the innovative processing of composite materials using microwaves. The previous chapter aimed at the understanding of the phenomena occuring during the process for a better understanding of the heating pattern. In parallele to such developments, industrial implementation focuses more on the real-time control of the process during the heating phase to ensure part quality.

Looking at the real-time control of a microwave heating process, one parameter that can be adjusted during the production of a part is the power delivered by the oven. At each chosen time-step, according to the behaviour of the part, the user should be able to adjust the power to avoid overheating, underheating or creation of hot-spots. On a practical point of view, realising such adjustment might be difficult as control over the power delivered by a magnetron is limited. This issue is –for now– circumvented by on-off switch of magnetron to deliver a specific amount of power during a certain time.

In terms of simulation, the constraint of real-time control implies that given the actual temperature in the oven, the simulation tool should be able to anticipate the adjustment needed to the power delivered to the system in order to follow the temperature cycle desired. Such use of co-simulation of process during production to assess compliance of actual process to expected process is essential. In that perspective, the PGD approach is not possible anymore. Where the decomposition according to the time coordinate was an advantage in the previous chapter (as detailed in Section 2.2.2), it is now a limitation as it is necessary to have an incremental simulation. In addition to an iterative approach, simulation needs to be performed in real-time for time-steps as small as one second. In order to achieve such performance, one solution using Model Order Redution (MOR) is proposed in this chapter.

3.1.2 Taking into account kinetic sources

Looking at actual composite parts which could be manufactured by microwave heating, reactive resins are most likely to be used. Therefore, taking into account electromagnetic heat sources as previously depicted is not sufficient anymore. When resins are exposed to heat, exothermic chemical reaction is induced and participate to the curing of the resin. This complex physico-chemical phenomenon is governed by polymerisation reactions and numerous models have been built depending on the resin characteristics [67, 88, 72, 43, 78, 73]. Generalised forms for the modeling of such reaction is given by:

$$\frac{\partial \alpha}{\partial t} = f(\alpha, T), \quad (3.1)$$

where α is the degree of cure of the resin and T the temperature. The source term $Q_{kin}(x, y, z, t)$ intervening in the heat equation is proportionnal to the derivative of α according to time:

$$Q_{kin}(x, y, z, t) = \Delta H(1 - V_f)\rho_r \int_0^t \frac{\partial \alpha}{\partial t} d\zeta, \quad (3.2)$$

where ΔH is the enthalpy of reaction, V_f is the fiber content of the composite part and ρ_r is the density of the resin.

Such formulation is then non-linear and again needs for an iterative simulation to be solved. As a consequence, such contribution can easily be added in the new solution developed by MOR techniques. The use of MOR for the reduction of thermal models coupling thermo-kinetics and electromagnetic sources is original. No previous work has been found coupling such physics and using reduction techniques for control. In addition, the poorly known behaviour of resins under microwave leads to a necessary refined control during the process. Unexpected reactions and sudden temperature change can be addressed despite few modeling information on thermokinetics under electromagnetic fields.

3.2 Reduction of the heat equation with thermo-kinetic and electromagnetic sources

This section develops the MOR for the heat equation when considering thermokinetic and electromagnetic heat sources under the constraint of a tunable power delivered by the magnetron in the oven cavity at each time step.

The electromagnetic problem being linear regarding the electromagnetic power, we denote by $\Theta(x, y, z)$ the electromagnetic source field in the simulation domain Ω when a unit power source applies at the magnetron. Thus, the total electromagnetic power results $\mathcal{P}\Theta(x, y, z)$, with \mathcal{P} the magnetrons power.

The heat equation allows computing the temperature at each point $(x, y, z) = \mathbf{x} \in \Omega$ and time t , $T(\mathbf{x}, t)$, with $T(\mathbf{x}, t = 0)$ assumed known and by enforcing appropriate boundary conditions on the domain boundary $\partial\Omega$. It writes

$$\rho C_p \frac{\partial T}{\partial t} = \nabla (\lambda \cdot \nabla T) + \mathcal{P}\Theta(\mathbf{x}) + \mathcal{S}(\mathbf{x}, t), \quad (3.3)$$

where for the sake of simplicity thermal dependences on the different parameters (ρ , C_p and the thermal conductivity λ) are neglected. In the previous equation \mathcal{S} refers to the source term related to the kinetic coupling (curing, phase transformation, etc ...) that in general is given by a nonlinear function on the temperature and the degree of advancement of the kinetic reaction. This kinetic term is nonlinear but its remains local in space.

After discretizing the previous equation using an appropriate numerical technique (e.g. finite elements, finite differences, ...) it results

$$\mathbf{M} \frac{\mathbf{T}^{n+1} - \mathbf{T}^n}{\Delta t} = \mathbf{K} \mathbf{T}^{\alpha(n+1) + (1-\alpha)n} + \mathcal{P}^{n+1} \Theta + \mathbf{S}^n, \quad (3.4)$$

where \mathbf{M} is the traditional mass matrix, \mathbf{K} the stiffness matrix and with $0 \leq \alpha \leq 1$, leading to an explicit strategy when choosing $\alpha = 1$ or implicit in the case of considering $\alpha = 0$. \mathbf{M} and \mathbf{K} depends on the numerical technique chosen.

When solving online the thermal problem with very small time steps (fine control strategy), the explicit method seems more appropriate, and could fulfill real-time constraints. However, when calculating a parametric solution, as it is the case in what follows, an implicit discretization seems more appropriate because of its superior stability behavior. Thus, in what follows we consider $\alpha = 1$ that leads to:

$$(\mathbf{M} - \Delta t \mathbf{K}) \mathbf{T}^{n+1} = \Delta t \mathcal{P}^{n+1} \Theta + \Delta t \mathbf{S}^n + \mathbf{M} \mathbf{T}^n. \quad (3.5)$$

Now, many snapshots of the temperature field \mathbf{T} and the kinetic source term \mathbf{S} are collected and a SVD –Singular Value Decomposition– is performed, from which the respective reduced basis could be extracted, consisting of the

eigenvectors associated with the higher eigenvalues. The N higher eigenvalues are chosen such as $|\alpha_N - \alpha_1| < \epsilon$ where α_1 is the higher eigenvalue and ϵ the tolerance chosen (here $\epsilon = 10^{-8}$). Thus, both reduced bases are composed of vectors $\boldsymbol{\phi}_l$ and $\boldsymbol{\psi}_m$ respectively, with $l = 1, \dots, \mathcal{L}$ and $m = 1, \dots, \mathcal{M}$, with both \mathcal{L} and \mathcal{M} much smaller than the number of nodes N_n used in the space discretization.

Thus, we can perform approximations at any time t_n according to

$$\mathbf{U}^n \approx \sum_{l=1}^{\mathcal{L}} \beta_l^n \boldsymbol{\phi}_l, \quad (3.6)$$

and

$$\mathbf{S}^n \approx \sum_{m=1}^{\mathcal{M}} \gamma_m^n \boldsymbol{\psi}_m. \quad (3.7)$$

By defining $\boldsymbol{\Phi}$ the matrix whose columns are $\boldsymbol{\phi}_m$ and $\boldsymbol{\Psi}$ the one composed by vectors $\boldsymbol{\psi}_n$, implying:

$$\begin{cases} \mathbf{U}^n = \boldsymbol{\Phi} \boldsymbol{\beta}^n \\ \mathbf{S}^n = \boldsymbol{\Psi} \boldsymbol{\gamma}^n \end{cases}, \quad (3.8)$$

we can obtain the reduced discrete linear system related to Eq. (3.5)

$$\boldsymbol{\Phi}^T (\mathbf{M} - \Delta t \mathbf{K}) \boldsymbol{\Phi} \boldsymbol{\beta}^{n+1} = \Delta t \mathcal{P}^{n+1} \boldsymbol{\Phi}^T \boldsymbol{\Theta} + \Delta t \boldsymbol{\Phi}^T \boldsymbol{\Psi} \boldsymbol{\gamma}^n + \boldsymbol{\Phi}^T \mathbf{M} \boldsymbol{\Phi} \boldsymbol{\beta}^n, \quad (3.9)$$

where after introducing into Eq. (3.5) expression (3.8), the resulting equation is premultiplied by $\boldsymbol{\Phi}^T$.

The parametric solution for the power delivered by the electromagnetic source consists in writing $\boldsymbol{\beta}^{n+1}$ as a function of \mathcal{P} , of each component of $\boldsymbol{\gamma}^n$ and $\boldsymbol{\beta}^n$. For that purpose, and taking into account the linearity of the previous equation we must solve $1 + \mathcal{L} + \mathcal{M}$ linear systems (related to a single time step):

- We denote by \mathbf{v}_p the solution of Eq. (3.9) for $\mathcal{P}^{n+1} = 1$, $\boldsymbol{\beta}^n = \mathbf{0}$ and $\boldsymbol{\gamma}^n = \mathbf{0}$;
- Then vectors \mathbf{v}_l^β , for $l = 1, \dots, \mathcal{L}$, solutions of Eq. (3.9) for $\mathcal{P}^{n+1} = 0$, $\boldsymbol{\gamma}^n = \mathbf{0}$, $\beta_k^n = \delta_{l,k}$ (with δ the Kroenecker delta);
- Finally vector \mathbf{v}_m^γ , for $m = 1, \dots, \mathcal{M}$, solutions of Eq. (3.9) for $\mathcal{P}^{n+1} = 0$, $\boldsymbol{\beta}^n = \mathbf{0}$, $\gamma_k^n = \delta_{m,k}$.

Now, as soon as the solution at the previous time step is known, $\boldsymbol{\beta}^n$, as well as the kinetic sources $\boldsymbol{\gamma}^n$ and the present electromagnetic power applied at

the magnetrons \mathcal{P}^{n+1} , the solution reads

$$\boldsymbol{\beta}^{n+1} = \mathcal{P}^{n+1} \mathbf{v}_p + \sum_{l=1}^{\mathcal{L}} \beta_l^n \mathbf{v}_l^\beta + \sum_{m=1}^{\mathcal{M}} \gamma_m^n \mathbf{v}_m^\gamma. \quad (3.10)$$

Eq. (3.10) can be efficiently applied, with the only issue related to the determination of γ^n . For that purpose, as soon as $\boldsymbol{\beta}^n$ is assumed known (computed at the previous time step), the full temperature field is reconstructed from $\mathbf{T}^n = \boldsymbol{\Phi} \boldsymbol{\beta}^n$, then from nodal temperatures one can evaluate the kinetic term \mathbf{S}^n , and then project it into the reduced basis to obtain $\gamma^n = \boldsymbol{\Psi}^T \mathbf{S}^n$.

Such calculation for the solution at each time step is fast (tens of nanoseconds) and \mathcal{P}^{n+1} can be adjusted by the control algorithm in order to fit the required heat treatment.

To conclude on the development of the modeling of temperature evolution using MOR coupling electromagnetics and thermo-kinetics, the developed tool allows instant resolution of the temperature field using Eq. 3.10 for two configurations. On a first case, the power applied at the magnetron is known and solving Eq. 3.10 amounts to solve the heat equation in the part taking into account all heat sources occurring in the composite part. On a second case where the user needs to control the power delivered by the oven to follow a specific requirement, the instantaneous resolution of Eq. 3.10 enables to choose the adapted power –using an optimisation algorithm matching the temperature wanted at the specific time with the temperature simulated by tuning the power value.

3.3 Experimental measurements for reduction model validation

In order to investigate the capabilities of the model reduction proposed on the heat equation, experimental work is done for two different samples of carbon fiber preform.

The following experiments have been realised in the framework of the SIMU-TOOL project with the partnership of TWI, Loiretech, Faurecia and Airbus Group Innovation.

3.3.1 Microwave oven device

The microwave oven device used for the heating process of the composite part is a hexagonal-shaped Hephaistos VHM 100/100 produced by Weiss Technik (Fig. 3.1). The microwave power is supplied by the twelve magnetrons placed around the oven with two magnetrons on each side of the hexagone. Each magnetron delivers an electromagnetic field at a 2.45GHz frequency and up to 850W, total power of the oven then being 10.2kW. Dimensions of the cavity are approximately 1m in each direction.

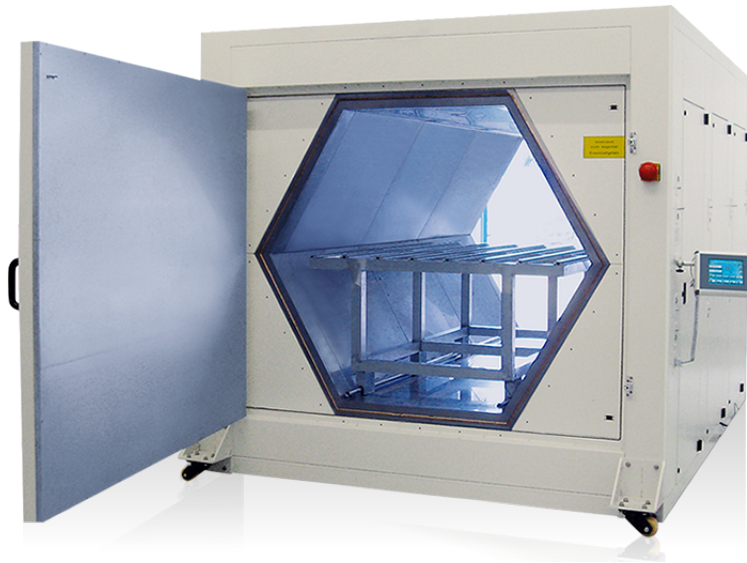


FIGURE 3.1: Hexagonal-shaped Hephaistos microwave oven

The unique hexagonal shape has been designed in order to overcome the field heterogeneity issue in a closed cavity. As shown in Section 2.3.1, the electric field distribution is likely to be strongly heterogeneous in the microwave oven cavity. As claimed by the oven designer, using an hexagonal shape and twelve sources placed around the cavity draws the expectation of the user to have a more homogeneous field distribution in the cavity. To enhance this assumption, simulations of the oven cavity with the supplied metal table are carried using the CEM One software [16] from ESI Group. This software shows more capabilities than Comsol when it comes to large-domain simulations and simulation technique can be adapted to the more suited to the case. Possible methods are the Method of Moments (MoM) [34, 35, 61], the Finite Element Method (FEM) or the Finite Difference Time Difference method (FDTD) [91, 82, 81, 46]. In our case, the FDTD method is chosen due to its smaller amount of memory needed with finer mesh and it

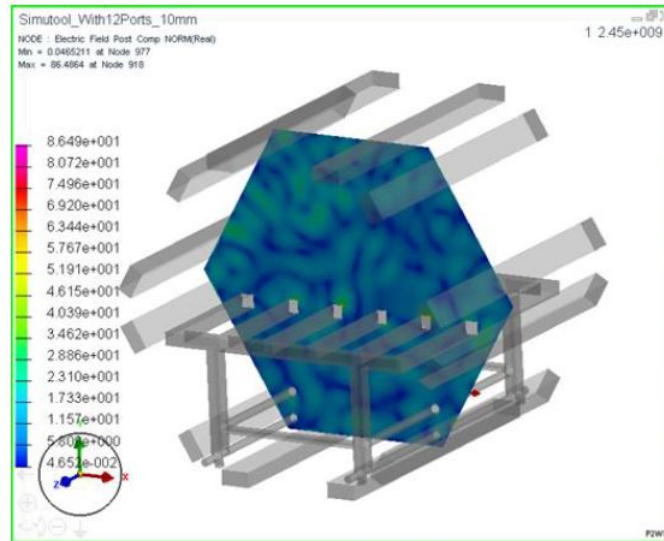


FIGURE 3.2: Electric field amplitude for the empty oven with all waveguides feeding

is the least time-consuming option. Figs.3.2-3.3 depict the electric field amplitude and surface current in the empty oven cavity with the metallic table. Electric field amplitude obtained on the middle cross-section agrees with the homogeneity statement of the field.

3.3.2 Samples used

Two different samples are prepared to be tested in the microwave oven with temperature monitoring. The geometry of the samples is a plate which dimensions are $200\text{mm} \times 200\text{mm} \times 3\text{mm}$ placed in the center of a mold of dimensions $300\text{mm} \times 300\text{mm} \times 40\text{mm}$.

The material used for the samples are preforms made of carbon fibers. The first preform is composed of short carbon fibers randomly distributed with a small proportion of thermoplastic binder to help the fibers to stick together (Fig. 3.5). The second preform is a laminate (Fig. 3.6) with a quasi-isotropic stacking $[45^\circ 90^\circ 135^\circ 0^\circ]$ of unidirectional plies composed of carbon fibers and epoxy resin. The microwave heating purpose for the two samples are different: the projected-fiber sample needs to be pre-heated before forming and the carbon / epoxy sample needs to be cured in the microwave oven. Therefore, the heat treatment required is different in each case and needs to be controlled over time during the process by adjusting the power delivered by the magnetrons. For the projected-fiber sample, the preforming requires

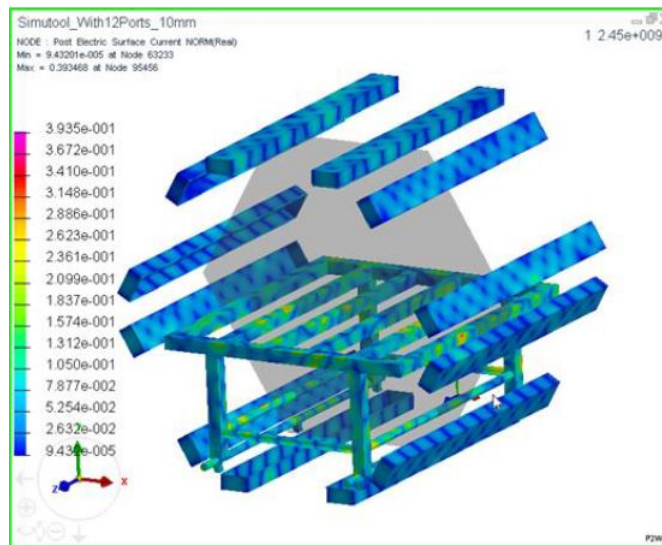


FIGURE 3.3: Surface currents (right) for the empty oven with all waveguides feeding



FIGURE 3.4: Mold design for experimental tests in the microwave oven



FIGURE 3.5: Projected fiber sample prior to heating

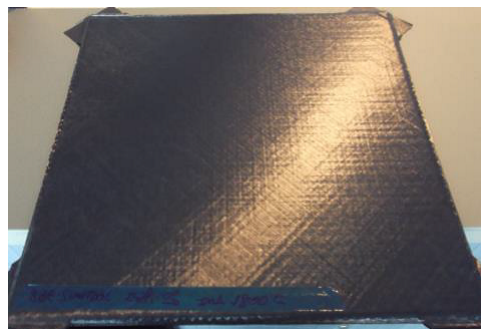


FIGURE 3.6: Carbon / epoxy sample prior to heating

at a temperature of 230°C during one minute in order to melt the thermoplastic binder and ensure the preform to be manipulated. The carbon / epoxy sample needs to follow the cure cycle of the epoxy resin composed of two main phases. First phase is a heating from room temperature to 180°C at a $3^{\circ}\text{C}/\text{min}$ rate and the second phase is a 2-hour dwell at 180°C . As depicted on 3.7, the two cure cycles studied are very different in both duration and precision requirements. For the projected fiber sample, process can be optimized to achieve the heating cycle whereas for the carbon / epoxy sample, the cycle needs to be carefully followed for a full cure of the resin and ensure the quality of the part.

3.3.3 Temperature measurements

Temperature measurements during the trials are carried using six measuring fibre optic thermocouples placed within the tool and preform. Location of the thermocouples are depicted in Figs. 3.8-3.10 for the projected-fiber sample

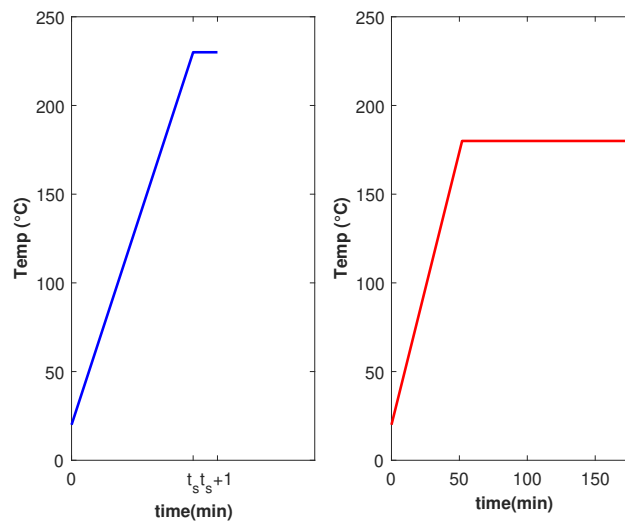


FIGURE 3.7: Heating cycles for projected fiber sample (left) and carbon / epoxy sample (right) where t_s refers to the shortest possible heating time from ambient temperature to 230°C

and in Fig. 3.11-3.13 for the carbon / epoxy sample.

3.4 Experimental and simulation comparison

3.4.1 Sample 1: no kinetic heat sources

The first sample tested is the projected-fiber sample. Simulation of the electric field distribution in the oven cavity is carried using CEM One software which is able to provide the heat sources distribution within the mold and composite part. The heat sources in the part are depicted on Fig. 3.14 in the case where the twelve magnetrons are switched on and delivering a unitary power.

The experimental results for the heating of the composite part in the oven are depicted on Fig. 3.16 using the power evolution of Fig. 3.15. The power evolution is automatically generated by the self-control device of the oven given a specific heat cycle. It is reminded that the requirements for this specific sample is to reach 230°C during one minute.

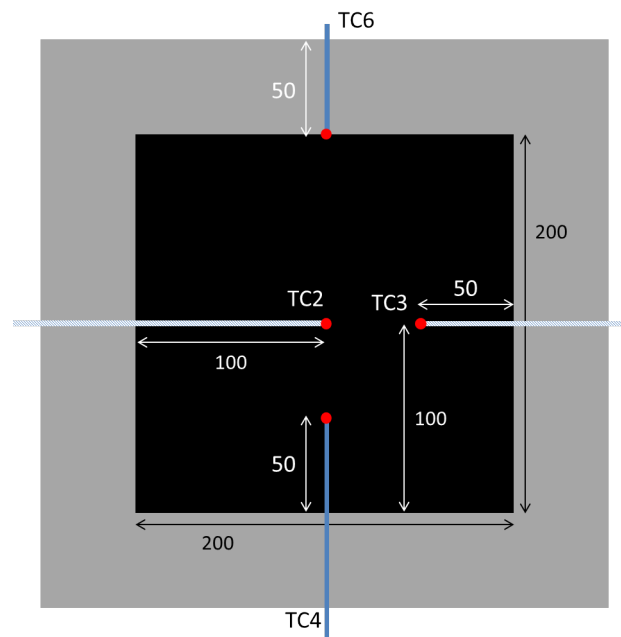


FIGURE 3.8: Thermocouples location in the projected-fiber sample, bottom view of the tool and sample - striped thermocouples represent the thermocouples inserted in the middle of the part

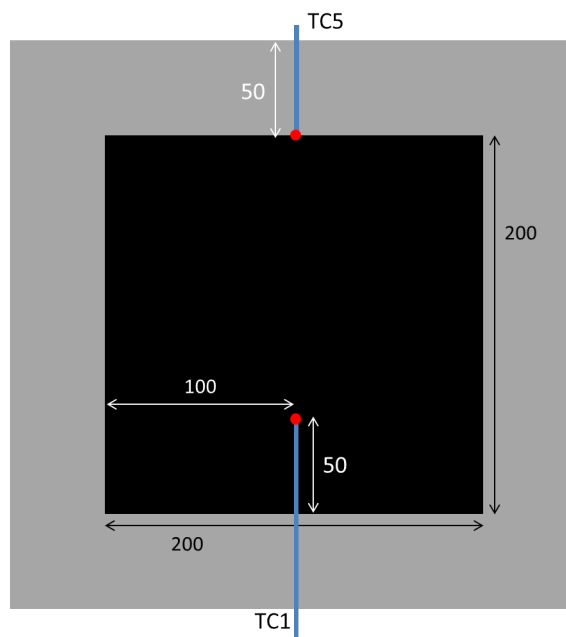


FIGURE 3.9: Thermocouples location in the projected-fiber sample, top view of the tool and sample

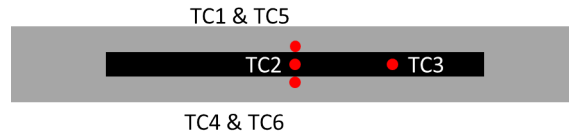


FIGURE 3.10: Thermocouples location in the projected-fiber sample, front view of the tool and sample

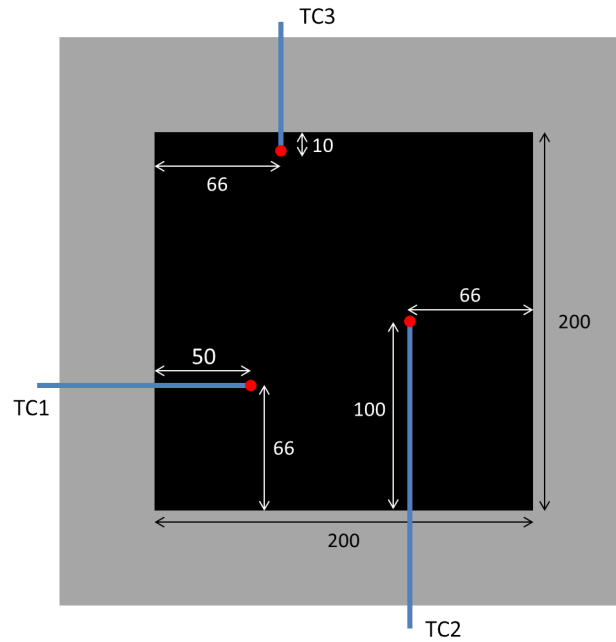


FIGURE 3.11: Thermocouples location in the carbon / epoxy sample, bottom view of the tool and sample

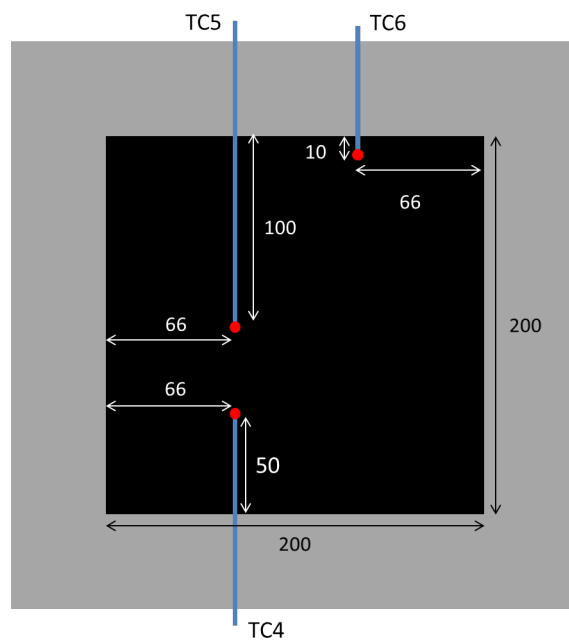


FIGURE 3.12: Thermocouples location in the carbon / epoxy sample, top view of the tool and sample

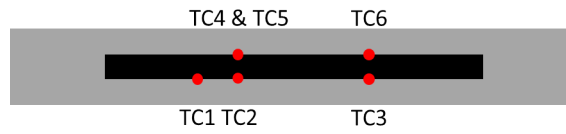


FIGURE 3.13: Thermocouples location in the carbon / epoxy sample, front view of the tool and sample

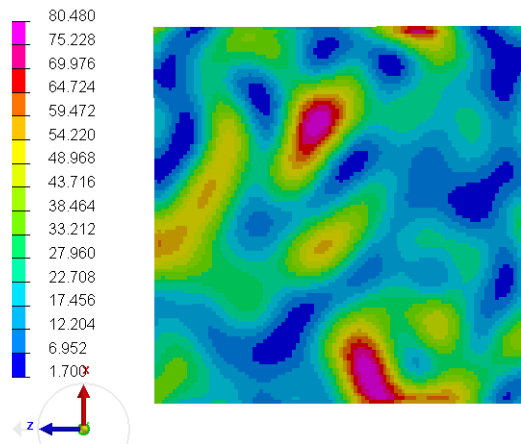


FIGURE 3.14: Heat sources distribution in the composite part for unitary power delivered by the twelve magnetrons for the projected-fiber sample in W/m^3

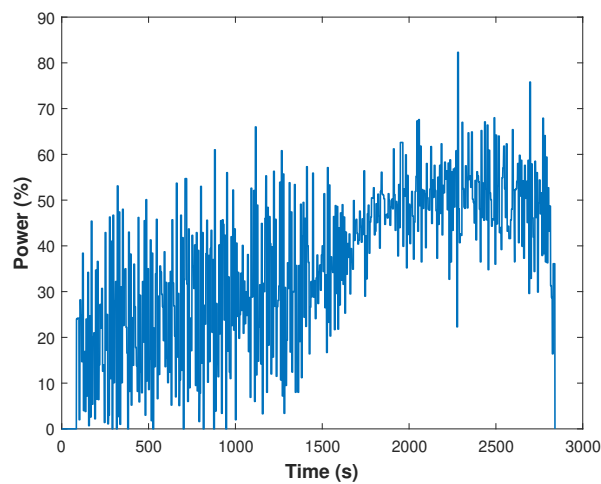


FIGURE 3.15: Power evolution during the projected-fiber sample trial (100% of the power represents a total 10.2 kW delivered by the twelve magnetrons)

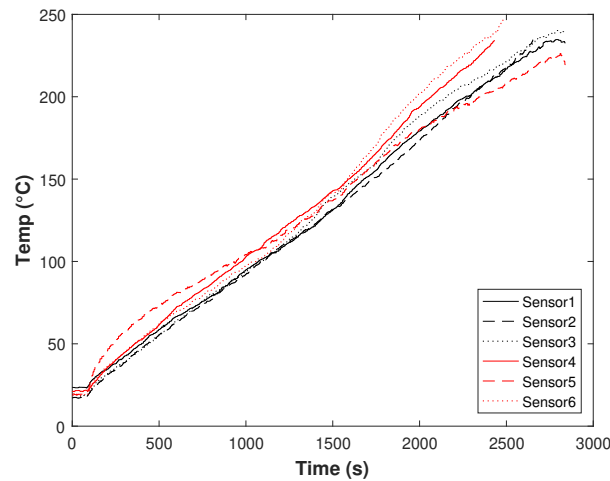


FIGURE 3.16: Measured temperature evolution at the six sensors locations in the projected-fiber sample

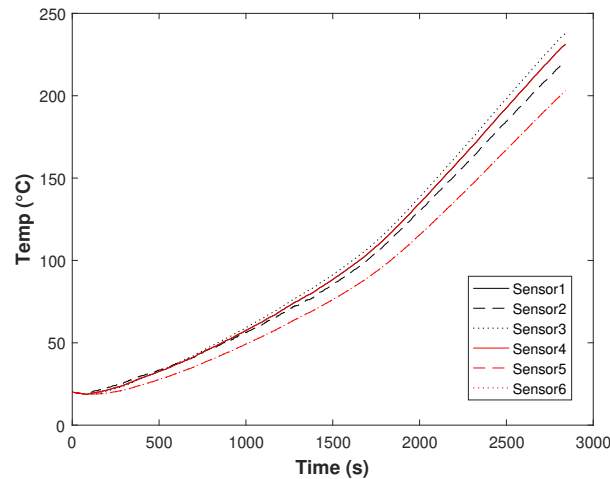


FIGURE 3.17: Temperature evolution at sensors location simulated with the MOR technique for the projected fiber sample

First validation for the MOR algorithm used is to apply the same power evolution as the experimental trial in the numerical resolution. Simulation results are depicted on Figs. 3.17-3.18. The temperature evolution at the sensors locations (Fig. 3.17) is of the same order of magnitude as in the experimental trial. Fig. 3.18 shows the temperature distribution in the middle cross-section of the composite part. The heterogeneity of the heating observed is a consequence of the heterogeneity of the heat sources due to the microwave heating (as shown on Fig. 3.14).

In order to optimise the heating process for the part, MOR algorithm is ran in order to get the fastest heating rate to the required 230°C. The power distribution and temperature evolution at sensors obtained are respectively

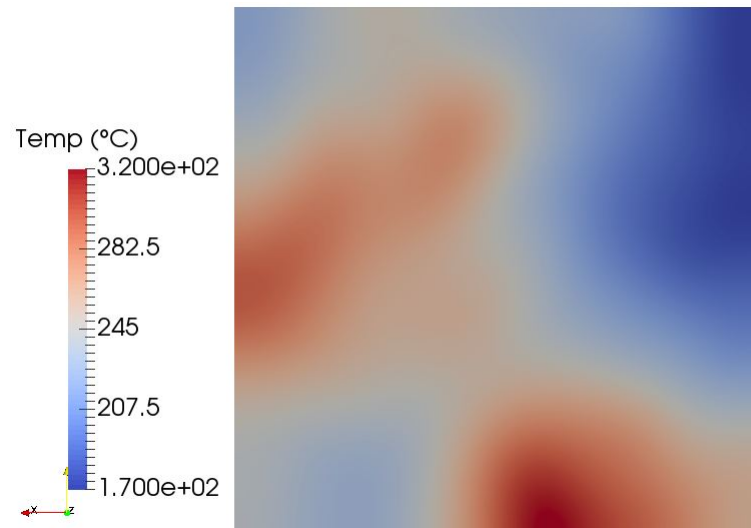


FIGURE 3.18: Temperature distribution at the end of the heating process in the middle cross-section of the composite part for the projected fiber sample

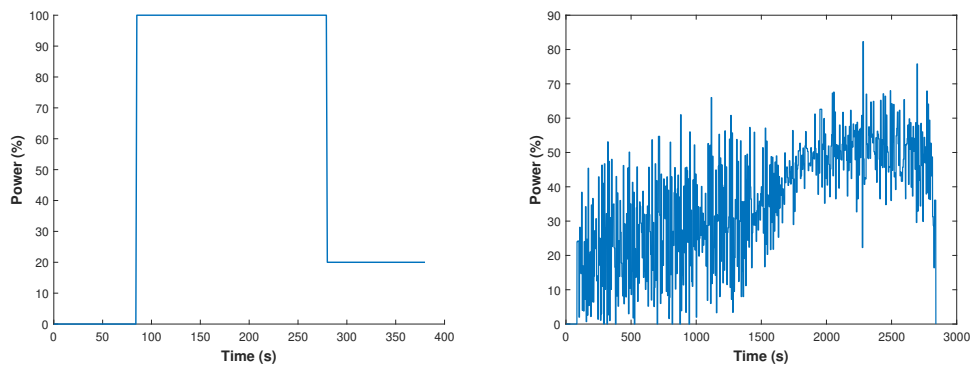


FIGURE 3.19: Power evolutions for the optimised (rleft) and initial (right) heating processes for the projected-fiber sample

depicted on Fig. 3.19 and Fig. 3.20. The optimised process cuts down the duration of the heating of the part to 380 seconds (approximately 6 minutes) as shown on Fig. 3.20.

3.4.2 Sample 2: exothermic epoxy curing

The second sample tested is the carbon / epoxy sample. Simulation of the electric field distribution in the oven cavity is carried using CEM One software which is able to provide the heat sources distribution within the mold and the homogenized composite part (homogenization of properties is carried according to [39]). The heat sources in the part are depicted on Fig. 3.21 in the case where the twelve magnetrons are switched on and delivering a unitary power.

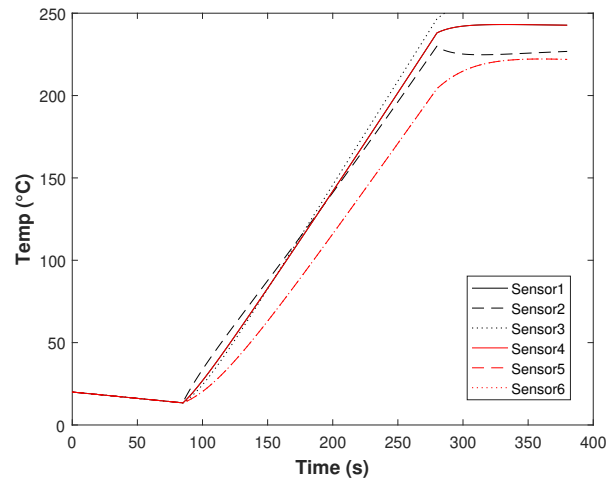


FIGURE 3.20: Temperature evolution at the six sensors locations in the projected-fiber sample for the optimised heating

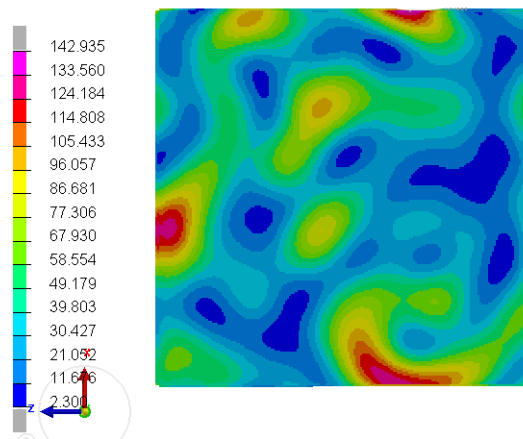


FIGURE 3.21: Heat sources distribution in the composite part for unitary power delivered by the twelve magnetrons for the carbon / epoxy sample in W/m^3

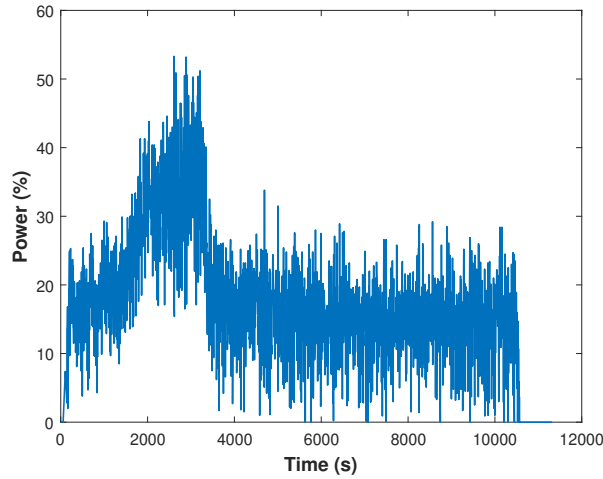


FIGURE 3.22: Power evolution during the carbon / epoxy sample trial (100% of the power represents a total 10.2 kW delivered by the twelve magnetrons)

The experimental results for the heating of the composite part in the oven are depicted on Fig. 3.23 using the power evolution of Fig. 3.22. The heat cycle required for this sample is a heating phase at a $3^{\circ}\text{C}/\text{min}$ rate up to 180°C and then rest at a constant level of 180°C during 2 hours.

In this case, optimisation of the power evolution is not feasible as the heat cycle required is determined by the curing cycle of the epoxy resin and cannot be changed. However, validation can be performed by the kinetic sources added to the numerical resolution.

For the validation, a Kamal-Sourour model for the curing of epoxy resin is used given by Eq. 3.11 and parameters in Table 3.1 ([44, 45]).

$$\frac{\partial \alpha}{\partial t} = \left(\frac{k_{1c}k_D}{k_{1c} + k_D} + \frac{k_{2c}k_D}{k_{2c} + k_D} \alpha^m \right) (1 - \alpha)^n, \quad (3.11)$$

where $k_D = k_{D0} \exp\left(-\frac{p_1 T - p_2}{p_3(T - T_g) + p_4}\right)$, $k_i = A_i \exp\left(-\frac{E_i}{RT}\right)$ for $i = 1c, 2c$ and $D0$ and $T_g = T_{g0} + \frac{(T_{g\infty} - T_{g0})\beta\alpha}{1 - (1 - \beta)\alpha}$.

Fig. ?? depicts the temperature evolution at sensors location for the heating process of the preform following the power evolution of the experimental trail and considering a Kamal-Sourour model for the resin reaction. The kinetic model is not adapted to our case and leads to a temperature runaway.

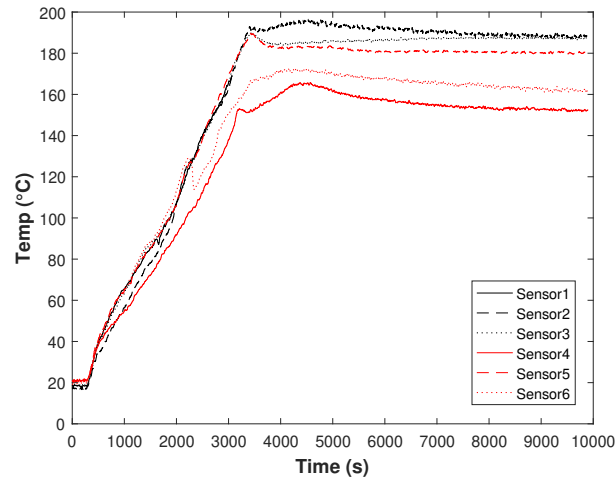


FIGURE 3.23: Measured temperature evolution in time at the six sensors locations in the carbon / epoxy sample

TABLE 3.1: Parameters for the Kamal-Sourour model of the kinetic reaction of the epoxy resin [44, 45]

Parameters	Values
$A_{1c}(s^{-1})$	$4.50 \cdot 10^6$
$A_{2c}(s^{-1})$	$1.30 \cdot 10^6$
$A_{D0}(s^{-1})$	$6.5 \cdot 10^{18}$
$E_{1c}(J/mol)$	74682
$E_{2c}(J/mol)$	58224
$E_{D0}(J/mol)$	136845
$p_1(1/^\circ C)$	0.0023131
$p_2(Nounits)$	0.0181789
$p_3(1/^\circ C)$	0.00048
$p_4(Nounits)$	0.025
$m(Nounits)$	1.4951162
$n(Nounits)$	1.0658882
$T_{g0}(^\circ C)$	-11
$T_{g\infty}(^\circ C)$	228
$\beta(Nounits)$	0.565
$\Delta H(J/g)$	429

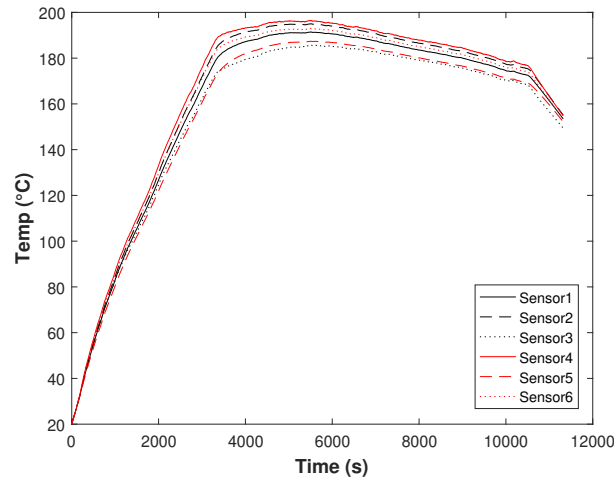


FIGURE 3.24: Temperature evolution at sensors location for the carbon / epoxy sample and simplified kinetic model

Because the Kamal-Sourour model has been modeled from conduction heating, it does not take into account the very specific phenomena the resin encounter when subjected to microwaves. This specific behaviour has been observed in the litterature [28, 59]. In order to fit the experimental data using the MOR technique, a simplified model is proposed:

$$\frac{\partial \alpha}{\partial t} = A(1 - \alpha)^n, \quad (3.12)$$

with $A = 0.00012$ and $n = 1.0658882$.

Fig. 3.24 depicts the results of the simulation with the simplified kinetic model. With the model and parameters chosen, the temperature distribution is consistent with the experimental results.

3.5 Discussions and conclusions

In this chapter, a numerical technique that make possible a real-time control over the heating process has been presented. Using a Model Order Reduction technique, the heat equation is solved with an iterative scheme which allows the user to modify the power delivered by the magnetrons at each time step. Using this technique of resolution of the heat equation and simulations performed by the software CEM One, the heating process of two different composite parts have been studied and compared to experimental data.

In the case of the short carbon fibers preform, experimental and simulation results are consistent. The algorithm for real-time control has been used to identify the optimum power distribution in order to reach the heating requirements as fast as possible. However, even though such power distribution has been identified, it can not be tested in an experimental trial. The small size of the part - with low dissipation of the electromagnetic field refrains the oven to work at full capacity. If the magnetrons deliver a higher power, the numerous reflections of the electromagnetic waves and the low losses in the oven cavity might damage the magnetrons as the reflected waves would have a high amplitude.

In the case of laminate composite composed of carbon fibers and epoxy resin, the heat sources due to the kinetic reaction of the resin have been taken into account. In order to adapt the kinetic model to the specific case of microwave heating, a simplified model has been proposed and depicts matching results with the experimental data.

Conclusion

In order to ensure a growing use of composite materials, new processes have to be developed to match the high expectations of the different industries involved in composite manufacturing: less energy use, faster process and high-quality parts. Following this will, the present work have aimed to the development of the understanding of the phenomena occuring during the heating process of a laminate composite using microwaves thanks to simulation tools.

Several developments have been pursued for different levels of understanding of the process. The first development made has been focused on understanding the propagation of the electric field in a laminate part. Thanks to the PGD approach, the refinement needed at the interface of the several plies of the part has been implemented. Several numerical challenges have been tackled: enforcing the electric field discontinuity at interfaces and the regularisation of the double-curl electromagnetic formulation. The second development proposed in this work concerns the simulation of the full heating process in an oven cavity. Thanks to the coupling of the electromagnetic and thermal resolutions, a deeper understanding of the crucial parameters of the microwave heating process is now available. The third and final development is focused on the industrialization of the process and validation of the work thanks to experimental data generated in a real-size industrial microwave oven. A real-time control over the process is possible thanks to a model order reduction approach to solve the heat equation. Heat sources due to the exothermic reaction of the resin are taken into account and fit the experimental results.

Perspectives for this work are numerous.

- Electromagnetic-thermal coupling: for now, the boundary conditions transfer is enforced only from the oven cavity to the part. However, in order to enforce a strong coupling, an iterative scheme should be introduced. Domain decomposition techniques are suitable for such work

and are under investigation in order to extend the coupling proposed here.

- Heating processes: the simulation tools developed can be extended to any kind of polymer / composite heating due to electromagnetic field, either in a microwave oven cavity or in a more open area under an antenna for example.
- Enhancement of the control algorithm: one interesting additional feature of the control algorithm could be to consider each magnetron individually. Therefore, the optimisation of the process would not only be a faster process but also a limitation of the temperature heterogeneity in the composite part.

Appendix A

Basis of electromagnetism

A.1 Maxwell's equations

The four equations governing the propagation of electric and magnetic fields in a medium are called Maxwell's equations. This set of equations describe how the electromagnetic field $[\mathbf{E}; \mathbf{H}]$ is created by charges and currents.

The first equation is called the Maxwell-Gauss equation. It states that the electric flux \mathbf{D} through a closed surface is proportional to the electric charge ρ_c contained in the surface.

$$\nabla \cdot \mathbf{D} = \rho_c \quad (\text{A.1})$$

The second equation is called the Maxwell-Gauss equation for magnetics and highlights the non-existence of individual magnetic charges (monopoles) contrary to electric charges. The equation states that the magnetic flux \mathbf{B} through a closed surface is zero.

$$\nabla \cdot \mathbf{B} = 0 \quad (\text{A.2})$$

The third equation is called the Maxwell-Faraday equation and translates the induction phenomena. A magnetic field \mathbf{B} changing in time induces an electric field \mathbf{E} travelling in space along a closed line.

$$\nabla \times \mathbf{E} = -\frac{\partial \mathbf{B}}{\partial t} \quad (\text{A.3})$$

The fourth and last equation is called the Maxwell-Ampère equation. It states that magnetic field \mathbf{H} can be generated by either by electric current \mathbf{J} or time-varying electric field \mathbf{D} .

$$\nabla \times \mathbf{H} = \mathbf{J} + \frac{\partial \mathbf{D}}{\partial t} \quad (\text{A.4})$$

A.2 Curl-curl formulation

The curl-curl formulation for the electric field is a partial differential equation which governs the electric field propagation in a medium. This formulation comes from the combination of the Maxwell's equation and of the constitutive laws for materials in electromagnetism:

$$\mathbf{J} = \sigma \mathbf{E}, \quad (\text{A.5})$$

$$\mathbf{D} = \epsilon \mathbf{E}, \quad (\text{A.6})$$

$$\mathbf{B} = \mu \mathbf{H}, \quad (\text{A.7})$$

where σ , ϵ and μ are the dielectric properties of the material: electric conductivity, permittivity and magnetic permeability.

The double-curl formulation is obtained following the steps below starting from the Maxwell-Faraday equation.

$$\nabla \times \mathbf{E} = -\frac{\partial \mathbf{B}}{\partial t} \quad (\text{A.8})$$

$$\nabla \times \mathbf{E} = -\mu \frac{\partial \mathbf{H}}{\partial t} \quad (\text{A.9})$$

$$\frac{1}{\mu} \nabla \times \mathbf{E} = -\frac{\partial \mathbf{H}}{\partial t} \quad (\text{A.10})$$

$$\nabla \times \left(\frac{1}{\mu} \nabla \times \mathbf{E} \right) = -\nabla \times \left(\frac{\partial \mathbf{H}}{\partial t} \right) \quad (\text{A.11})$$

$$\nabla \times \left(\frac{1}{\mu} \nabla \times \mathbf{E} \right) = -\frac{\partial}{\partial t} \nabla \times \mathbf{H} \quad (\text{A.12})$$

$$\nabla \times \left(\frac{1}{\mu} \nabla \times \mathbf{E} \right) = -\frac{\partial}{\partial t} \left(\mathbf{J} + \frac{\partial \mathbf{D}}{\partial t} \right) \quad (\text{A.13})$$

$$\nabla \times \left(\frac{1}{\mu} \nabla \times \mathbf{E} \right) = -\sigma \frac{\partial \mathbf{E}}{\partial t} - \epsilon \frac{\partial^2 \mathbf{E}}{\partial t^2} \quad (\text{A.14})$$

Assuming being in the frequency space, the electric field and its derivatives can be written as:

$$\mathbf{E} = \underline{\mathbf{E}} e^{i\omega t}, \quad (\text{A.15})$$

$$\frac{\partial \mathbf{E}}{\partial t} = i\omega \mathbf{E}, \quad (\text{A.16})$$

$$\frac{\partial^2 \mathbf{E}}{\partial t^2} = -\omega^2 \mathbf{E}, \quad (\text{A.17})$$

where $\underline{\mathbf{E}}$ is the amplitude and ω the angular frequency.

Eq. A.14 then becomes after simplification by $e^{i\omega t}$

$$\nabla \times \left(\frac{1}{\mu} \nabla \times \underline{\mathbf{E}} \right) = -i\omega\sigma\underline{\mathbf{E}} + \omega^2\epsilon\underline{\mathbf{E}}. \quad (\text{A.18})$$

Finally, the curl-curl formulation is obtained:

$$\nabla \times \left(\frac{1}{\mu} \nabla \times \underline{\mathbf{E}} \right) - \omega^2\epsilon^*\underline{\mathbf{E}} = 0 \quad (\text{A.19})$$

where ϵ^* is the complex permittivity defined by:

$$\epsilon^* = \epsilon - i\frac{\sigma}{\omega}. \quad (\text{A.20})$$

A.3 Interface conditions for electric field

To determine the electric field behaviour at the interface between two materials, the integral forms of the Maxwell-Gauss and Maxwell-Faraday equations have to be examined.

First, the Maxwell-Gauss equation is studied, considering in our case no volumic electric charge and integration over a volume:

$$\int \nabla \cdot \mathbf{D} dV = 0 \quad (\text{A.21})$$

which leads to:

$$\oint \mathbf{D} \cdot d\mathbf{S} = 0 \quad (\text{A.22})$$

using the Ostogradsky theorem.

Applying this equation to a small box as depicted in Fig. A.1 and considering $\Delta h \rightarrow \text{zero}$, the fluxes entering and leaving the box through the surface are:

$$\oint \mathbf{D} \cdot d\mathbf{S} = \mathbf{D}_1 \cdot \hat{\mathbf{n}}\Delta s + \mathbf{D}_2 \cdot (-\hat{\mathbf{n}})\Delta s = 0. \quad (\text{A.23})$$

Therefore, the normal component of the electric flux density vector at the interface between two media are related by:

$$D_{n1} = D_{n2} \quad (\text{A.24})$$

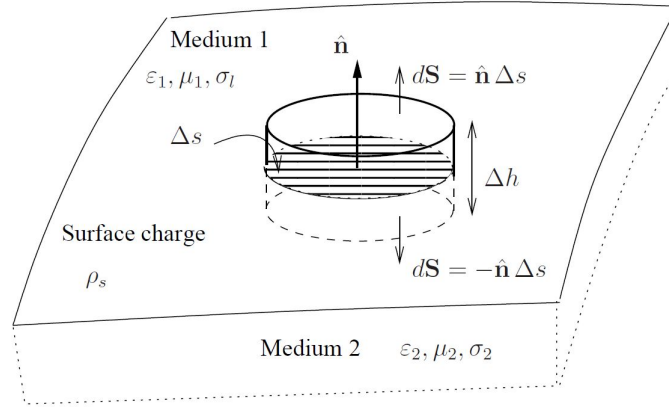


FIGURE A.1: Box at the interface between two media

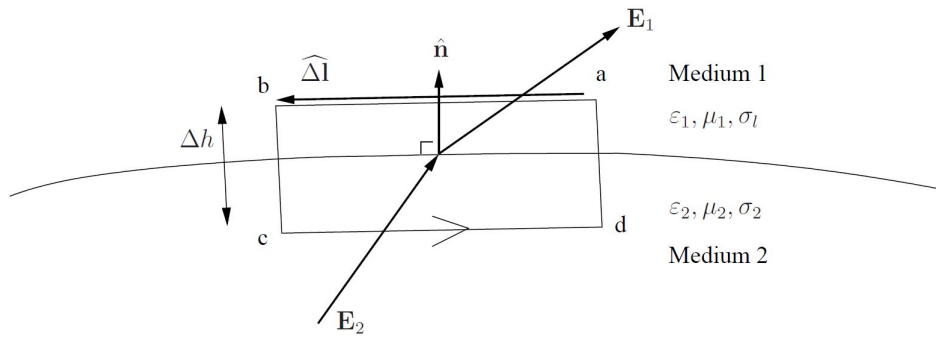


FIGURE A.2: Loop at the interface between two media

and in terms of electric field:

$$\epsilon_1 E_{n1} = \epsilon_2 E_{n2}. \quad (\text{A.25})$$

Then, looking at the Maxwell-Faraday equation integrated over a surface, we have:

$$\oint \nabla \times \mathbf{E} \cdot d\mathbf{S} = - \oint \frac{\partial \mathbf{B}}{\partial t} d\mathbf{S} \quad (\text{A.26})$$

which leads to :

$$\oint \mathbf{E} \cdot d\mathbf{l} = - \oint \frac{\partial \mathbf{B}}{\partial t} d\mathbf{S} \quad (\text{A.27})$$

using the Stokes theorem.

Applying this equation to a small rectangular loop at the interface as depicted in Fig. A.2 and considering $\Delta h \rightarrow$ zero, the magnetic flux tends to zero and electric field is:

$$\oint \mathbf{E} \cdot d\mathbf{l} = \int_a^b \mathbf{E}_1 \cdot d\mathbf{l} + \int_c^d \mathbf{E}_2 \cdot d\mathbf{l} = \mathbf{E}_1 \cdot \Delta \mathbf{l} + \mathbf{E}_2 \cdot (-\Delta \mathbf{l}) = 0. \quad (\text{A.28})$$

Therefore, the tangential components of the electric field are related by:

$$E_{t1} = E_{t2}. \quad (\text{A.29})$$

Appendix B

PGD technique - detailed example on the heat equation

The objective of the following example is to explicit the different steps for the resolution of a numerical problem using the Proper Generalized Decomposition. This example is based on the developments proposed in the litterature [20].

B.1 PGD assumption and heat equation

The example treated in this section is the resolution of the transient heat equation in two dimensions with Dirichlet boundary conditions. The heat equation is considered in the domain $\Omega = \Omega_x \times \Omega_y \times \Omega_t = (0, L) \times (0, L) \times (0, t_{max})$:

$$\rho C_p \frac{\partial T}{\partial t} = \nabla(\lambda \nabla T). \quad (\text{B.1})$$

Boundary and initial conditions are the following:

$$\left\{ \begin{array}{l} T(x = 0, y, t) = T_1 \\ T(x = L, y, t) = T_1 \\ T(x, y = 0, t) = T_1 \\ T(x, y = L, t) = T_1 \\ T(x, y, t = 0) = f(x, y) \end{array} \right. \quad (\text{B.2})$$

where the function f is defined by Eq. B.25 and represented in Fig. B.1.

$$f(x, y) = \begin{cases} T_1 + (T_2 - T_1) \sin(\pi \frac{x}{L}) \sin(2\pi \frac{y}{L}) & \forall x \text{ and } 0 \leq y < \frac{L}{2} \\ T_1 & \forall x \text{ and } \frac{L}{2} \leq y < L \end{cases} \quad (\text{B.3})$$

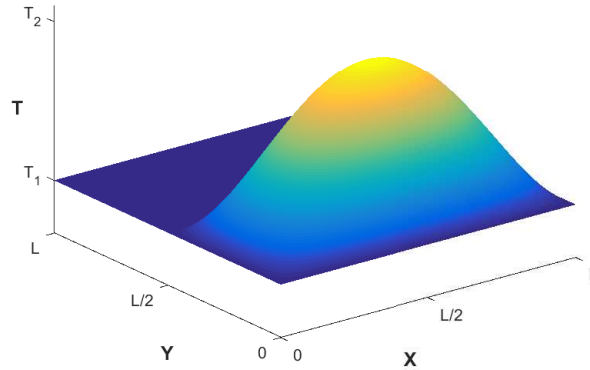


FIGURE B.1: Initial condition f defined on $\Omega_{xy} = (0, L) \times (0, L)$

The weak formulation for the heat equation under such boundary conditions is:

$$\int_{\Omega} T^* \rho C_p \frac{\partial T}{\partial t} d\Omega + \int_{\Omega} \nabla T^* \lambda \nabla T d\Omega = 0 \quad (\text{B.4})$$

for any function T^* regular enough.

The objective is to obtain a solution under the separated form:

$$T(x, y, t) = \sum_{i=1}^N X_i(x) \cdot Y_i(y) \cdot \Theta_i(t). \quad (\text{B.5})$$

The computation is conducted one enrichment term i after another, each enriching the previous one until convergence is reached.

B.2 Construction of the separated representation

The detailed calculation of one enrichment term is presented in this section. For the enrichment step n , the previous terms are assumed known, written under the separated form:

$$T^{n-1}(x, y, t) = \sum_{i=1}^{n-1} X_i(x) \cdot Y_i(y) \cdot \Theta_i(t). \quad (\text{B.6})$$

The next step consists of computing the three unknown functionals $X_n(x)$, $Y_n(y)$ and $\Theta_n(t)$. The resulting problem is non-linear and an iterative scheme by alternating directions is chosen. At iteration p , the approximation of the

temperature field reads:

$$T^{n,p}(x, y, t) = T^{n-1}(x, y, t) + X_n^p(x) \cdot Y_n^p(y) \cdot \Theta_n^p(t). \quad (\text{B.7})$$

The alternating strategy is composed of three steps for each iteration: calculating $X_n^p(x)$ from $Y_n^{p-1}(y)$ and $\Theta_n^{p-1}(t)$, calculating $Y_n^p(y)$ from $X_n^p(x)$ and $\Theta_n^{p-1}(t)$ and finally calculating $\Theta_n^p(t)$ from $X_n^p(x)$ and $Y_n^p(y)$. Random guesses $Y_n^0(y)$ and $\Theta_n^0(t)$ are fixed at the start of the iterative process. The alternating direction scheme runs until reaching a fixed point considering the user-specified tolerance ϵ :

$$\frac{\| X_n^p(x) \cdot Y_n^p(y) \cdot \Theta_n^p(t) - X_n^{p-1}(x) \cdot Y_n^{p-1}(y) \cdot \Theta_n^{p-1}(t) \|}{\| X_n^{p-1}(x) \cdot Y_n^{p-1}(y) \cdot \Theta_n^{p-1}(t) \|} < \epsilon. \quad (\text{B.8})$$

At the end of the process, functionals are assigned: $X_n(x) \leftarrow X_n^p(x)$, $Y_n(y) \leftarrow Y_n^p(y)$ and $\Theta_n(t) \leftarrow \Theta_n^p(t)$.

Each step of the alternating direction strategy is now detailed.

B.2.1 Step 1. Calculating $X_n^p(x)$ from $Y_n^{p-1}(y)$ and $\Theta_n^{p-1}(t)$

The approximation of the temperature field reads:

$$T^{n,p}(x, y, t) = \sum_{i=1}^{n-1} X_i(x) \cdot Y_i(y) \cdot \Theta_i(t) + X_n^p(x) \cdot Y_n^{p-1}(y) \cdot \Theta_n^{p-1}(t), \quad (\text{B.9})$$

where every functional is known except for $X_n^p(x)$. The choice of for the weight function T^* is:

$$T^*(x, y, t) = X_n^*(x) \cdot Y_n^{p-1}(y) \cdot \Theta_n^{p-1}(t). \quad (\text{B.10})$$

Injecting B.9 and B.10 in B.4, we get:

$$\begin{aligned} & \int_{\Omega} X_n^* \cdot Y_n^{p-1} \cdot \Theta_n^{p-1} \rho C_p X_n^p \cdot Y_n^{p-1} \cdot \frac{d\Theta_n^{p-1}}{dt} d\Omega + \int_{\Omega} \frac{dX_n^*}{dx} \cdot Y_n^{p-1} \cdot \Theta_n^{p-1} \lambda \frac{dX_n^p}{dx} \cdot Y_n^{p-1} \cdot \Theta_n^{p-1} d\Omega + \\ & \int_{\Omega} X_n^* \cdot \frac{dY_n^{p-1}}{dy} \cdot \Theta_n^{p-1} \lambda X_n^p \cdot \frac{dY_n^{p-1}}{dy} \cdot \Theta_n^{p-1} d\Omega = \\ & - \int_{\Omega} X_n^* \cdot Y_n^{p-1} \cdot \Theta_n^{p-1} \rho C_p \left(\sum_{i=1}^{n-1} X_i \cdot Y_i \cdot \frac{d\Theta_i}{dt} \right) d\Omega - \int_{\Omega} \frac{dX_n^*}{dx} \cdot Y_n^{p-1} \cdot \Theta_n^{p-1} \lambda \left(\sum_{i=1}^{n-1} \frac{dX_i}{dx} \cdot Y_i \cdot \Theta_i \right) d\Omega - \end{aligned}$$

$$\int_{\Omega} X_n^* \cdot \frac{dY_n^{p-1}}{dy} \cdot \Theta_n^{p-1} \lambda \left(\sum_{i=1}^{n-1} X_i \cdot \frac{dY_i}{dy} \cdot \Theta_i \right) dy. \quad (\text{B.11})$$

Since all functions of y and t are known, we can compute the following integrals over Ω_y and Ω_t :

$$\begin{cases} \alpha^x = \int_{\Omega_y \times \Omega_t} Y_n^{p-1} \cdot Y_n^{p-1} \cdot \Theta_n^{p-1} \cdot \frac{d\Theta_n^{p-1}}{dt} dy \cdot dt \\ \beta^x = \int_{\Omega_y \times \Omega_t} Y_n^{p-1} \cdot Y_n^{p-1} \cdot \Theta_n^{p-1} \cdot \Theta_n^{p-1} dy \cdot dt \\ \gamma^x = \int_{\Omega_y \times \Omega_t} \frac{dY_n^{p-1}}{dy} \cdot \frac{dY_n^{p-1}}{dy} \cdot \Theta_n^{p-1} \cdot \Theta_n^{p-1} dy \cdot dt \\ \delta_i^x = \int_{\Omega_y \times \Omega_t} Y_n^{p-1} \cdot Y_i \cdot \Theta_n^{p-1} \cdot \frac{d\Theta_i}{dt} dy \cdot dt \\ \epsilon_i^x = \int_{\Omega_y \times \Omega_t} Y_n^{p-1} \cdot Y_i \cdot \Theta_n^{p-1} \cdot \Theta_i dy \cdot dt \\ \zeta_i^x = \int_{\Omega_y \times \Omega_t} \frac{dY_n^{p-1}}{dy} \cdot \frac{dY_i}{dy} \cdot \Theta_n^{p-1} \cdot \Theta_i dy \cdot dt \end{cases} \quad (\text{B.12})$$

Eq. B.11 then becomes:

$$\begin{aligned} & \int_{\Omega_x} X_n^* \cdot \rho C_p \cdot \alpha^x \cdot X_n^p dx + \int_{\Omega_x} \frac{dX_n^*}{dx} \cdot \lambda \cdot \beta^x \cdot \frac{dX_n^p}{dx} dx + \\ & \int_{\Omega_x} X_n^* \cdot \lambda \cdot \gamma^x \cdot X_n^p dx = - \sum_{i=1}^{n-1} \left(\int_{\Omega_x} X_n^* \cdot \rho C_p \cdot \delta_i^x \cdot X_i dx + \right. \\ & \left. \int_{\Omega_x} \frac{dX_n^*}{dx} \cdot \lambda \cdot \epsilon_i^x \cdot \frac{dX_i}{dx} dx + \int_{\Omega_x} X_n^* \cdot \lambda \cdot \zeta_i^x \cdot X_i dx \right). \end{aligned} \quad (\text{B.13})$$

The equation we obtain is a weak formulation for a 1D problem defined on Ω_x which can be solved using traditional methods - by the finite element method for example, in order to get the functional X_n^p .

B.2.2 Step 2. Calculating $Y_n^p(y)$ from $X_n^p(x, y)$ and $\Theta_n^{p-1}(t)$

The approximation of the temperature field reads:

$$T^{n,p}(x, y, t) = \sum_{i=1}^{n-1} X_i(x) \cdot Y_i(y) \cdot \Theta_i(t) + X_n^p(x) \cdot Y_n^p(y) \cdot \Theta_n^{p-1}(t), \quad (\text{B.14})$$

where every functional is known except for $Y_n^p(x)$. The choice of for the weight function T^* is:

$$T^*(x, y, t) = X_n^p(x) \cdot Y_n^*(y) \cdot \Theta_n^{p-1}(t). \quad (\text{B.15})$$

Injecting [B.14](#) and [B.15](#) in [B.4](#), we get:

$$\begin{aligned}
& \int_{\Omega} X_n^p \cdot Y_n^* \cdot \Theta_n^{p-1} \rho C_p X_n^p \cdot Y_n^p \cdot \frac{d\Theta_n^{p-1}}{dt} d\Omega + \int_{\Omega} \frac{dX_n^p}{dx} \cdot Y_n^* \cdot \Theta_n^{p-1} \lambda \frac{dX_n^p}{dx} \cdot Y_n^p \cdot \Theta_n^{p-1} d\Omega + \\
& \int_{\Omega} X_n^p \cdot \frac{dY_n^*}{dy} \cdot \Theta_n^{p-1} \lambda X_n^p \cdot \frac{dY_n^p}{dy} \cdot \Theta_n^{p-1} d\Omega = \\
& - \int_{\Omega} X_n^p \cdot Y_n^* \cdot \Theta_n^{p-1} \rho C_p \left(\sum_{i=1}^{n-1} X_i \cdot Y_i \cdot \frac{d\Theta_i}{dt} \right) d\Omega - \int_{\Omega} \frac{dX_n^p}{dx} \cdot Y_n^* \cdot \Theta_n^{p-1} \lambda \left(\sum_{i=1}^{n-1} \frac{dX_i}{dx} \cdot Y_i \cdot \Theta_i \right) d\Omega - \\
& \int_{\Omega} X_n^p \cdot \frac{dY_n^*}{dy} \cdot \Theta_n^{p-1} \lambda \left(\sum_{i=1}^{n-1} X_i \cdot \frac{dY_i}{dy} \cdot \Theta_i \right) d\Omega. \tag{B.16}
\end{aligned}$$

Since all functions of x and t are known, we can compute the following integrals over Ω_x and Ω_t :

$$\left\{ \begin{array}{l}
\alpha^y = \int_{\Omega_x \times \Omega_t} X_n^p \cdot X_n^p \cdot \Theta_n^{p-1} \cdot \frac{d\Theta_n^{p-1}}{dt} dx \cdot dt \\
\beta^y = \int_{\Omega_x \times \Omega_t} \frac{dX_n^p}{dx} \cdot \frac{dX_n^p}{dx} \cdot \Theta_n^{p-1} \cdot \Theta_n^{p-1} dx \cdot dt \\
\gamma^y = \int_{\Omega_x \times \Omega_t} X_n^p \cdot X_n^p \cdot \Theta_n^{p-1} \cdot \Theta_n^{p-1} dx \cdot dt \\
\delta_i^y = \int_{\Omega_x \times \Omega_t} X_n^p \cdot X_i \cdot \Theta_n^{p-1} \cdot \frac{d\Theta_i}{dt} dx \cdot dt \\
\epsilon_i^y = \int_{\Omega_x \times \Omega_t} \frac{dX_n^p}{dx} \cdot \frac{dX_i}{dx} \cdot \Theta_n^{p-1} \cdot \Theta_i dx \cdot dt \\
\zeta_i^y = \int_{\Omega_x \times \Omega_t} X_n^p \cdot X_i \cdot \Theta_n^{p-1} \cdot \Theta_i dx \cdot dt
\end{array} \right. \tag{B.17}$$

Eq. [B.16](#) then becomes:

$$\begin{aligned}
& \int_{\Omega_y} Y_n^* \cdot \rho C_p \cdot \alpha^y \cdot Y_n^p dy + \int_{\Omega_y} Y_n^* \cdot \lambda \cdot \beta^y \cdot Y_n^p dy + \\
& \int_{\Omega_y} \frac{dY_n^*}{dy} \cdot \lambda \cdot \gamma^y \cdot \frac{dY_n^p}{dy} dy = - \sum_{i=1}^{n-1} \left(\int_{\Omega_y} Y_n^* \cdot \rho C_p \cdot \delta_i^y \cdot Y_i dy + \right. \\
& \left. \int_{\Omega_y} Y_n^* \cdot \lambda \cdot \epsilon_i^y \cdot Y_i dy + \int_{\Omega_y} \frac{dY_n^*}{dy} \cdot \lambda \cdot \zeta_i^y \cdot \frac{dY_i}{dy} dy \right). \tag{B.18}
\end{aligned}$$

The equation we obtain is a weak formulation for a 1D problem defined on Ω_y which can be solved using traditional methods - by the finite element method for example, in order to get the functional Y_n^p .

B.2.3 Step 3. Calculating $\Theta_n^p(t)$ from $X_n^p(x)$ and $Y_n^p(y)$

The approximation of the temperature field reads:

$$T^{n,p}(x, y, t) = \sum_{i=1}^{n-1} X_i(x) \cdot Y_i(y) \cdot \Theta_i(t) + X_n^p(x) \cdot Y_n^p(y) \cdot \Theta_n^p(t), \quad (\text{B.19})$$

where every functional is known except for $\Theta_n^p(x)$. The choice of for the weight function T^* is:

$$T^*(x, y, t) = X_n^p(x) \cdot Y_n^p(y) \cdot \Theta_n^*(t). \quad (\text{B.20})$$

Injecting [B.19](#) and [B.20](#) in [B.4](#), we get:

$$\begin{aligned} & \int_{\Omega} X_n^p \cdot Y_n^p \cdot \Theta_n^* \rho C_p X_n^p \cdot Y_n^p \cdot \frac{d\Theta_n^p}{dt} d\Omega + \int_{\Omega} \frac{dX_n^p}{dx} \cdot Y_n^p \cdot \Theta_n^* \lambda \frac{dX_n^p}{dx} \cdot Y_n^p \cdot \Theta_n^p d\Omega + \\ & \int_{\Omega} X_n^p \cdot \frac{dY_n^p}{dy} \cdot \Theta_n^* \lambda X_n^p \cdot \frac{dY_n^p}{dy} \cdot \Theta_n^p d\Omega = \\ & - \int_{\Omega} X_n^p \cdot Y_n^p \cdot \Theta_n^* \rho C_p \left(\sum_{i=1}^{n-1} X_i \cdot Y_i \cdot \frac{d\Theta_i}{dt} \right) d\Omega - \int_{\Omega} \frac{dX_n^p}{dx} \cdot Y_n^p \cdot \Theta_n^* \lambda \left(\sum_{i=1}^{n-1} \frac{dX_i}{dx} \cdot Y_i \cdot \Theta_i \right) d\Omega - \\ & \int_{\Omega} X_n^p \cdot \frac{dY_n^p}{dy} \cdot \Theta_n^* \lambda \left(\sum_{i=1}^{n-1} X_i \cdot \frac{dY_i}{dy} \cdot \Theta_i \right) d\Omega. \end{aligned} \quad (\text{B.21})$$

Since all functions of x and y are known, we can compute the following integrals over Ω_x and Ω_y :

$$\left\{ \begin{array}{l} \alpha^t = \int_{\Omega_x \times \Omega_y} X_n^p \cdot X_n^p \cdot Y_n^p \cdot Y_n^p dx \cdot dy \\ \beta^t = \int_{\Omega_x \times \Omega_y} \frac{dX_n^p}{dx} \cdot \frac{dX_n^p}{dx} \cdot Y_n^p \cdot Y_n^p dx \cdot dy \\ \gamma^t = \int_{\Omega_x \times \Omega_y} X_n^p \cdot X_n^p \cdot \frac{dY_n^p}{dy} \cdot \frac{dY_n^p}{dy} dx \cdot dy \\ \delta_i^t = \int_{\Omega_x \times \Omega_y} X_n^p \cdot X_i \cdot Y_n^p \cdot Y_i dx \cdot dy \\ \epsilon_i^t = \int_{\Omega_x \times \Omega_y} \frac{dX_n^p}{dx} \cdot \frac{dX_i}{dx} \cdot Y_n^p \cdot Y_i dx \cdot dy \\ \zeta_i^t = \int_{\Omega_x \times \Omega_y} X_n^p \cdot X_i \cdot \frac{dY_n^p}{dy} \cdot \frac{dY_i}{dy} dx \cdot dy \end{array} \right. \quad (\text{B.22})$$

Eq. [B.21](#) then becomes:

$$\int_{\Omega_t} \Theta_n^* \cdot \rho C_p \cdot \alpha^t \cdot \frac{d\Theta_n^p}{dt} dt + \int_{\Omega_t} \Theta_n^* \cdot \lambda \cdot \beta^t \cdot \Theta_n^p dt +$$

$$\int_{\Omega_t} \Theta_n^* \cdot \lambda \cdot \gamma^t \cdot \Theta_n^p dt = - \sum_{i=1}^{n-1} \left(\int_{\Omega_t} \Theta_n^* \cdot \rho C_p \cdot \delta_i^t \cdot \frac{d\Theta_i}{dt} dt + \int_{\Omega_t} \Theta_n^* \cdot \lambda \cdot \epsilon_i^t \cdot \Theta_i dt + \int_{\Omega_t} \Theta_n^* \cdot \lambda \cdot \zeta_i^t \cdot \Theta_i dt \right). \quad (\text{B.23})$$

The equation we obtain is a weak formulation for a 1D problem defined on Ω_t which can be solved using traditional methods - by the finite element method for example, in order to get the functional Θ_n^p .

B.3 Numerical application

Analytical and PGD solutions are compared in this section. The analytical solution for the heat equation as described above is:

$$T_{ex}(x, y, t) = T_1 + \sum_{m=0}^{\infty} B_m \sin(\pi x) \sin(m\pi y) e^{-2\pi(1+m^2)\alpha t} \quad (\text{B.24})$$

where $\alpha = \frac{k}{\rho C_p}$ and

$$B_m = \begin{cases} \frac{(T_2 - T_1)}{32} & \text{if } m = 2 \\ \frac{(T_2 - T_1)}{16} \left(\frac{1}{\pi(m-2)} \sin\left(\frac{\pi}{2}(m-2)\right) - \frac{1}{\pi(m+2)} \sin\left(\frac{\pi}{2}(m+2)\right) \right) & \text{if } m \neq 2 \end{cases} \quad (\text{B.25})$$

Boundary and initial conditions are defined using the constants $T_1 = 293K$ and $T_2 = 573K$. Material properties are taken as $\alpha = 10^{-4} m^2/s$. The dimensions of the 2D spatial domain are set with $L = 1m$ and the mesh is made of $M = 90$ 1D linear elements in x and y directions. The resolution is calculated with $t_{max} = 10min$ with a time step of 1 second.

Evolution of temperature during time is depicted on Fig. B.2. Fig. B.3 shows the difference between exact solution and PGD solution at $t = t_{max}$ for different enrichment steps N. As N increases, the difference decreases and tends to a stable distribution as given for $N = 30$. The convergence of the PGD with respect to M and N is depicted on Fig. B.4.

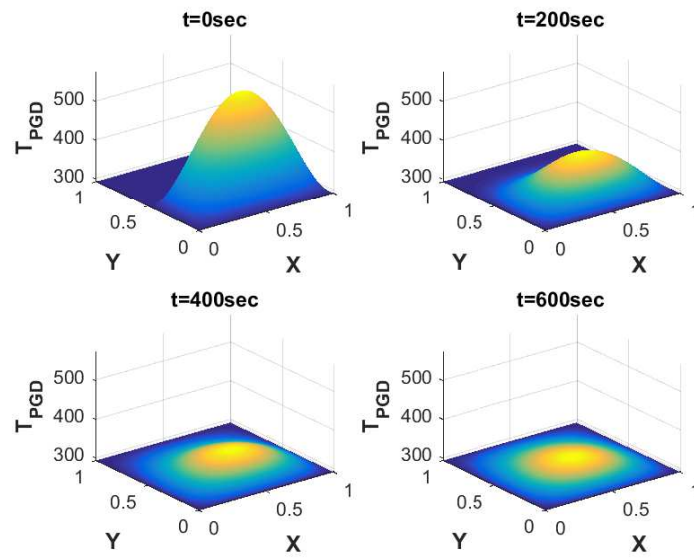


FIGURE B.2: Temperature distribution as calculated using the PGD at different time

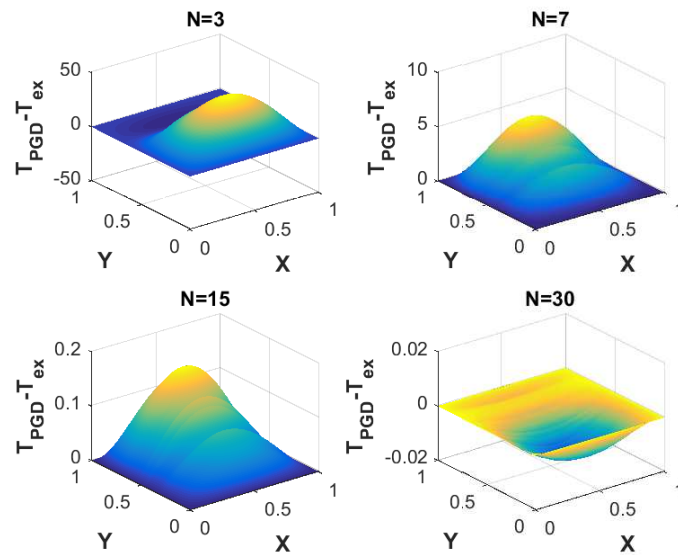


FIGURE B.3: $T_{PGD} - T_{ex}$ for $M = 90$ and different enrichment steps N for $t = t_{max}$

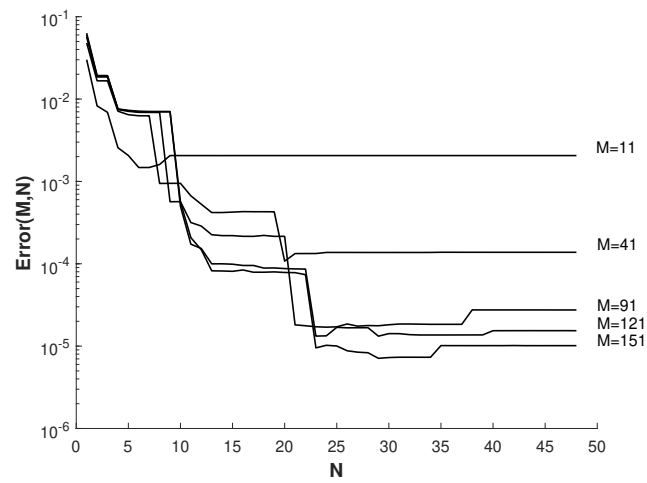


FIGURE B.4: Error between PGD solution and analytical solution as a function of enrichment steps N and discretization refinement M for $t = t_{max}$

Bibliography

- [1] J. Abdulnour and L. Marchildon. "Scattering by a dielectric obstacle in a rectangular waveguide". In: *IEEE Transactions on Microwave Theory and Techniques* 41.11 (1993), pp. 1988–1994.
- [2] M. Jaleel Akhtar, L. E. Feher, and M. Thumm. "A waveguide-based two-step approach for measuring complex permittivity tensor of uniaxial composite materials". In: *IEEE Transactions on Microwave Theory and Techniques* 54.5 (2006), pp. 2011–2022.
- [3] A. Ammar, B. Mokdad, F. Chinesta, and R. Keunings. "A new family of solvers for some classes of multidimensional partial differential equations encountered in kinetic theory modeling of complex fluids". In: *Journal of Non-Newtonian Fluid Mechanics* 139.3 (2006), pp. 153–176.
- [4] S. Arakelyan, H. Lee, D. Han, A. Babajanyan, G. Berthiau, B. Friedman, and K. Lee. "Microwave Heating Visualization for Carbon Fibers Composite Material: Development of Tunable Microstrip Structures". In: *IEEE Transactions on Microwave Theory and Techniques* 66 (2018), pp. 883–888.
- [5] T. Basak and S. Durairaj. "Numerical Studies on Microwave Heating of Thermoplastic-Ceramic Composites Supported on Ceramic Plates". In: *Journal of Heat Transfer* 132.7 (2010).
- [6] A. Benatar and T.G. Gutowski. "Method for fusion bonding thermoplastic composites". In: *SAMPE Quarterly; (United States)* 18.1 (1986), pp. 35–42.
- [7] S. Bensaïd, D. Trichet, and J. Fouladgar. "3D simulation of induction heating of anisotropic composite materials". In: *IEEE Transactions on Magnetics* 41.5 (2005), pp. 1568–1571.
- [8] S. Bensaïd, D. Trichet, and J. Fouladgar. "Electromagnetic and thermal behaviours of multi-layer anisotropic composite materials". In: *IEEE Transactions on Magnetics* 42.4 (2006), pp. 995–998.
- [9] R. Bocquet and Loiretech. "Outillage pour la mise en oeuvre d'un matériau composite". Pat. European Patent 14159000.0. 2014.

- [10] B. Bognet, A. Leygue, and F. Chinesta. "Separated representations of 3D elastic solutions in shell geometries". In: *Advanced Modelling and Simulation in Engineering Sciences* (2014), pp. 1–4. URL: <http://www.amses-journal.com/content/1/1/4>.
- [11] B. Bognet, A. Leygue, F. Chinesta, A. Poitou, and F. Bordeu. "Advanced simulation of models defined in plate geometries: 3D solutions with 2D computational complexity". In: *Computer Methods in Applied Mechanics and Engineering* 201–204 (2012), pp. 1–12. URL: <http://www.sciencedirect.com/science/article/pii/S0045782511002891>.
- [12] W.E. Boyse, D.R. Lynch, K.D. Paulsen, and G.N. Minerbo. "Nodal-based finite-element modeling of Maxwell's equations". In: *IEEE Transactions on Antennas and Propagation* 40 (1992), pp. 642–651.
- [13] H. K. Bui, G. Wasselynck, D. Trichet, and G. Berthiau. "Degenerated hexahedral whitney elements for electromagnetic fields computation in multi-layer anisotropic thin regions". In: *IEEE Transactions on Magnetics* 52.3 (2016).
- [14] N. Bur, P. Joyot, Ch. Ghnatios, P. Villon, E. Cueto, and F. Chinesta. "Advanced computational vademecums for Automated Fibre Placement processes". In: *Advanced Modelling and Simulation in Engineering Sciences* 3 (2016). URL: <https://amses-journal.springeropen.com/articles/10.1186/s40323-016-0056-x>.
- [15] F.C. Campbell. *Structural Composite Material. Chapter 1. Introduction to Composite Material*. ASM International, 2010.
- [16] CEM One. ESI Group, Rungys, France. 2011. URL: <https://www.esi-group.com/fr/solutions-logicielles/environnement-virtuel/electromagnetisme/cem-one>.
- [17] W.C. Chew and M.A. Nasir. "A Variational analysis of anisotropic, inhomogeneous dielectric waveguides". In: *IEEE Transactions on Microwave Theory and Technologies* 37.4 (1989), pp. 661–668.
- [18] F. Chinesta, A. Leygue A. Ammar, and R. Keunings. "An overview of the Proper Generalized Decomposition with applications in computational rheology". In: *Journal of Non Newtonian Fluid Mechanics* 166.11 (2011), pp. 578–592. URL: <http://www.sciencedirect.com/science/article/pii/S0377025711000061>.
- [19] F. Chinesta, A. Ammar, and E. Cueto. "Recent advances and new challenges in the use of the Proper Generalized Decomposition for solving multidimensional models". In: *Archives of Computational Methods in Engineering* 17 (2010), pp. 327–350.

- [20] F. Chinesta, R. Keunings, and A. Leygue. *The Proper Generalized Decomposition for advanced numerical simulations. A primer*. Springerbriefs, Springer, 2014.
- [21] F. Chinesta, P. Ladeveze, and E. Cueto. “A short review in model order reduction based on Proper Generalized Decomposition”. In: *Archives of Computational Methods in Engineering* 18 (2011), pp. 395–404.
- [22] F. Chinesta, A. Leygue, B. Bognet, Ch. Ghnatios, F. Poulhaon, F. Bordeu, A. Barasinski, A. Poitou, S. Chatel, and S. Maison-Le-Poec. “First steps towards an advanced simulation of composites manufacturing by Automated Tape Placement”. In: *International Journal of Material Forming* 7.1 (2014), pp. 81–92.
- [23] P. Ciarlet. “Augmented formulations for solving Maxwell equations”. In: *Computer Methods in Applied Mechanics and Engineering* 194 (2005), pp. 559–586.
- [24] *Comsol Multiphysics v5.3a*. COMSOL AB, Stockholm, Sweden. 2017. URL: www.comsol.com.
- [25] M. Costabel and M. Dauge. “Weighted regularization of Maxwell equations in polyhedral domains”. In: *Numerische Mathematik* 93.2 (2002), pp. 239–277.
- [26] H. Deng, J. Ramos, and P. Yang. “Thermal Properties of a Glass Fiber Filled Epoxy (Sumitomo E264H)”. In: *The Rio Grande Symposium on Advanced Materials* (2015).
- [27] E. Diaz. *WAVECOM Project - Microwave assisted curing for carbon fiber reinforced epoxy composites*. European Union CORDIS Project. 2014. URL: http://cordis.europa.eu/result/rcn/140584_en.html.
- [28] G. B. Dudley, R. Richert, and A.E. Stiegman. “On the existence of and mechanism for microwave-specific reaction rate enhancement”. In: *Chemical Science* 6.4 (2015), pp. 2144–2152.
- [29] L.E. Feher. *Energy Efficient Microwave Systems: Materials Processing Technologies for Avionic, Mobility and Environmental Applications*. Springer Science and Business Media, 2009.
- [30] G.G. Gentili and L. Accatino. “A 2.5D FEM analysis of E-plane structures”. In: *International Conference on Numerical Electromagnetic Modeling and Optimization for RF, Microwave, and Terahertz Applications (NEMO)* (2014).

- [31] E. Giner, B. Bognet, J.J. Rodenas, A. Leygue, J. Fuenmayor, and F. Chinesta. "The Proper Generalized Decomposition (PGD) as a numerical procedure to solve 3D cracked plates in linear elastic fracture mechanics". In: *International Journal of Solid Structures* 50.10 (2013), pp. 1710–1720. URL: <http://www.sciencedirect.com/science/article/pii/S0020768313000541>.
- [32] J. Gyselinck, L. Krahenbuhl P. Dular, and R.V. Sabariego. "Finite-element homogenization of laminated iron cores with inclusion of net circulating currents due to imperfect insulation". In: *IEEE Transactions on Magnetics* 52.3 (2016).
- [33] I.H. Hacialioglu. *A review of the global composites market and turkish composites market*. 2018. URL: <http://www.reinforcer.com/en/author/default/General-Secretary-Kompozit-Sanayicileri-Dernegi/61/350/0>.
- [34] R.F. Harrington. *Field Computation by Moment Methods*. IEEE Press, 1968.
- [35] R.F. Harrington. "Origin and development of the method of moments for field computation". In: *IEEE Antennas and Propagation Magazine* 32.3 (1990), pp. 31–35.
- [36] C. Hazard and M. Lenoir. "On the solution of the time-harmonic scattering problems for Maxwell's equations". In: *SIAM Journal on Mathematical Analysis* 27 (1996), pp. 1597–1630.
- [37] T. Henneron and S. Clenet. "Model order reduction of quasi-static problems based on POD and PGD approaches". In: *European Physical Journal: Applied Physics* 64.2 (2013), pp. 1–7. URL: <http://hal.archives-ouvertes.fr/hal-00851978>.
- [38] T. Henneron and S. Clenet. "Proper Generalized Decomposition method applied to solve 3-D magnetoquasi-static field problems coupling with external electric circuits". In: *IEEE Transactions on Magnetics* 51.6 (2015), pp. 1–10.
- [39] C.L. Hollway, M.S. Sarto, and M. Johansson. "Analyzing carbon-fiber composite materials with equivalent-layer models". In: *IEEE transactions on electromagnetic compatibility* 47.4 (2005), pp. 833–844.
- [40] C. Hunyar, L. Feher, and M. Thumm. "Processing of Carbon-Fiber Reinforced Composite (CFRP) Materials with Innovative Millimeter-Wave Technology". In: *Advances in Microwave and Radio Frequency Processing* (2006), pp. 735–744.
- [41] BNZ Materials Inc. *Transite HT Material Properties*. 2010. URL: http://www.redseal.com/download/Spec_Transite_HT.pdf.

- [42] J. Jin. *The Finite Element Method in Electromagnetics*. John Wiley & Sons, 2002.
- [43] M.R. Kamal, S. Sourour, and M. Ryan. "Integrated thermo – rheological analysis of the cure of thermosets". In: *Society of Plastics Engineers Technical Papers* 19 (1973), pp. 187–191.
- [44] P.I. Karkanis and I.K. Partridge. "Cure modelling and monitoring of epoxy/amine resin systems. I. Cure kinetics modelling". In: *Journal of Applied Polymer Science* 77 (2000), pp. 1419–1431.
- [45] P.I. Karkanis and I.K. Partridge. "Cure modelling and monitoring of epoxy/amine resin systems. II. Network formation and chemoviscosity modeling". In: *Journal of Applied Polymer Science* 77 (2000), pp. 2178–2188.
- [46] K.S. Kunz and K.M. Lee. "A three-dimensional finite-difference solution of the external response of an aircraft to a complex transient EM environment". In: *IEEE Transactions on Electromagnetic Compatibility* 20.2 (1978), pp. 328–341.
- [47] M. Kwak, P. Robinson, A. Bismarck, and R. Wise. "Curing of Composite Materials Using the Recently Developed Hepahaistos Microwave". In: *18th International Conference on Composite Materials* (2011).
- [48] M. Kwak, P. Robinson, A. Bismarck, and R. Wise. "Microwave curing of carbon-epoxy composites: penetration depth and material characterisation". In: *Composites: Part A* 75 (2015), pp. 18–27.
- [49] P. Ladeveze. "On a family of algorithms for structural mechanics (in french)". In: *Comptes Rendus Académie des Sciences Paris* 300.2 (1985), pp. 41–44.
- [50] W.I. Lee and G.S. Springer. "Microwave Curing of Composites". In: *Journal of Composite Materials* 18.4 (1984), pp. 387–409.
- [51] N. Li, Y. Li, X. Hao, and J. Gao. "A comparative experiment for the analysis of microwave and thermal process induces strains of carbon fiber/bismaleimide composite materials". In: *Composites: Science and Technology* 106 (2015), pp. 15–19.
- [52] Y. Li, N. Yi, and J. Gao. "Tooling design and microwave curing technologies for the manufacturing of fiber-reinforced polymer composites in aerospace applications". In: *International Journal of Advanced Manufacturing Technology* 70.1–4 (2014), pp. 591–606.

- [53] E.X. Liu, X.C. Wei, and E.P. Li. "2.5D methodologies for electronic package and PCB modeling: Review and latest development". In: *IEEE International Symposium on Electromagnetic Compatibility (EMC)* (2016), pp. 801–805.
- [54] G.A. Marengo, T.M. Herkner, and GKN Aerospace Services Limited. "Manufacturing method for components made of fiber-reinforced composite materials by using microwaves". Pat. US Patent 8,916,016 B2. 2014.
- [55] H. Miyagawa, K. Wakino, and Y.D. Lin. "Simultaneous determination of complex permittivity and permeability of columnar materials with arbitrary shaped cross-section". In: *IEEE Transactions on Microwave Theory and Techniques* 57.9 (2009), pp. 2249–2256.
- [56] D. Modesto and J. De la Puente. "Fast solution of Maxwell's equations for CSEM simulations by reduced order methods". In: *SEG Technical Program Expanded Abstracts 2017* (2017), pp. 1147–1151.
- [57] G. Mur. "Edge elements, their advantages and their disadvantages". In: *IEEE Transactions on Magnetics* 30.5 (1994), pp. 3552–3557.
- [58] G. Mur. "The fallacy of edge elements". In: *IEEE Transactions on Magnetics* 34.5 (1998), pp. 3244–3247.
- [59] P. Navabpour, A. Nesbitt, B. Degambder, G. Fernando, T. Mann, and R. Day. "Comparison of the curing kinetics of the RTM6 epoxy resin system using differential scanning calorimetry and a microwave-heated calorimeter". In: *Journal of Applied Polymer Science* 9.6 (2005), pp. 3658–3668.
- [60] J.C. Nedelec. "Mixed finite elements in R³". In: *Numerische Mathematik* 35.3 (1980), pp. 315–341.
- [61] M.N. Ney. "Method of moments as applied to electromagnetics problems". In: *IEEE Transactions on Microwave theory and Techniques* 33.10 (1985), pp. 972–980.
- [62] C. Nightingale and R.J. Day. "Flexural and interlaminar shear strength properties of carbon fibre/epoxy composites cured thermally and with microwave radiation". In: *Composites Part A: Applied Science and Manufacturing* 33.7 (2002), pp. 1021–1030.
- [63] I. Niyonzima, R.V. Sabariego, P.Dular, F.Henrotte, and C. Geuzaine. "Computational homogenization for laminated ferromagnetic cores in magnetodynamics". In: *IEEE Transactions on Magnetics* 49.5 (2013), pp. 2049–2052.

- [64] R. Otin. "ERMES: A nodal-based finite element code for electromagnetic simulations in frequency domain". In: *Computer Physics Communications* 184.11 (2013), pp. 2588–2595. URL: <http://www.sciencedirect.com/science/article/pii/S001046551300204X>.
- [65] R. Otin. "Regularized Maxwell equations and nodal finite elements for electromagnetic field computations". In: *Journal Electromagnetics* 30.1–2 (2010), pp. 190–204.
- [66] G. Pan and J. Tan. "General edge element approach to lossy and dispersive structures in anisotropic media". In: *IEEE Proceedings: Microwaves, Antennas and Propagation* 144.2 (1997), pp. 81–89.
- [67] J.P. Pascault, H. Sautereau, J. Verdu, and R.J.J. Williams. *Thermosetting Polymers*. Marcel Dekker, 2003.
- [68] K.D. Paulsen, D.R. Lynch, and J.W. Strohbehm. "Numerical treatment of boundary conditions at points connecting more than two electrically distinct regions". In: *Communications in Applied Numerical Methods* 3 (1987), pp. 53–62.
- [69] K.D. Paulsen, D.R. Lynch, and J.W. Strohbehm. "Three dimensional finite, boundary, and hybrid element solutions of Maxwell equations for lossy dielectric media". In: *IEEE Transactions on Microwave Theory and Techniques* 36.4 (1988), pp. 682–693.
- [70] M. Pineda, F. Chinesta, J. Roger, M. Riera, J. Perez, and F. Daim. "Simulation of skin effect via separated representations". In: *International Journal for Computation and Mathematics in Electrical and Electronic Engineering* 29.4 (2010), pp. 919–929. URL: <http://hal.archives-ouvertes.fr/hal-01008914>.
- [71] J. Rautio. "Some Comments on Electromagnetic Dimensionality". In: *IEEE M-TTS Newsletter Winter 1992* (1992), p. 23.
- [72] C.C. Riccardi, F. Fraga, J. Dupuy, and R.J.J. Williams. "Cure kinetics of diglycidylether of bisphenol A – ethylenediamine revisited using a mechanistic model". In: *Journal of Applied Polymer Science* 82 (2001), pp. 2319–2325.
- [73] M.E. Ryan and A. Dutta. "Kinetics of epoxy cure: a rapid technique for kinetic parameter estimation". In: *Polymer* 20 (1979), pp. 203–206.
- [74] H. Saito, M. Morita, K. Kawabe, M. Kanasaki, and I. Kimpara H. Takeuchi M. Tanaka. "Effect of ply thickness on impact damage morphology in CFRP laminates". In: *Journal of Reinforced Plastics and Composites* 30.13 (2011), pp. 1097–1106.

- [75] S. Sanchez-Saez, E. Barbero, R. Zaera, and C. Navarro. "Compression after impact of thin composite laminates". In: *Composites Science and Technology* 65.13 (2005), pp. 1911–1919. URL: <http://www.sciencedirect.com/science/article/pii/S0266353805000990>.
- [76] S. Sihm, R.Y. Kim, K. Kawabe, and S.W. Tsai. "Experimental studies of thin-ply laminated composites". In: *Composites Science and Technology* 67.6 (2007), pp. 996–1008. URL: <http://www.sciencedirect.com/science/article/pii/S0266353806002168>.
- [77] V.I. Sokolov, S.I. Shalgunov, I.G. Gurtovnik, L.G. Mikheeva, and I.D. Simonov-Emelyanov. "Dielectric characteristics of glass fibre reinforced plastics and their components". In: *International Polymer Science and Technology* 32.7 (2005), pp. 62–67.
- [78] S. Sourour and M.R. Kamal. "Differential scanning calorimetry of epoxy cure: isothermal cure kinetics". In: *Thermochimica Acta* 14 (1976), pp. 41–59.
- [79] W. Suwanwatana, S. Yarlagadda, and J. W. Gillespie Jr. "Hysteresis heating based induction bonding of thermoplastic composites". In: *Composites Science and Technology* 66.11–12 (2006), pp. 1713–1723.
- [80] D.G. Swanson and W.J.R. Hoefer. *Microwave circuit modeling using electromagnetic field simulation*. Artech House Publishers, 2003.
- [81] A. Taflove. "Application of the finite-difference time-domain method to sinusoidal steady-state electromagnetic-penetration problems". In: *IEEE Transactions on Electromagnetic Compatibility* 22.3 (1980), pp. 191–202.
- [82] A. Taflove and K.R. Umashankar. "Solution of complex electromagnetic penetration and scattering problems in unbounded regions". In: *Computational Methods for Infinite Domain Media-structure Interaction* 46 (1981), pp. 83–113.
- [83] E.T. Thostenson and T. Chou. "Microwave and Conventional Curing of Thick-Section Thermoset Composite Laminates: Experiment and Simulation". In: *Polymer Composites* 22.2 (2001), pp. 197–212.
- [84] G. Wasselynck. "Etude des interactions entre les ondes électromagnétiques de fréquences moyennes et les matériaux composites. Application à l'assemblage par induction de ces matériaux". In: *PhD thesis, Ecole Polytechnique de l'Université de Nantes* (2011).

- [85] G. Wasselynck, D. Trichet, B. Ramdane, and J. Fould. "Interaction between electromagnetic field and CFRP materials: A new multiscale homogenization approach". In: *IEEE Transactions on Magnetics* 46.8 (2010), pp. 3277–3280.
- [86] X.C. Wei, E.P. Li, E.X. Liu, and R. Vahldieck. "Efficient simulation of power distribution network by using integral-equation and modal-decoupling technology". In: *IEEE Transactions on Microwave Theory and Techniques* 56.10 (2008), pp. 2277–2285.
- [87] N.H. Williams. "Curing Epoxy Resin Impregnated Pipe at 2450 Mega-Hertz". In: *Journal of Microwave Power* 2.4 (1967), pp. 123–127.
- [88] C.W. Wise, W.D. Cook, and A.A. Goodwin. "Chemico-diffusion kinetics of model epoxy-amine resins". In: *Polymer* 38 (1997), pp. 3251–3261.
- [89] R.J. Wise and I.D. Froment. "Microwave welding of thermoplastics". In: *Journal of Materials Science* 36 (2001), pp. 5935–5954.
- [90] V. Yakovlev. *Introduction to Multiphysics Modeling in Microwave Power Engineering*. Short Course, 52nd Annual Microwave Power Symposium. 2018.
- [91] K.S. Yee. "Numerical solution of initial boundary-value problems involving Maxwell's equations in isotropic media". In: *IEEE Transactions on Antennas and Propagation* 14 (1966), pp. 302–307.
- [92] T. Yokozeki, A. Kuroda, A. Yoshimura, T. Ogasawara, and T. Aoki. "Damage characterization in thin-ply composite laminates under out-of-plane transverse loadings". In: *Composite Structures* 93.1 (2010), pp. 49–57. URL: <http://www.sciencedirect.com/science/article/pii/S0263822310002254>.
- [93] R. Yusoff, M.K. Aroua, A. Nesbitt, and R.J. Day. "Curing of Polymeric Composites Using Microwave Resin Transfer Moulding (RTM)". In: *Journal of Engineering Science and Technology* 2.2 (2007), pp. 151–163.
- [94] O.I. Zhupanska and R.L. Sierakowski. "Electro-thermo mechanical coupling in carbon fiber polymer matrix composites". In: *Acta Mechanica* 218 (2011), pp. 319–332.